S. Schlücker

DOI: 10.1002/anie.201205748

Spectroscopic Methods

Surface-Enhanced Raman Spectroscopy: Concepts and Chemical Applications

*Sebastian Schlücker**

Keywords:
plasmonics · Raman spectroscopy · SERS · spectroscopic methods · surfaces

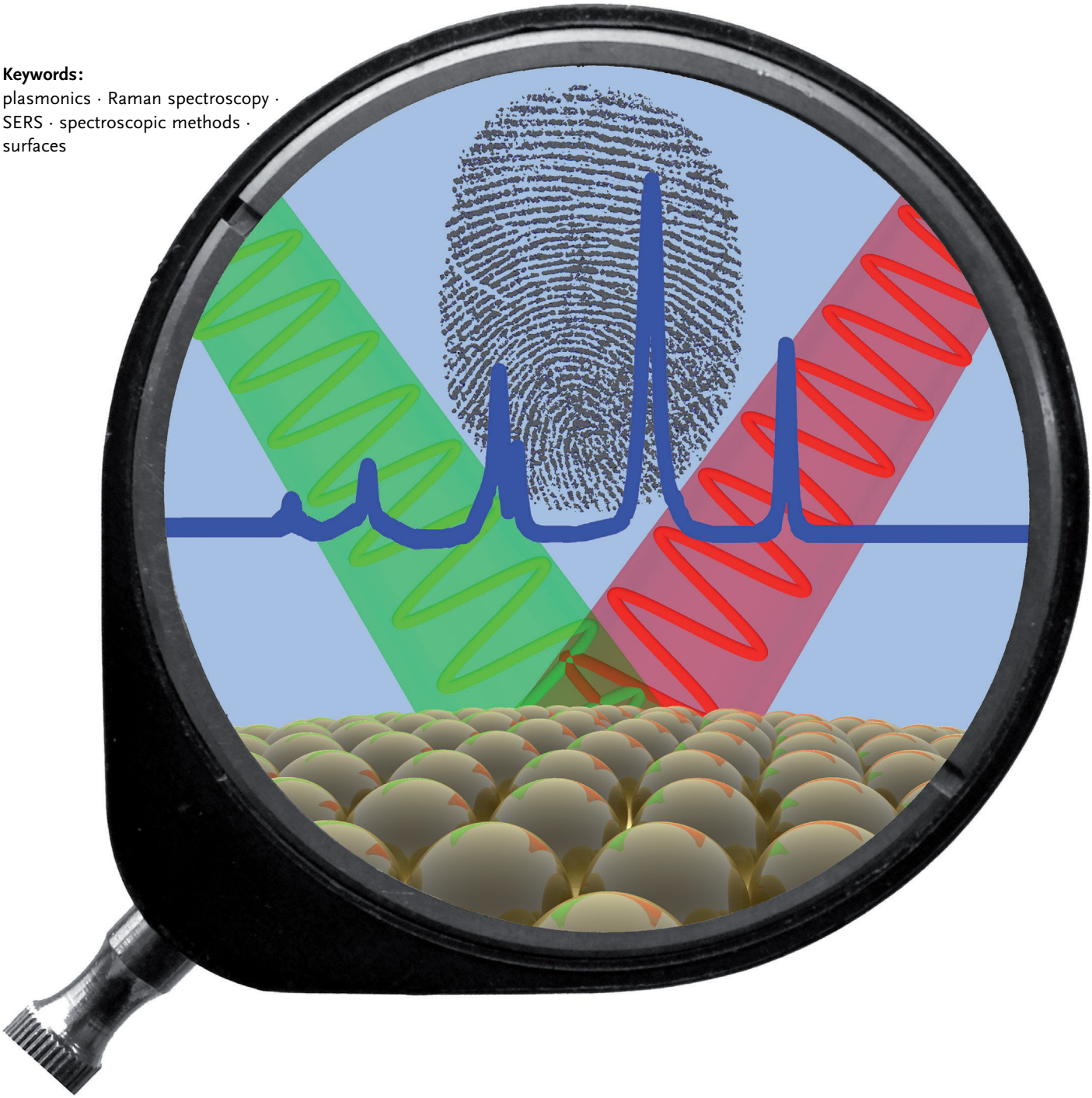

Angewandte International Edition Chemie

Surface-enhanced Raman scattering (SERS) has become a mature vibrational spectroscopic technique during the last decades and the number of applications in the chemical, material, and in particular life sciences is rapidly increasing. This Review explains the basic theory of SERS in a brief tutorial and—based on original results from recent research—summarizes fundamental aspects necessary for understanding SERS and provides examples for the preparation of plasmonic nanostructures for SERS. Chemical applications of SERS are the centerpiece of this Review. They cover a broad range of topics such as catalysis and spectroelectrochemistry, single-molecule detection, and (bio)analytical chemistry.

From the Contents

1. Introduction

Surface-enhanced Raman scattering (SERS) is a phenomenon first observed in 1973 (first publication: 1974) for pyridine adsorbed on a roughened silver electrode[1] and correctly interpreted in 1977.[2] Initially, SERS was employed by a relatively small community of scientists with expertise in both electrochemistry and Raman spectroscopy, the latter requiring an in-depth knowledge of optics and lasers at that time. The observation of single-molecule SERS in 1997[3,4] was a strong stimulus for the field since it demonstrated that the signal strength of Raman scattering can rival that of fluorescence. For the rapid development of SERS during the last two decades, advances in nanofabrication and Raman instrumentation were equally important. Nowadays, scientists from a large range of disciplines—including chemistry, physics, and material and life sciences—are increasing our knowledge on SERS and only begin to fully exploit the huge potential of this technique in numerous uni- and multidisciplinary approaches.

Several excellent review articles,[5–10] monographs,[11–13] and themed journal issues[14–18] as well as proceedings of a Faraday Discussion[19] on SERS are available. The main intent of this Review addressed to the general chemical audience is to summarize key concepts and highlight selected contributions from individual research groups during the last decade, which are of interest to *Angewandte Chemie*'s broad and heterogeneous readership. Therefore this Review does not contain a complete list of citations from the extensive SERS literature, but instead refers the reader to recent SERS reviews on the corresponding topic.

After a brief tutorial on SERS (Section 2), important results from selected research articles on fundamental aspects of SERS are highlighted (Section 3). Since metal nanostructures are a prerequisite for observing SERS, selected important conceptual and synthesis developments in this field are highlighted (Section 4). Chemical applications of SERS discussed in Section 5 are the centerpiece of this Review. A broad and diverse range of topics is covered, from catalysis and spectroelectrochemistry (5.1) to single-molecule detection (5.2). Analytical applications of SERS (5.3) include various aspects such as sensing, trapping, and solid-phase synthesis/detection. Separate subsections are devoted to bioanalytical applications (5.4) including SERS labels, with a focus on the detection of nucleic acids and proteins. The examples described in the various sections were chosen in order to illustrate and highlight the underlying concepts and strategies by discussing experimental and theoretical results from key publications. The last section contains conclusions and the attempt to outline potential future directions of SERS (Section 6). Readers who are predominantly or exclusively interested in chemical applications may want to skip Sections 2 to 4 and start directly start with Section 5. Please take home at least the most basic "equation": SERS = high molecular specificity of Raman spectroscopy + metal nanostructures supporting localized surface plasmon resonances + high sensitivity.

The choice of contributions highlighted in this Review article on concepts and chemical applications of SERS is naturally subjective. I must apologize to all colleagues whose work is not described in detail and not cited here. Please consult the many excellent review articles, monographs, and the original research articles cited therein for a complete overview on the extensive literature on SERS.

2. A Brief Tutorial on SERS

In comparison to normal Raman spectroscopy, SERS additionally requires the presence of metal nanostructures as an integral component. For understanding SERS, we therefore need to consider not only the interaction between light and molecules/matter, but also that between light and metal nanostructures.[9,11,13,20–24] The optical properties of metal nanostructures are the central topic of plasmonics. This term, a hybrid of plasma oscillations (plasmons) and elec-

[*] Prof. Dr. S. Schlücker
Fakultät für Chemie, Universität Duisburg-Essen
Universitätsstrasse 5, 45141 Essen (Germany)
E-mail: sebastian.schluecker@uni-due.de
Homepage: http://www.uni-due.de/schluecker-lab/

tronics, indicates the coupling of photons to charge density oscillations of the conduction electrons in metals. In this brief tutorial addressed to the general chemical audience, a simplified and in most cases qualitative description is used, which is often sufficient to capture the most important concepts.

First, it is necessary to recall the basic physics of driven or forced oscillations. A well-known example in classical mechanics is the driven harmonic oscillator. Consider, for instance, a suspension bridge oscillating with large amplitude due to an external periodic driving force, e.g., the wind ("resonance catastrophe"). In the harmonic oscillator model, the eigenfrequency $\omega = (k/\mu)^{1/2}$ of the oscillator is solely determined by the force constant k and the reduced mass μ of the system. In analogy to this mechanical example, laser light as an electromagnetic wave (external driving force) can also resonantly excite the delocalized conduction electrons in a metal (plasma oscillations). The resonance frequency ω_{max} of the plasma oscillations (plasmons) in the metal nanostructure depends, among other parameters, on the dielectric functions of the metal $\varepsilon_{metal}(\omega)$ and the surrounding medium $\varepsilon_m(\omega)$. For colloidal silver (yellowish) and gold (reddish color), plasmon peaks are observed in the visible region and can therefore be excited at optical frequencies (ca. 10^{14}–10^{15} Hz). Upon resonant excitation, the oscillating electric field of the incoming laser radiation with angular frequency ω_{inc} and amplitude E_0 drives an oscillation of the conduction electrons, e.g., in a gold nanoparticle (Figure 1 A), leading to a charge separation. This type of resonance is termed dipolar localized surface plasmon resonance (LSPR). The magnitude of the induced dipole $\mu_{ind(metal)}$ is determined by the polarizability of the metal sphere α_{metal} and the incident electric field strength $E(\omega_{inc})$: $\mu_{ind} = \alpha_{metal} E_0(\omega_{inc})$. The sign of the localized induced dipole μ_{ind} changes periodically with the angular frequency ω_{inc} of the electromagnetic wave as the external driving force. Overall, a Hertzian dipole (see electric field lines in Figure 1 A) on the nanoscale, i.e., a nanoantenna, has been generated, which can emit radiation at the same frequency ω_{inc} (green color in Figure 1 A and B). In other words: we have qualitatively described resonant elastic light scattering off a metal sphere, leading to an increased local electric field $E_{loc}(\omega_{inc})$ in the vicinity of the metal particle relative to the incident electric field $E_0(\omega_{inc})$ (see Section 3.1). Please differentiate between absorption and scattering as well as the extinction as the sum of both; only the scattering component is discussed here since it is exploited for the electromagnetic enhancement of Raman scattering in SERS (vide infra).

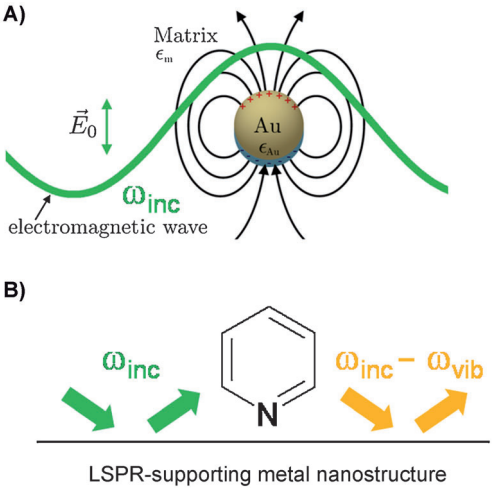

Figure 1. Electromagnetic enhancement in SERS. A) A gold nanoparticle acts as a nanoantenna by excitation of a dipolar localized surface plasmon resonance (LSPR). B) Both the "incoming" field (ω_{inc}, green) and the "outgoing" field ($\omega_{inc}-\omega_{vib}$, orange) are enhanced by elastic light scattering off the LSPR-supporting metal nanostructure.

Second, we need to consider the interaction of the local electric field $E_{loc}(\omega_{inc})$ with a molecule near the surface of the metal sphere (Figure 1 B). Similar to a dipole induced in the metal sphere, also dipoles in molecules can be induced: $\mu_{ind} = \alpha_{molecule} E_{loc}(\omega_{inc})$. The induced dipole moment μ_{ind} and the incident local electric field $E_{loc}(\omega_{inc})$ are vectorial properties, while the electronic polarizability $\alpha_{molecule}$ of the molecule, which connects the two, is a tensor of rank two with nine components; the tensor is often symmetric and only six components are relevant. The occurrence of inelastic light scattering can be explained by classical theory in terms of a modulation of the incident electric field $E_{loc}(\omega_{inc})$ by a vibrating molecule with angular eigenfrequency ω_{vib}. Three dipole components occur: $\mu_{ind}(\omega_{inc})$, $\mu_{ind}(\omega_{inc}-\omega_{vib})$, and $\mu_{ind}(\omega_{inc}+\omega_{vib})$, which correspond to Rayleigh, Stokes Raman, and anti-Stokes Raman scattering, respectively.

Quantum mechanics is required to explain the occurrence of only discrete lines as well as the different intensities for Stokes and anti-Stokes Raman scattering. In Figure 1 B the Stokes Raman scattering with angular frequency $\omega_{inc}-\omega_{vib}$ for one particular vibrational mode out of the total of $3N-6$ normal modes (for nonlinear molecules) or $3N-5$ normal modes (for linear molecules) is shown. This frequency-shifted radiation at $\omega_{inc}-\omega_{vib}$ (left orange arrow in Figure 1 B) itself can excite a LSPR of the metal colloid in Figure 1 A. Again, elastic light scattering off the metal sphere can take place (right orange arrow in Figure 1 B) and the emitted radiation is detected in the far field. This picture is not limited to the metal colloids discussed here, but can be applied to all nanostructures that support LSPRs (see Section 4).

The overall SERS intensity depends on both the "incoming" (ω_{inc}) and the "outgoing" ($\omega_{inc}-\omega_{vib}$) field: $I_{SERS} = I_{inc}(\omega_{inc}) I(\omega_{inc}-\omega_{vib}) = |E_{inc}(\omega_{inc})|^2 |E(\omega_{inc}-\omega_{vib})|^2$. Optimal

Sebastian Schlücker was born in Essen (Germany) in 1973, the year when SERS was first observed in Southampton (UK). He received his PhD in physical chemistry from Würzburg University in 2002. After postdoctoral studies at the NIH (Bethesda, USA) and his Habilitation, he became Professor of Experimental Physics at Osnabrück University in 2008. Since 2012 he has been Professor of Physical Chemistry at the University Duisburg-Essen. His field of research is nanobiophotonics, in particular the physics and chemistry of single plasmonic nanostructures and their applications in biomedicine and ultrasensitive chemical analysis.

SERS enhancements therefore require that both the incident radiation at ω_{inc} and the Stokes Raman shifted radiation at $\omega_{inc}-\omega_{vib}$ are in resonance with the plasmon peak of the metal nanostructure. For $\omega_{inc} \gg \omega_{vib}$ or $\omega_{inc} \approx \omega_{inc}-\omega_{vib}$, in other words when ω_{inc} (incident laser light) and $\omega_{inc}-\omega_{vib}$ (Stokes Raman scattering for one particular vibration/Raman band) are close to each other, the widely used $|E|^4$ approximation of the SERS intensity results: $I_{SERS} \approx |E(\omega_{inc})|^4$. This approximation is typically good for ω_{inc} in the blue and green region, but not for the red or even near-infrared region.

Further, since the electric field strength of dipolar radiation scales with $E(r) \sim 1/r^3 = r^{-3}$, a SERS distance dependence of $I_{SERS} \sim 1/r^{12} = r^{-12}$ is both theoretically expected and experimentally observed (see Section 3.4). In other words: SERS is a truly surface-selective effect. Also the orientation of the molecule relative to the surface normal is important and can be detected: flat versus tilted versus perpendicular orientations give rise to distinct SERS signatures since the various vibrational bands of the adsorbed molecule, e.g., bands due to in-plane and out-of-plane modes of an aromatic compound (cf. Figure 1 B), are differently enhanced according to the corresponding components of the tensor $\alpha_{molecule}$.

The electromagnetic enhancement discussed above is the dominant enhancement mechanism for SERS and it involves only the metal nanostructure and photons, or to be more drastic: this purely physical effect does not require the presence of molecules (see Sections 3.1 and 3.2), if at all then only for the "frequency conversion" from ω_{inc} to $\omega_{inc}-\omega_{vib}$ (Figure 1 B). The central message here is that very high local electric fields are responsible for the significantly increased signal strength observed in SERS relative to normal Raman scattering. An increase of $E_{loc}/E_{inc} = 100 = 10^2$, for example, results in an overall increase of the SERS intensity by a factor of $(E_{loc}/E_{inc})^4 = (10^2)^4 = 10^8$ or one hundred million. In other words: moderate increases of E_{loc}/E_{inc} lead to huge SERS enhancements (see Sections 3.2 and 3.3). This number—10^8 in this example—is termed the SERS enhancement factor (EF); it is a very central figure in SERS for quantifying the overall signal enhancement. The experimental determination of SERS EFs requires measurements of the SERS intensity for the adsorbed molecule on the metal surface, relative to the normal Raman intensity of the same, "free" molecule in solution. The two intensities must be normalized to the corresponding number of molecules on the surface (SERS) and in solution (conventional Raman), respectively.

SERS is a molecular spectroscopic technique, which is based on the plasmon-assisted scattering of molecules on or near metal nanostructures that support LSPRs. Molecules are therefore an intrinsic and integral component of SERS and it is this wealth of chemical/molecular, and to a certain extent also structural information, which makes SERS such a powerful molecular spectroscopic technique. In other words: there is no SERS without molecules, but there is also no SERS without plasmonic nanostructures (plus light, of course). For a theoretical treatment of SERS it is therefore mandatory to also include the interaction of molecules with the metal surface and to consider the electronic properties of the corresponding adsorbate. The corresponding effects are summarized under the term "chemical" enhancement (see Section 3.5).

The next section covers many facets of SERS only briefly discussed in this tutorial. Important recent results from original research, which have further increased our knowledge on SERS during the last years, are highlighted.

3. Understanding SERS: Fundamental Aspects

3.1. Field Enhancements in Noble Metal Nanostructures: Theory and Experiment

3.1.1. Electromagnetic Enhancement: Theory for Single Spheres and Their Dimers

The single-molecule SERS experiments reported in 1997[3,4] stimulated theoretical investigations on the magnitude of the electromagnetic EF in metal colloids,[25] in particular the origin of the very high EFs necessary for generating single-molecule SERS.[26] Figure 2 shows the electromagnetic EF ($|E|^4$) calculated for dimeric configurations of two spheres (top) and two polygons (bottom), together with those of the corresponding isolated single particles (right column).[26] The 2D representation is a horizontal cross section. The color scale is logarithmic and EFs outside the range 10^0–10^8 are shown in dark blue and dark red, respectively.

From these calculations it becomes evident that isolated particles (right column), either single spheres or single polygons, do not exhibit very large EFs, which are typically on the order of only 10^3 and are therefore not relevant for single-molecule SERS. Very high EFs are only observed in highly localized regions ("hot spots") in the junctions between two particles. The left and middle columns show dimers with a particle separation of 1 and 5.5 nm, respectively. When the gap size is increased from 1 nm to 5.5 nm, the maximum EF in the hot spot decreases from ca. 10^{10}–10^{11} by three orders of magnitude to ca. 10^7–10^8 (better represented in Figure 2 of Ref. [26]). A very close spacing between particles is therefore beneficial for the generation of extremely strong, but at the same time also highly spatially localized electric field enhancements. Time-dependent DFT calculations predict that at very small distances (<1 nm) quantum effects such as electron tunneling across the dimer junction modify the optical response, leading to electromagnetic field enhancements that are drastically reduced compared to the classical predictions.[27]

For other wavelengths the spatial dependence of the enhancement factors is the same, but their magnitude is different.[26] Also calculations for gold were performed and the corresponding enhancements are smaller. Silver is therefore plasmonically more active than gold and commonly used for single-molecule and ultrasensitive SERS experiments. On the other hand, gold is chemically more inert, which is preferred in applications where the chemical stability of the colloid is more important than maximum enhancement. Also, the enhancements of Ag and Au become similar in the red to near-infrared.[20]

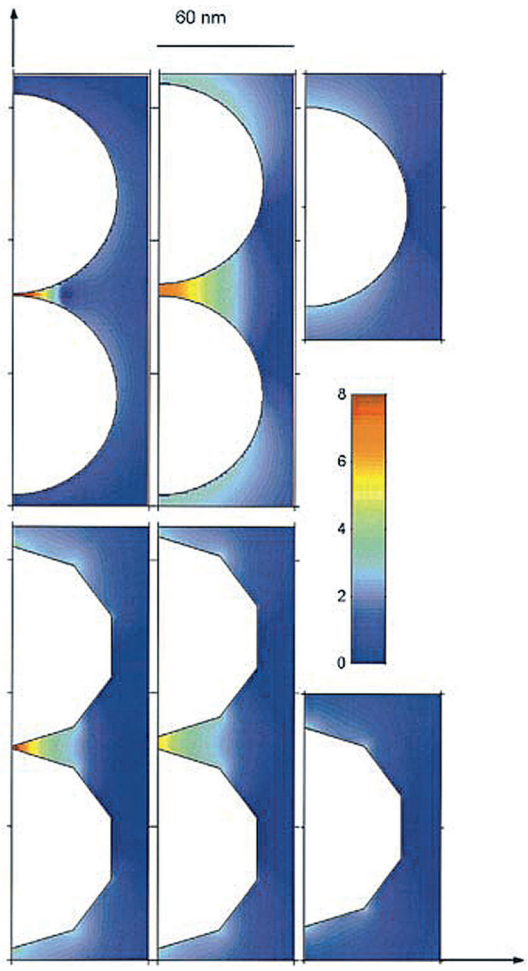

Figure 2. Electromagnetic enhancement contribution factors (color-coded log scale) for dimers of silver nanoparticles (left and middle columns) compared with single isolated silver nanoparticles (right column). From Ref. [26].

3.1.2. *Probability Distribution of Calculated Enhancement Factors in SERS*

Hot spots are highly spatially localized regions exhibiting extreme field enhancements (see dark red regions in Figure 2). In contrast, sites with moderate enhancement factors are much more frequent (see dark blue regions in Figure 2). The probability of accidentally finding a molecule in a hot spot, i.e., positioned exactly in the gap between the particles of a dimer in Figure 2, is therefore very small. In contrast, it is much more likely to find a molecule somewhere on the surface of one of the two particles, where it experiences only moderate enhancements. The corresponding probability distribution—the statistical distribution of probabilities to find a certain EF—exhibits a typical long-tail behavior[28,29] (Figure 3) and reflects the qualitative trends discussed above: moderate EFs have much higher probabilities than extreme EFs. Please note that the representation is double logarithmic, i.e., both x values (EFs) and y values (probability) are plotted on a logarithmic scale.

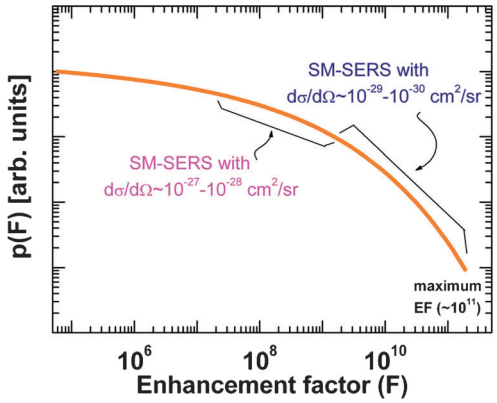

Figure 3. Long-tail probability distribution of enhancement factors (EFs) in SERS. From Ref. [29].

Molecules with relatively high differential Raman scattering cross sections $d\sigma/d\Omega$ on the order of 10^{-27}–10^{-28} $cm^2\,sr^{-1}$ such as dyes require enhancement factors of "only" 10^7–10^8 for single-molecule SERS. In contrast, molecules with "normal" differential Raman scattering cross sections $d\sigma/d\Omega$ on the order of 10^{-29}–10^{-30} $cm^2\,sr^{-1}$ (not dyes, usually referred to as "nonresonant" molecules) require the extremely large but extremely rare EFs of 10^9–10^{11} for single-molecule SERS. Note that the maximum EF in Figure 3 is ca. 10^{11}.

It is important to keep this probability distribution of EFs in mind since it stresses that the extreme EFs are very rare. In the case of dimers, for instance, only the molecules located in the hot spot (see Figure 2) experience an extremely high EF, while molecules located elsewhere experience significantly lower EFs. A simple calculation illustrates this: a single molecule in a hot spot with an EF of 10^{10} gives the same Raman signal as 10 million molecules experiencing only a moderate EF of 10^3.

Hot spots do not only occur in the gap between two particles, but also at sharp edges and tips;[30–33] the latter is the basis for tip-enhanced Raman scattering (TERS).[34–36]

3.1.3. *Experimentally Determined Site Distribution of Enhancements*

The probability distribution of enhancement factors in Figure 3 is based on calculations and needs to be confirmed by experiment. Ensemble measurements based on linear Raman spectroscopy are not capable of determining the site distribution of enhancements since only average values are obtained. Therefore, nonlinear spectroscopy or a sequential, molecule-by-molecule approach is required. The latter approach would probably lack the sensitivity required to also observe the cold sites. Other approaches include photobleaching and the vibrational pumping of adsorbed dye molecules. Both approaches lack a sharp threshold. In contrast, photochemical hole burning (PHB) provides a sharp electric field threshold as a cut-off, which significantly simplifies the corresponding analysis for extracting the site distribution of enhancements.[37]

The experimental approach is depicted in Figure 4.[37] The SERS-active nanostructure is a Ag film over nanospheres (AgFON, Figure 4A), which comprises 330 nm nanospheres

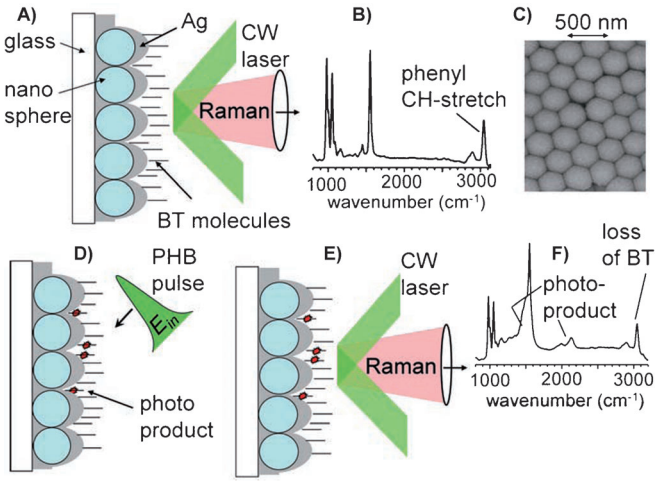

Figure 4. Experimental approach for determining the site distribution of enhancements in SERS, using photochemical hole burning (PHB) of benzenethiol (BT) molecules on a Ag film over nanospheres. From Ref. [37].

coated by a 150 nm thick film of silver (SEM picture in Figure 4C). The Ag surface of the AgFON is covered by a self-assembled monolayer of benzenethiol (BT) as a probe molecule. Since benzenethiol in solution does not exhibit an electronic absorption band near the laser excitation wavelength of 532 nm employed in this study, molecular electronic resonances are assumed to be negligible and it is believed that mostly the electromagnetic enhancement contributes in this case.

The SERS spectrum of the BT probe molecule (Figure 4B) obtained with green continuous-wave (cw) laser excitation (Figure 4A) exhibits the characteristic vibrational Raman peaks of aromatic compounds, including contributions from phenyl CH-stretching motions giving rise to peaks around 3000 cm^{-1}. Upon illumination with an intense 1 ps laser pulse (PHB pulse in Figure 4D), BT molecules are converted into a photoproduct. It is important to note again that the PHB laser approach provides the necessary control and selectivity for experimentally probing the distribution of site enhancements; photodamage will only occur at those sites with the highest enhancement, followed by molecules at sites with progressively smaller enhancements. In other words, the power of the PHB pulses makes it possible to selectively probe only those molecules which are located at sites with an enhancement higher than the sharp threshold. After photoconversion, the composition of the self-assembled monolayer (SAM), now containing a mixture of photoproduct and BT molecules, can be interrogated by a low-power green cw laser (Figure 4E).

The SERS spectrum of the illuminated SAM on the AgFON substrate exhibits new vibrational Raman bands at 1550 cm^{-1} and 2100–2200 cm^{-1} due to the presence of the photoproduct (Figure 4F). At the same time, the intensity of the CH-stretching band at 3000 cm^{-1} indicates the loss of BT molecules (Figure 4F). The comparable SERS intensities of the photoproduct and BT, together with the lack of apparent effects on the AgFON surface plasmon resonance due to continued PHB pulse radiation, support the conclusion that PHB pulses do not change the AgFON as a SERS substrate, but only initiate the photoconversion of BT.

The (PHB 1 ps 532 nm)-pump/(Raman cw 532 nm)-probe experiment was performed at different laser power densities and the intensity of the aromatic CH-stretch peak at 3000 cm^{-1} was used as a spectrally isolated marker for monitoring the formation of the photoproduct (Figure 4F). After 1000 pulses, a constant CH-stretch Raman signal is observed, indicating that the intensity drop caused by photodamage of BT is complete.

A model was developed, by which—starting with the assumption that each PHB pulse has a constant probability for inducing photodamage—the distribution of the site enhancement can be calculated. A basic conclusion from the resulting equation is that the relative intensity I/I_0 is inversely proportional to E_{in}; in other words, the higher the field strength E_{in} (laser power density), the lower the BT intensity due to the increased formation of the photoproduct. The plot of I/I_0 as a function of $1/E_{in}$ for the experimental data is shown in Figure 5, demonstrating the agreement with the model.

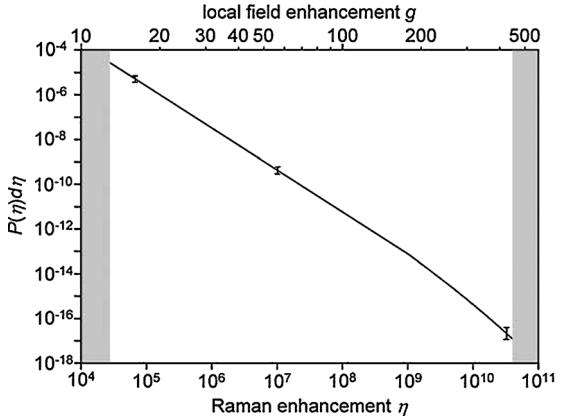

Figure 5. Probability distribution of Raman enhancement factors determined from data obtained in the experiment depicted in Figure 4. From Ref. [37].

It was calculated that only 63 out of 1 million molecules (!) at hot sites (enhancement $> 10^9$) contribute to 24% of the overall SERS signal, while the coldest sites contain 61% of the molecules but contribute just 4% to the overall SERS intensity.[37] This approach can, in principle, be applied to any SERS substrate.

3.1.4 Experimentally Determined Distance Dependence of SERS in a Dimer Model

Molecules in the gap between two silver or gold nanoparticles exhibit SERS intensities several orders of magnitude

higher than that of normal Raman scattering, in some cases down to the single-molecule level. Parameters such as the dependence of the SERS signal on the size and shape of the nanoparticle (NP) dimer as well as the role of the incident light polarization have been investigated. Electromagnetic theory predicts that the distance between the two particles critically determines the field enhancement in the hot spot of the dimer. Experimentally, however, it is very difficult to achieve distance control on the sub-nanometer scale since methods for precisely and flexibly adjusting the separation during the SERS measurements are lacking.

This has been realized by a combination of SERS and a mechanically controllable break junction method for measuring the SERS signals of molecules located within a nanogap between two gold electrodes on a Si chip (Figure 6).[38] The tips of the two gold electrodes represent

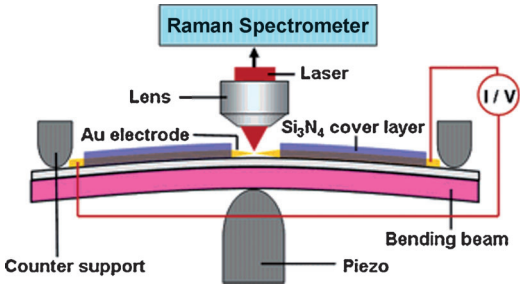

Figure 6. Experimental setup for mechanical break junction Raman spectroscopy. From Ref. [38].

a model for a gold dimer with a well-defined gap. The gap size can be controlled mechanically by a piezoelectric transducer with sub-Ångström resolution (Figure 6). This precise and stable adjustment of the separation between the electrodes is a prerequisite for monitoring the variation of SERS as a function of the gap size in a dimer since it is the distance between the two individual particles (here: the two electrodes) which critically determines the electromagnetic enhancement.

Results from SERS measurements with sub-Ångström distance control are shown in Figure 7.[38] When the nanogap is decreased from 0.8 to 0.6 and finally to 0.4 nm, the SERS signal of 1,4-benzenedithiol continuously increases. Similar results were obtained with other probe molecules such as 4-aminothiophenol. At the present stage, the success rate for observing gap-size-dependent SERS spectra is about 20%, with room for experimental improvements.

It is likely that many interesting studies will follow from this combined mechanical break junction/SERS approach, with applications in single-molecule vibrational spectroscopy, molecular electronics, sensing, and other areas, in which the synergy of sub-nanometer distance control and molecular identification, orientation, and—to a certain extent—structural information can be exploited.

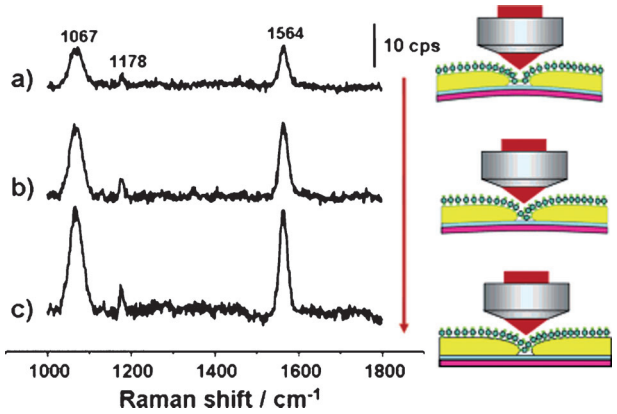

Figure 7. SERS spectra of 1,4-benzenedithiol for different gap junctions: a) 0.8 nm, b) 0.6 nm, and c) 0.4 nm. From Ref. [38].

3.2. Beyond Single Spheres and Dimers: From Trimers to Superstructures

3.2.1. Experimental Structure–Activity Relationships in Gold Dimers and Trimers

Structure–activity relationships are widely used in physical organic chemistry; however, their establishment for plasmonic nanostructures and SERS is more challenging due to variations in the size of the colloidal particles (monodispersity), their state of aggregration (cluster size), and their geometrical arrangement (e.g., linear versus L-shaped trimer).[39,40] Correlated LSPR/HR-TEM/SERS experiments on dozens of individual glass-coated gold dimers and trimers were performed in order to identify the most important physical parameters that determine very high EFs in these hot-spot-containing structures. Figure 8 shows results from correlated LSPR/HR-TEM/SERS experiments on glass-coated dimer and trimer nanoantennas.[39] The two dimers in Figure 8a and b exhibit similar structures, but very different LSPR spectra. However, the corresponding EF values are within one order of magnitude. This suggests that the gap size is critically important for the EF of the nanostructure, confirming results reported earlier (see literature citations in Ref. [39]). Also the trimers with linear (Figure 8c) and bent (Figure 8d) geometries have different LSPR spectra, but similar EFs. Since their EFs are similar to those determined for the dimers, the addition of hot spots does not seem to result in additional enhancement. In contrast to dimers, trimers exhibit a quasi-polarization-independent optical response.[41]

Overall, the correlated HR-TEM/SERS experiments demonstrated that all highly SERS-active dimer and trimer nanoantennas exhibited either coalesced or separated cores with gap sizes in the range <1 nm, a finding in accordance with results from finite element method (FEM) calculations.

3.2.2. Plasmonic 3D Superstructures through Self-Assembly of Satellites onto a Core

Dimers are characterized by a single hot spot in the junction and, due to their lower symmetry compared to

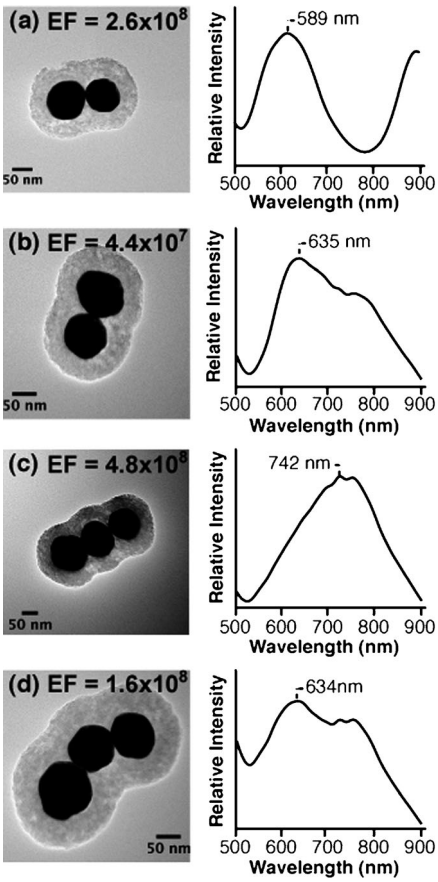

Figure 8. HR-TEM images and corresponding single-particle LSPR spectra of glass-coated dimers and trimers of gold nanospheres. From Ref. [39].

a single NP, they exhibit a highly anisotropic optical response; maximum signals are observed when the laser polarization is parallel to the dimer axis, while a perpendicular orientation does not lead to resonant excitation of the longitudinal plasmon mode. Building 3D plasmonic superstructures with more than two particles represents the next level of complexity and is an important topic in material science.[42–46] In particular approaches based on self-assembly are among the most promising bottom-up approaches. In contrast to dimers with only a single hot spot, assemblies can exhibit a series of hot spots (Figures 9 and 10). For N satellite spheres that surround a single central sphere (core) and touch each other, the number of hot spots is $2N-1=N$ (between satellites and core) $+N-1$ (between satellites); in other words, the number of hot spots scales linearly with the total number of spheres $(N+1)$. Additionally, a quasi-isotropic optical response—in contrast to the characteristic $|\cos\theta|^2$ dependency for dimers (where θ is the angle between laser polarization and dimer axis)—is theoretically expected[46] and has been demonstrated experimentally at the single-particle level.[41]

Figure 9 shows electron microscopy images from 3D SERS-active superstructures obtained by self-assembly. Gold particles (80 nm) were incubated with Raman reporters and encapsulated with a very thin silica shell (Figure 9a),[46]

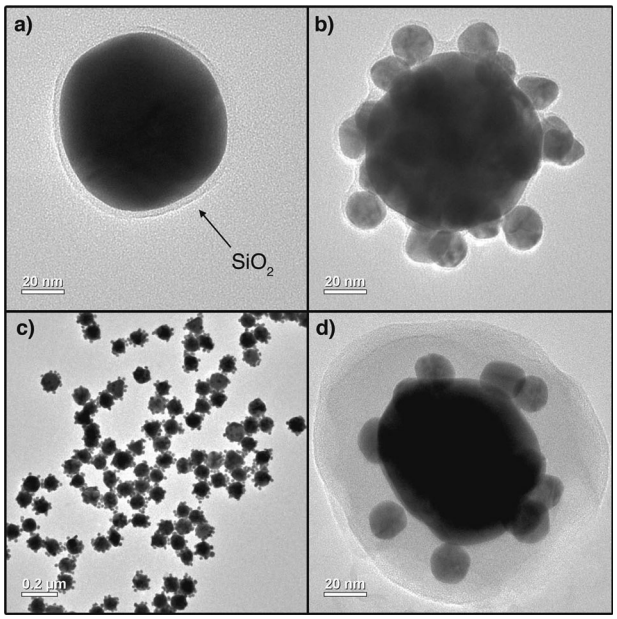

Figure 9. TEM images of a) a 80 nm gold core coated with an ultrathin silica shell, b,c) 3D superstructures with 20 nm gold satellites self-assembled onto the core, shown at high (b) and low (c) magnification, and d) a glass-coated 3D superstructure. From Ref. [46].

using a protocol described in Section 4.1.1. The ultrathin glass shell was then functionalized with a binary mixture of silanes, including an aminosilane. Negatively charged, citrate-stabilized 20 nm gold nanospheres were assembled onto this positively charged ($-NH_3^+$), glass-coated 80 nm core (Figures 9b,c). Finally, the 3D structure was stabilized by silica encapsulation (Figure 9d). Correlated HR-SEM/dark-field/LSPR/SERS experiments on individual 3D SERS-active superstructures together with finite element method (FEM) calculations (Figure 10) confirmed the plasmonic coupling between the core and the satellite particles, with hot spots occurring between core and satellites as well as between satellites. Such computer simulations are generally instructive for understanding the plasmonic coupling in complex metal nanostructures, in particular the occurrence of hot spots.

The next section describes direct experimental evidence of hot spots.

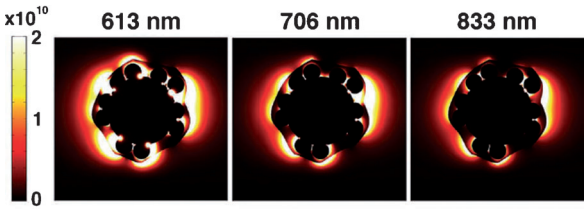

Figure 10. Spatial $|E|^4$ distribution in a 2D section of a 3D computer-generated model based on the single 3D superstructure in Figure 9d. Three different LSPRs at 613, 706, and 833 nm can be observed. From Ref. [46].

3.3. Experimental Evidence of Hot Spots: Isolating, Probing, and Localizing Hot Spots

3.3.1. Isolating and Probing the Hot Spot Formed between Two Silver Nanocubes

Calculations on dimers of nanospheres (cf. Section 3.1) have demonstrated that these objects are ideal candidates for obtaining very high field enhancements through the generation of hot spots in the junction between the two spheres. The examination of individual dimers even makes it possible to quantify the field enhancement in the hot spots and serves as valuable information for correlating the specific structure of the hot spot with the corresponding SERS intensity observed experimentally. Determining the contribution of molecules located in the hot spots is therefore of central importance. However, not only the molecules located in the hot spots—although they experience by far the largest enhancement, but they are few in number—also molecules at colder sites of the dimer contribute to the overall signal (cf. Sections 3.1.2 and 3.1.3 for the probability distribution of EFs). Thus, it is necessary to isolate the SERS signal contribution arising from molecules located in the hot spot from the rest, i.e., from molecules not located in the hot spot. Otherwise, only a lower average EF of an ensemble would be detected, rather than the actual higher EF_{dimer} for the hot spot.

Plasma etching is an elegant way of selectively removing molecules from the surface of metal nanostructures. This technique has been used to isolate the hot spot formed between two silver nanocubes for subsequent measurement of the SERS EF intrinsic to this particular hot spot.[47] First, it was demonstrated on single Ag nanocubes that plasma etching removes the probe molecules 4-methylbenzenethiol (4-MTB) and 1,4-benzenedithiol (1,4-BDT), both of which form a self-assembled monolayer (SAM) on the silver surface. Then, this approach was applied to nanocube dimers with a narrow gap between two nearly touching cubes (Figure 11). Upon immersion of the nanocube dimer in a solution of 4-MTB, a complete SAM on the entire surface of the dimer is formed (Figure 11 top). 4-MBT molecules located in the junction between the two cubes are considered as a multilayer resist relative to oxygen plasma. Removing 4-MBT molecules located in the hot spot therefore takes much longer than removing molecules outside the hot spot, for example, those exposed on the top faces of these cubes. Overall, plasma etching leads to the selective removal of molecules that are not located in the hot spot (Figure 11 bottom). Interestingly, only a slight reduction in SERS intensity due to the removal of molecules outside the hot spot is observed (Figure 12). This indicates that the major contribution to the overall SERS signal arises from the molecules in the hot spot, i.e., those molecules not been removed by plasma etching that experience the largest enhancement.

After plasma etching, the Ag nanocube dimer was immersed in a solution of 1,4-BDT as a second Raman probe molecule in order to demonstrate that no significant changes had occurred on the surface of the Ag cube dimer upon plasma etching. 1,4-BDT is a dithiol and strongly binds to the Ag surface, which is presumably the driving force for replacing 4-MTB from the hot spots.

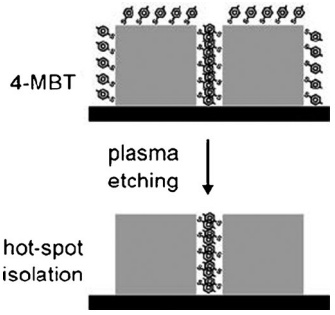

Figure 11. Isolation of molecules located in a hot spot by plasma etching. A self-assembled monolayer of 4-methylbenzenethiol (4-MBT) is formed on the surface of a dimer of silver nanocubes. Plasma etching removes the surface-bound molecules except those located in the junction of the cubes. From Ref. [47].

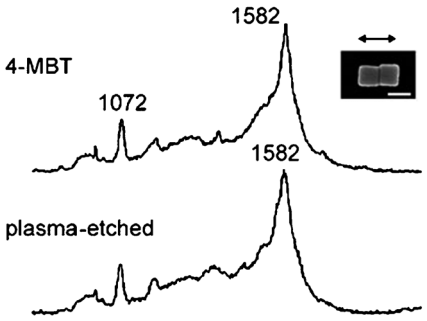

Figure 12. SERS spectra of 4-MBT before and after plasma etching, recorded for parallel laser polarization with respect to the dimer axis. The signal decreases only marginally, demonstrating the overwhelming contribution of 4-MBT molecules located in the hot spot (cf. Figure 11). From Ref. [47].

Quantification of the EF requires an estimation of the number of molecules present in the hot spots. The authors assumed that each 4-MBT molecule occupies a circular area with a diameter of 0.49 nm. As the nanocubes have an edge length of 100 nm, this corresponds to roughly 200 layers of 4-MBT molecules in the vertical direction (Figure 11). Based on these assumptions, an enhancement factor of $EF_{dimer} = 2.2 \times 10^7$ was determined.

Molecules present in a hot spot not only experience maximum enhancements (EF_{dimer}), their SERS signal also exhibits a characteristic polarization dependence. Maximum SERS signals are observed when the laser polarization is aligned parallel to the dimer axis (Figure 12 top). For other orientations, such as 45° between the long dimer axis and the laser polarization, less efficient excitation of the corresponding plasmon mode occurs and the experimentally observed SERS intensity is lower than that with parallel orientation. For a perpendicular orientation the SERS intensity even decreases further (Figure 13 top). In this case, the molecules located in the hot spot do not further contribute to the overall SERS signal, which is now determined by contributions from molecules outside the hot spot (Figure 13 bottom).

The presented plasma etching methodology is powerful since it is possible to isolate an individual hot spot by

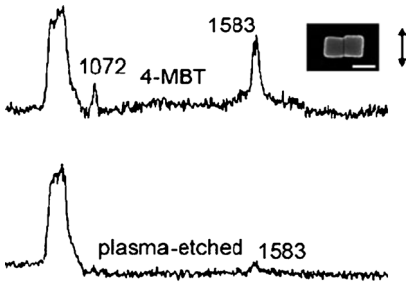

Figure 13. SERS spectra of 4-MBT before and after plasma etching, recorded for perpendicular laser polarization with respect to the dimer axis. The signal decreases drastically, demonstrating that the 4-MBT molecules are located in the hot spot (cf. Figure 11). From Ref. [47].

selectively removing molecules from regions outside the hot spot, subsequently probe the properties of the hot spot, and determine its enhancement factor together with its polarization-dependent behavior.

3.3.2. *Direct Evidence for High Spatial Localization of Hot Spots in SERS*

The controlled deposition of molecules directly in the hot spot and at well-defined distances from it is the basis for directly mapping the high spatial localization of SERS hot spots. When SERS is measured on the same type of analyte deposited at a different position on a different nanostructure with identical dimensions, the corresponding SERS intensities can be compared. Figure 14 depicts the experimental methodology for selectively depositing amorphous carbonaceous nanoparticles (CNPs) at different positions in a gold nanoslit cavity: directly in the slit (top right), on the side wall (middle right), and on the top edge (bottom right).[48] CNPs are used as the analyte for SERS and are deposited locally by the decomposition of a gaseous precursor, in this case hexadecane. The gas-to-solid phase conversion is mediated by an electron beam, which guarantees selective deposition with high spatial localization (Figure 14a top left). Cross-sectional images of a CNP deposited inside the nanoslit obtained with energy-filter transmission electron microscopy demonstrated

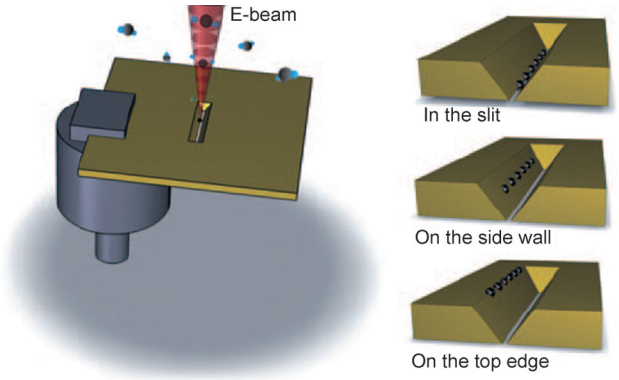

Figure 14. Local deposition of carbonaceous nanoparticles (CNPs) in a nanoslit by decomposition of gaseous precursors mediated by electron beam lithography. From Ref. [48].

the high spatial control over deposition. Also, the optical field enhancement distribution in the nanoslit cavity was obtained from finite difference time domain (FDTD) calculations. The localization of the hot spot at the nanoslit is clearly visible in the corresponding false-color images. For calculating the SERS enhancement, the $|E^4|$ approximation can be used (Section 2). For example, in this case an increase in SERS intensity by a factor of $250^2 = 62\,500$ was calculated.

Figure 15 shows Raman images of the CNPs deposited at the three different locations (cf. Figure 14): directly in the nanoslit (NS), on the side wall, and on the top edge of the NS. The Raman images, in which the nanoslit area is indicated by a white box, clearly demonstrate that high SERS signals are observed only when the CNPs are deposited directly in the plasmonically active Au nanoslit. The corresponding SERS spectra exhibit the broad spectral feature of amorphous carbon and demonstrate the following order of experimentally observed SERS intensities as a function of CNP location in the Au nanoslit (NS): in the NS $\gg$ on the NS edge $>$ top edge.

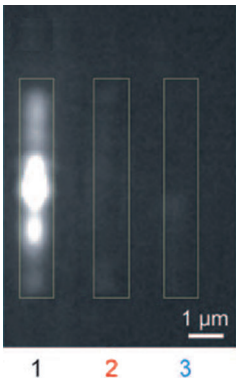

Figure 15. Raman images of CNPs located 1) in the nanoslit (NS), 2) on the side wall, and 3) on the top edge of the NS (cf. Figure 14), demonstrating the strong enhancement for CNPs located directly in the hot spot at the bottom of the slit. From Ref. [48].

Overall, these results reveal the overwhelming contribution to the overall SERS signal from only few analyte molecules located directly in the hot spot.

3.4. *Dependence of Enhancements on the Distance between the Molecule and the Metal Surface*

The distance between the molecule and the metal surface is a very important parameter, which determines the SERS signal strength. A simple model for the distance dependence of the enhancement treats it as a near-field interaction of an oscillating dipole in the center of a sphere with a molecule at distance R from the center of the sphere, yielding a R^{-12} distance dependence.

3.4.1. *Tip-Enhanced Measurements*

Figure 16 shows results from tip-enhanced Raman scattering (TERS) on single-walled carbon nanotubes (SWCNTs) with a sharp tip (Figure 16b), in which the tip was retracted from the surface (Figure 16a).[49] The relative TERS intensities clearly follow an inverse power law. The analytical expression describing the Raman intensity profile also contains several other parameters: the lateral distance between the molecule and the central point beneath the tip, the tip radius, and a tunneling gap width.[50] The tip radius (typical value: 20 nm) was much smaller than the laser excitation wavelength.

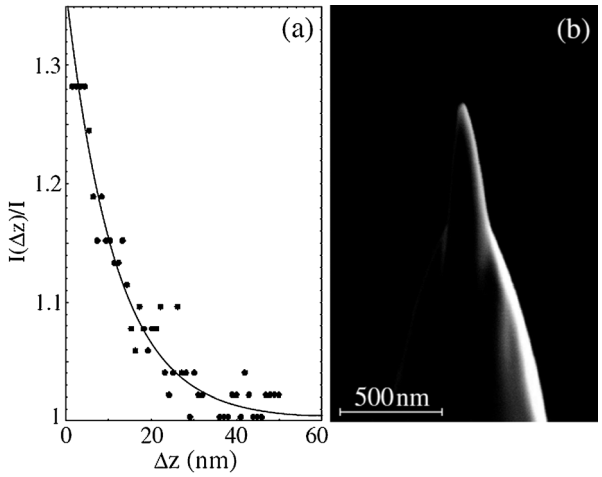

Figure 16. a) Dependence of the Raman intensity of the G' peak of single-walled carbon nanotubes (SWCNTs) on the separation between the tip and the SWCNT. b) SEM image of a sharp tip. From Ref. [49].

3.4.2. *Atomic Layer Deposition*

In TERS experiments the plasmonically active tip can be precisely retracted in the z direction using AFM or STM in order to determine the distance dependence of the signal strength. One way to achieve this in SERS experiments is to use a spacer with a variable length ranging from a few Ångströms to a hundred nanometers. The coated plasmonic surface must to be pinhole-free in order to avoid direct interaction with the probe molecule. Atomic layer deposition (ALD) is a spacer fabrication method that produces highly uniform and controlled thin films. Figure 17 shows results from SERS on pyridine deposited on Al_2O_3 multilayers onto a AgFON substrate (see Section 4.2.2.2).[51] The intensity of the 1594 cm^{-1} band of pyridine is plotted as a function of the Al_2O_3 thickness. The data can be fitted to a R^{-10} power law. In contrast to the TERS experiments, which probed only a single molecule/SWCNT (Section 3.4.1), here the total surface area (scaling with R^2 for a sphere; cf. model above) is probed (i.e., 10^{-12} per molecule $\times$ 10^2 molecules $= 10^{-10}$ overall).

A different approach was based on molecular rulers using DNA and gold nanoshells as a plasmonic substrate.[52]

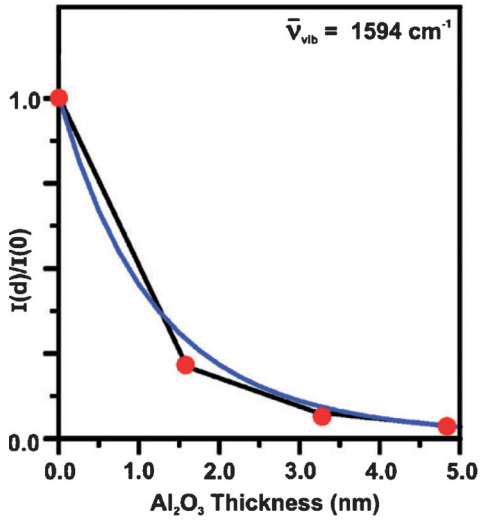

Figure 17. Dependence of the Raman intensity of the 1594 cm^{-1} peak of pyridine on the thickness of the Al_2O_3 overlayer/spacer on a Ag film over nanospheres. From Ref. [51].

3.5. *Beyond Plasmonics: "Chemical" and Resonance Raman Contributions*

Current models explaining the experimentally observed signal enhancements in SERS are based on two contributions: the electromagnetic (EM) and the "chemical" enhancement (CE). The EM mechanism describes the enhanced local electromagnetic fields due to resonant excitation of plasma oscillations (plasmons) in the metallic nanostructure. This purely physical effect is by far the most dominant contribution, with standard SERS EFs in the wide range of 10^3–10^{10}.[20] Please recall the basic formula for the induced dipole moment, $\mu_{ind} = \alpha_{molecule} E_{loc}(\omega_{inc})$, which was used for the classical description of the Raman effect and note that the EM enhancement contributes through the increase of the local electric field E_{loc}. Actually, the local field enhancements arising from the excitation of LSPRs do not require the presence of molecules at all; the latter are only necessary for the "frequency conversion" from ω_{inc} to $\omega_{inc}-\omega_{vib}$ by means of Raman/inelastic light scattering (Figure 1B). A direct interaction between the molecule and the underlying metal surface, however, is not covered at all by this effect.

In contrast, the CE mechanism is related to the electronic properties of the adsorbate and acts by means of the increase in the electronic polarizability $\alpha_{molecule@metal}$ of the adsorbed molecule on the induced dipole μ_{ind}; CE enhancements, of the order of one to three orders of magnitude, are significantly smaller than the EM contribution. First, charge transfer (CT) between the molecule in its electronic ground state and the metal can change the polarizability of the molecule, resulting in a change of the Raman scattering cross-section of the molecule. The same effect occurs in coordination chemistry when ligand molecules are bound to a metal center. Second, the energy levels of the adsorbate molecule usually differ from those of the molecule in its unbound or "free" state. For instance, let us assume that the laser excitation wavelength does not coincide with an electronic absorption band of the "free" molecule, but does coincide with one of the adsorbed molecule. The resonant excitation of electronic transitions in molecules is known as resonance Raman (RR) scattering. At the same time, new electronic excitation channels can arise through a photoinduced CT mechanism, for example through CT from the metal to the adsorbed molecule. This is an integral component of the so-called CT resonance model, in which the transition energies depend on the energy separation between molecular and metallic energy levels. Disentangling these different processes experimentally is not trivial (Section 3.5.1) and in some cases even not possible.

Electronic structure calculations on molecules at metal surfaces/clusters are therefore an extremely valuable approach for investigating the role of the above-mentioned contributions separately under controlled and a priori well-

defined conditions.[53,54] The interfacial structure of a molecule–metal cluster and its optical properties can be modeled at the atomic scale by electronic structure calculations. Various parameters can be investigated, including the bonding situation between the molecule and the metal nanostructure, the effect of surface roughness at the atomic scale, the effects of molecular and charge-transfer resonances, the effects of the incident laser wavelength, and the wavelength of Stokes Raman scattering; in other words: electronic structure modeling can be used to disentangle the role of the individual contributions under the controlled and well-defined conditions of a computer "experiment" (Section 3.5.1).

3.5.1. Electronic Structure Calculations on a Model System: Pyridine@Ag_{20}

Due to the high computational demands of electronic structure methods, most calculations have adopted small clusters to mimic metal surfaces. In addition, most calculations have considered only static Raman scattering and could therefore only model the chemical enhancement. Time-dependent density functional theory (TDDFT) and a short-time approximation to the Raman scattering cross-section was applied to pyridine (C_{2v} symmetry) bound through the nitrogen atom in a perpendicular manner to the Ag_{20} cluster (T_d symmetry).[53] Two different configurations, both with C_s symmetry, were examined because of their very different local chemical environments: the surface (S) complex with binding of pyridine onto one of the four faces of the tetrahedral Ag_{20} cluster, representing a (111) surface of face-centered cubic (fcc) silver (Figure 18a) and the vertex (V) complex with

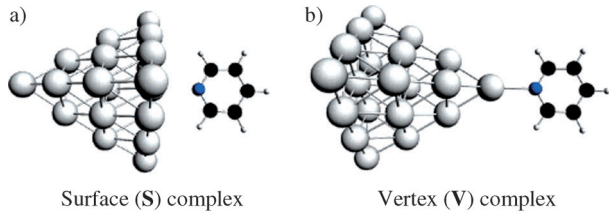

Figure 18. The Py@Ag_{20} cluster can form a) a surface complex or b) a vertex complex. From Ref. [53].

pyridine binding onto one the vertexes of the Ag_{20} cluster, representing an ad-atom site (Figure 18b). In both complexes a transfer of electron density from the pyridine ring and the central silver atom into the N bonding region is observed, in agreement with the overall charge transfer from pyridine to the Ag_{20} cluster. The N–Ag bond length in the V complex is shorter than in the S complex, indicating a stronger interaction in the ad-atom situation.

The Raman spectra of pyridine in the S complex and the V complex were simulated. The differential cross-section in the normal Raman spectrum of pyridine is on the order of 10^{-31} $cm^2 sr^{-1}$. The dominant Raman peaks at 978 and 1022 cm^{-1} are both assigned to ring modes. Upon binding to silver, several differences in the Raman spectrum of pyridine can be observed. The overall intensity of Raman scattering is enhanced by a factor of 4 for the V complex and by a factor of 8 for the S complex. The higher enhancement for the S complex is expected since it involves a stronger Py–Ag interaction. The observed chemical enhancement is due to changes in the electronic properties, in particular the increased polarizability due to the charge transfer from pyridine to silver upon coordination. This also causes wavenumber shifts, in particular for those normal modes which involve vibrational motions of the N atom along the N–Ag bond. Mode-specific differences are observed not only for peak positions, but also for the relative Raman intensities. In addition to the chemical effect, the other two contributions—the charge transfer and the electromagnetic enhancement—were also calculated. The charge transfer (CT) resonance enhancement was estimated for the CT excitation (471 nm) with the largest oscillator strength. The Raman scattering intensities are about 10^4 times larger than the normal Raman scattering intensities of pyridine; in other words, the CT contribution adds an additional 3 orders of magnitude on top of the chemical enhancement. The electromagnetic enhancement for the S and V complex was calculated at incident wavelengths of 365 and 363 nm, respectively. It is important to keep in mind that due to the limited size of the cluster with only 20 silver atoms, one cannot speak of a true collective oscillation, but should rather consider it to be a microscopic model of the plasmon excitation occurring in a silver NP.

3.5.2. Potential-Dependent SERS on Individual Hot Spots

The discrimination between CT contributions and SERS intensity variations due to molecular reorientations induced by the external potential is possible by the use of several laser excitation lines across the visible region. The effect of molecular reorientations on the SERS spectra should be independent of the excitation energy. In contrast, the CT contribution should be dependent on the excitation energy since it depends on the match between the incoming photon energy and the CT transition energy. Electrochemical SERS experiments are typically performed on roughened electrodes ("bulk") with a high inhomogeneity in terms of plasmonic enhancement because hot spots with extreme enhancements as well as areas with only modest enhancement are present. Quantifying the contributions of the different mechanisms is therefore difficult since it requires knowledge of various parameters that are practically unattainable: hot spot distribution, molecular orientation, and the coverage on the highly heterogeneous surface. The complexity of the situation can be reduced by collecting SERS signals from individual hot spots under electrochemical conditions.[55] Figure 19 shows SEM images of aggregated silver nanoparticles at low (a) and high resolution (b) before potential sweeps are applied. 4-Mercaptopyridine (4-MPy) was chosen as a probe molecule because of its strong binding to the silver surface through the thiol group and its C_{2v} symmetry, which facilitates the identification of molecular reorientations. Figure 19c shows a SERS false-color map exhibiting a single hot spot. Wavelength- and potential-dependent SERS spectra of 4-MPy molecules were recorded from individual hot spots within the silver island structures. The potential sweep drives the system

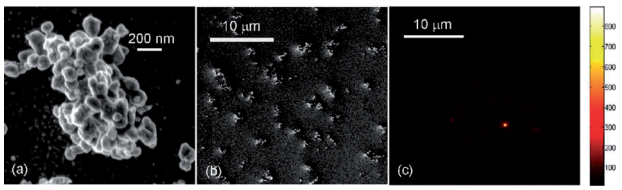

Figure 19. a,b) SEM images of silver islands and c) a false-color Raman image showing a single hot spot. From Ref. [55].

molecule@metal in and out of the CT resonance by tuning the position of the Fermi level of the metal, while the different laser excitation wavelengths make it possible to differentiate CT contributions (wavelength-dependent) from molecular reorientations (not wavelength-dependent). Reference measurements were performed with R6G as a second probe molecule. These reference experiments were conducted separately; that is, R6G and 4-MPy were never co-adsorbed on the same surface during the same experiment. Since the absolute Raman cross-section for R6G is known, the absolute Raman cross-section of 4-MPy (and any other molecule) can be determined, without knowing the (usually experimentally inaccessible) absolute magnitude of the EM enhancement. The authors concluded that the Raman scattering cross-section of the strongest band of 4-MPy should be on the order of 10^{-26} cm^2, which is at least 3 orders of magnitude larger than that of similar small organic molecules in the absence of electronic resonance, e.g., benzene. Since the lowest electronic excitation of 4-MPy is at 324 nm, this extra enhancement by 3 orders of magnitude is assigned to the chemical mechanism because 4-MPy is excited far from electronic resonance in these SERS experiments. Overall, this approach is especially useful for molecule@metal systems with CT excitations in the visible region, which naturally overlap with the plasmon resonance of the metal.

4. Plasmonic Nanostructures for SERS

The ideal plasmonic nanostructure used in SERS—often called the SERS substrate—is chemically stable, easy to prepare in a reproducible manner, and exhibits a spatially uniform, high EF. Numerous approaches for the synthesis of various SERS substrates have been summarized in a series of book chapters and review articles.[33,56–66] In this section, only few selected plasmonic nanostructures will be highlighted. Silver and gold are by far the most frequently used metals in SERS. Section 4.1 covers metal NPs as substrates used in colloidal SERS, while Section 4.2 covers arrays and films for use as "solid" SERS substrates. Strategies of surface functionalization for enriching and trapping molecules will be discussed in Section 5.3.

4.1. Metal Nanoparticles as SERS Substrates

4.1.1. Metal Nanoparticles with a Very Thin Glass Shell (SHINERS)

Figure 20 depicts different modalities of plasmon-assisted Raman scattering. In Figure 20a bare Au nanospheres are deposited as a film on a solid support and the molecules to be probed—indicated as blue dots—are in direct contact with the metal surface. This contact mode also applies to transition-metal-coated NPs (Figure 20b), which extend the application

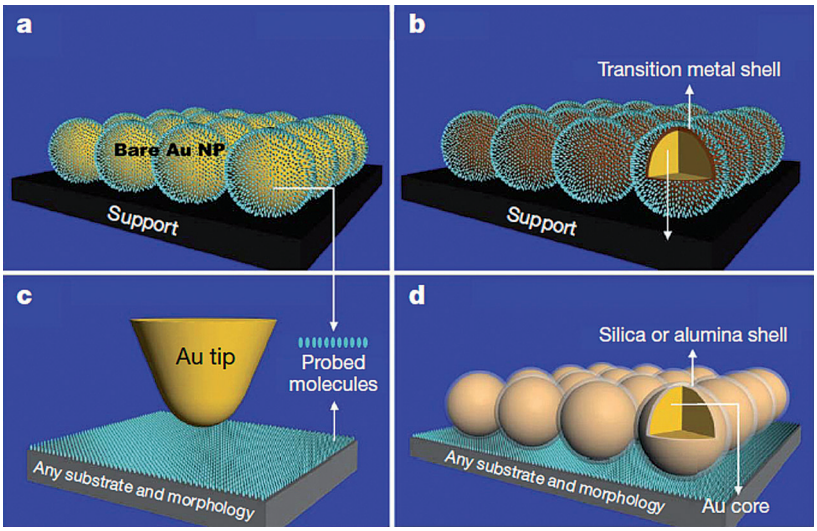

Figure 20. Different modalities of SERS. See text for details. From Ref. [67].

of SERS to other wavelength regions and transition-metal-catalyzed reactions. In contrast, tip-enhanced Raman scattering (TERS) operates in a noncontact mode (Figure 20c): the Au tip, acting as the Raman signal amplifier, and the probed molecules on the surface are separated from each other. With this powerful approach of chemical imaging at the nanometer scale any substrate can be probed without additional constraints on material composition and surface topography. Shell-isolated nanoparticle-enhanced Raman spectroscopy (SHINERS)[67,68] also operates in the noncontact mode by using Au nanospheres protected by a 2 nm ultrathin glass shell (Figure 20d), which isolates the gold surface from the probed molecules and therefore prevents a potentially disturbing interaction. On the other hand, the very short metal–molecule separation (SERS distance dependence; see Section 3.4) of 2 nm still leads to a significant NP-enhanced Raman signal compared with the contact mode. Since the entire surface is covered by a "smart dust" of Au/SiO_2 particles, a very large number of "tips" are simultaneously probing the underlying molecules. The dense packing of the Au/SiO_2 particles present as a monolayer on a smooth Au surface was demonstrated by scanning electron microscopy (SEM). The thickness of the glass shell can be controlled, as demonstrated by HR-TEM. In addition to encapsulation by silica, also a very thin aluminum oxide shell can be prepared.

Overall, this methodology is very flexible; it can be applied to virtually any surface by adapting to the surface

topography as a "smart film" and therefore the simultaneous interrogation of the entire surface is possible by "spatial multiplexing". Equally important, the noncontact mode prevents the direct metal–molecule interaction—the source of many irregularities observed in conventional SERS in the contact mode (Figure 20a). This leads to more "reasonable" spectra in the sense that the NPs provide only the desired signal enhancement, but at the same time do not perturb the electronic, vibrational, and/or conformational properties of the molecule due to adsorption onto the metal surface.

4.1.2. *Anisotropic Etching of Silver Nanoparticles*

The ability to distinguish between various crystallographic faces and growth directions is of central importance for controlling the shape of single-crystalline metal NPs.[69,70] The position of the plasmon peak and the scattering properties depend on the size, shape, and the proximity of the nanoparticles. Single silver and gold nanospheres with plasmon peaks in the blue and green regions, respectively, exhibit only moderate EFs. In contrast to highly symmetric and isotropic colloidal particles, plasmonic nanostructures with sharp corners and edges exhibit significantly increased field enhancements. The controlled synthesis of such anisotropic particles in high yield and purity is therefore a promising approach to highly active plasmonic nanostructures exhibiting single-particle sensitivity.

In a similar way to the control over nanoparticle growth with respect to size and shape,[69,70] also the opposite process—selective etching—can be exploited for the controlled generation of shaped nanostructures. Anisotropic etching of octahedral silver particles[31] was developed by using a 9:1 mixture of NH_4OH and 30% H_2O_2 for selectively etching (100) planes of the nanocrystals. Figure 21 schematically shows the conversion of a Ag octahedron (left) to a starlike octapod (right) through increased anisotropic etching of the (111) faces. Also quantitative data from kinetic measurements were obtained, which demonstrate the selectivity of the 9:1 NH_4OH/H_2O_2 mixture for the (100) faces. The average thickness of the NPs in both directions (d100 and d111) was determined from the corresponding SEM images and evaluated as a function of the etchant concentration. While d100 decays rapidly with $c(H_2O_2)$, d111 varies only slowly. The difference in the slopes, as determined from the corresponding least square fits, is larger than 20-fold.

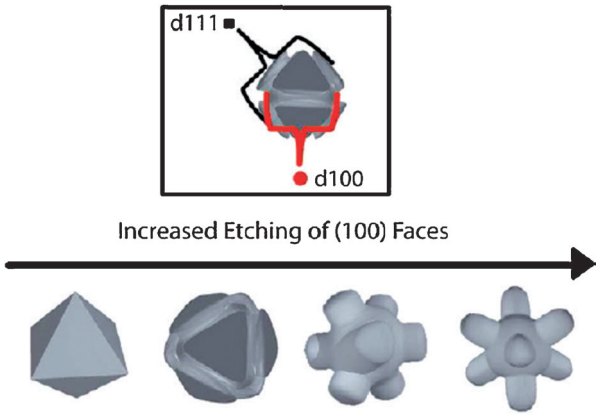

Figure 21. Anisotropic etching of octahedral Ag nanoparticles. From Ref. [31].

The optical properties of each of the four states during etching, starting from octahedral particles, were characterized at the single-particle level by dark-field microscopy (Figure 22). All particle morphologies exhibit different colors—ranging from yellow-green for the octahedral to red for the octapod structures—due to their characteristic and distinct elastic scattering spectra. In addition to these single-particle LSPR experiments, it was demonstrated that all particles exhibit also single-particle SERS sensitivity in measurements using a nonresonant probe molecule during 1 s integration time.

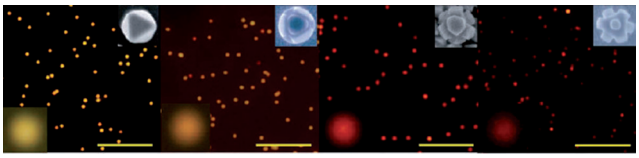

Figure 22. Single-particle dark-field images of NPs obtained by anisotropic etching. From Ref. [31].

Overall, these anistropic silver NPs exhibit interesting plasmonic properties, with LSP resonances covering the visible to near-infrared regions and large scattering intensities due to their intrinsic edges and corners.

4.1.3. *Dimers of Silver Nanospheres*

Dimers of noble metal nanospheres are highly efficient plasmonic substrates for SERS since a hot spot occurs in the gap between the two spheres (see Section 3.1). While colloidal clusters or aggregates are routinely prepared in the wet-chemistry laboratory by salt addition in a rather uncontrolled way, their controlled synthesis is much more challenging. An elegant and straightforward approach to dimers of Ag nanospheres starts from Ag nanocubes (Figure 23 left).[71] The addition of a small amount of an aqueous solution of $Fe(NO_3)_3$ to a suspension of Ag nanocubes yields dimers of Ag nanospheres through etching and dimerization. The iron salt $Fe(NO_3)_3$ has two important functions in this process. First, it is a powerful wet etchant to dissolve Ag, that is, oxidizing it from Ag(s) to Ag^+. Second, it is an ionic species and electrolyte which decreases the stability of the colloidal system. Thus, it serves as an etching agent for converting Ag cubes to Ag spheres and also triggers the subsequent dimerization of the Ag spheres. Also the presence of polyvinylpyrrolidinone (PVP) and ethanol is required. Without PVP, the etching process did not proceed. In addition, no dimers were observed when the reaction was performed in water, most likely because of the rapid formation of a $Fe(OH)_3$ coating, which prevents the formation of dimers. In a second step (Figure 23 right), the dimers of Ag nanospheres are coated by silica to form a continuous glass shell around the dimers. This is required for confirming that the

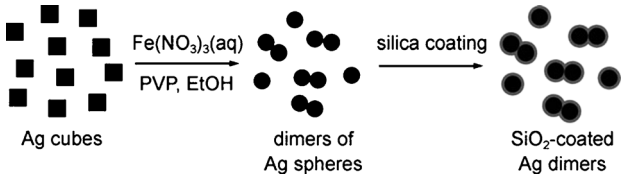

Figure 23. Synthesis of dimers of Ag nanospheres from Ag nanocubes. From Ref. [71].

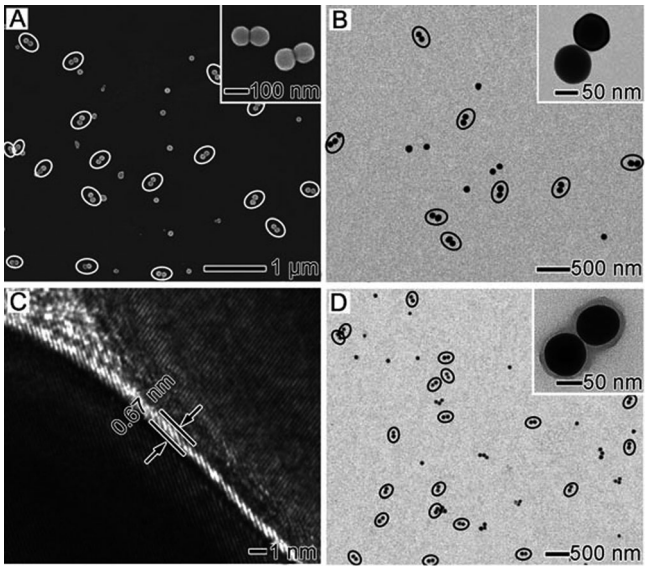

Figure 24. SEM and TEM images of Ag nanosphere dimers obtained from Ag nanocubes, illustrating the very small gap between the cubes. From Ref. [71].

dimers have indeed formed in suspension, rather than on the substrate during the preparation of the sample for analysis by electron microscopy.

The electron microscopy images in Figure 24 show the resulting dimers of Ag nanospheres, obtained from Ag cubes with an edge length of roughly 100 nm. The large number of dimers, highlighted by white and black ellipses, confirms the good production yield, which was estimated to be around 66 % based on $N = 150$ Ag nanoparticles. A very small gap of only 0.67 nm or 670 pm—equivalent to the length of several C–C bonds—is evident in the HR-TEM image in Figure 24 C. The TEM image of a sample obtained after silica coating also contains a large number of dimers, which convincingly demonstrates that the dimers have indeed formed in suspension rather than on the substrate during the deposition of the sample on the grids for SEM or TEM characterization. Polarization-dependent SERS measurements of Ag nanosphere dimers with 4-methylbenzenethiol (4-MBT) as a probe molecule exhibit the expected orientation-dependent enhancement upon laser excitation parallel and perpendicular to the dimer axis (cf. Section 3.3.1).

Also clusters larger than dimers can be prepared, using an elegant stoichiometry-controlled heteroassembly of NPs.[44] Overall, control over the size and monodispersity of quasi-spherical Ag NPs[72] is desired for systematically investigating the size-dependent optical properties of the corresponding dimers and assemblies.

4.2. Nanostructured Arrays and Films as SERS Substrates

4.2.1. Nanostructured 2D SERS Substrates Fabricated by Nanosphere Lithography

Nanosphere lithography (NSL) is an elegant, very powerful and highly flexible nanofabrication approach, which provides outstanding control over NP size, shape, and interparticle spacing. The following description of NSL refers to the simplest configuration, a single-layer periodic particle array.[73–76] A monolayer of hexagonally close-packed nanospheres is self-assembled onto the surface of a substrate (Figure 25 top). Upon solvent evaporation, the nanospheres are drawn together by capillary forces. The resulting self-assembled 2D monolayer of hexagonally packed nanospheres can then serve as a colloidal crystal mask (side view: Figure 25 top right; top view: Figure 26) for the subsequent deposition of metal onto this mask, either by physical vapor or electrochemical deposition (Figure 25 middle).[76] The C_3-symmetric interstices (Figure 26) allow the deposited metal to reach the substrate, while all other regions on the substrates are blocked by the colloidal crystal mask. Three types of nanostructured SERS substrates can be prepared (Figure 25 bottom), depending on the thickness of the deposited metal layer. Physical vapor deposition on the

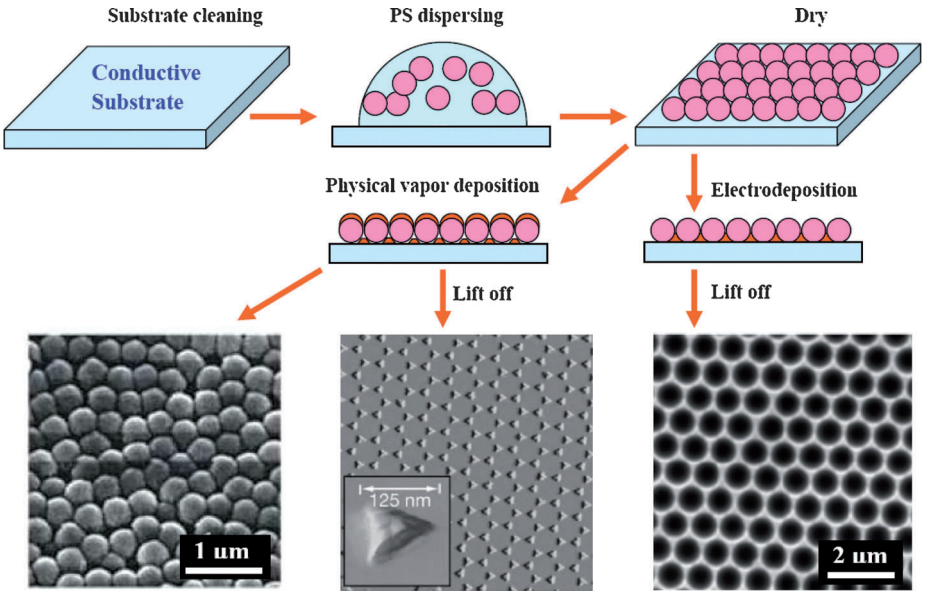

Figure 25. Nanosphere lithography for the fabrication of nanostructured SERS substrates. From Ref. [76].

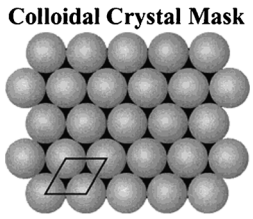

Figure 26. Colloidal crystal mask used as a template. From Ref. [74].

crystal mask yields a film-over-nanospheres (FON) surface (Figure 25 bottom left). Removal of the nanospheres by sonicating the sample leads to triangular-shaped Ag nanoparticles with P_{6mm} symmetry (Figure 25 bottom middle and Figure 26). The sharp tips lead to high field enhancements upon resonant plasmon excitation. Electrochemical deposition with subsequent removal of the spheres yields a thin structured film comprising a regular hexagonal array of uniform segment sphere voids (SSV, Figure 25 bottom right).

4.2.2. *Aluminum Oxide Overlayers on a Silver Film-over-Nanosphere Substrate*

The stability of a plasmonic SERS substrate determines the breadth of its application. Key parameters are the stability against chemical perturbation, in particular oxidation, and the tolerance of different physical conditions such as high temperatures. In addition to stabilization, surface functionalization is a second important aspect since selectivity for analytical applications can be introduced in this way. Affinity coatings with analyte-specific molecules selectively capture the analyte from a sample solution onto the surface for SERS detection. Thiol-containing molecules are often used since they form self-assembled monolayers (SAMs) on the metal surface. However, photoxidation and thermal desorption of the thiols may lead to defects of the coating. In contrast, aluminum oxide is a coating material which fulfills several of the requirements described above: extreme stability against oxidation and high temperatures as well as strong interaction with polar analytes such as carboxylic acids in a predictive manner. Further, atomic layer deposition (ALD) of aluminum oxide provides precise control over thickness and surface coverage. The ability to generate very thin (ca. 1 nm) overlayers of aluminum oxide on top of the actual solid SERS substrate[77] is important since the detection capabilities of the entire system are determined by the distance between the analyte and the metal surface (cf. SERS distance dependence, Section 3.4); the same considerations were also relevant for the SHINERS approach (Section 4.1.1). Figure 27 shows a SEM image of an alumina-modified AgFON substrate.

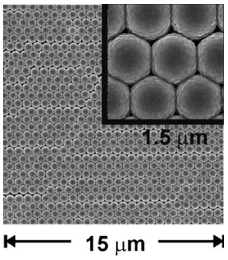

Figure 27. SEM image of an Al_2O_3-modified Ag FON. From Ref. [77].

4.2.3. *Nanosphere Arrays with Controlled Gaps Smaller than 10 nm*

Coating gold nanospheres with a roughly 2.2 nm thin layer of cetyltrimethylammoniumbromide (CTAB) and depositing them on indium-doped tin oxide (ITO) glass under ambient conditions leads to the formation of a hexagonally close-packed monolayer of NP arrays (Figure 28 A).[78] The average interparticle spacing determined from SEM images is 8 nm (Figure 28 B). Figure 28 C shows a SEM image of a monolayer of isolated gold nanospheres on ITO glass. The plasmonic properties are displayed in Figure 28 D. The array exhibits a plasmon peak in the red to near-infrared region; in contrast, the constituting single Au nanospheres have a plasmon peak around 500 nm.

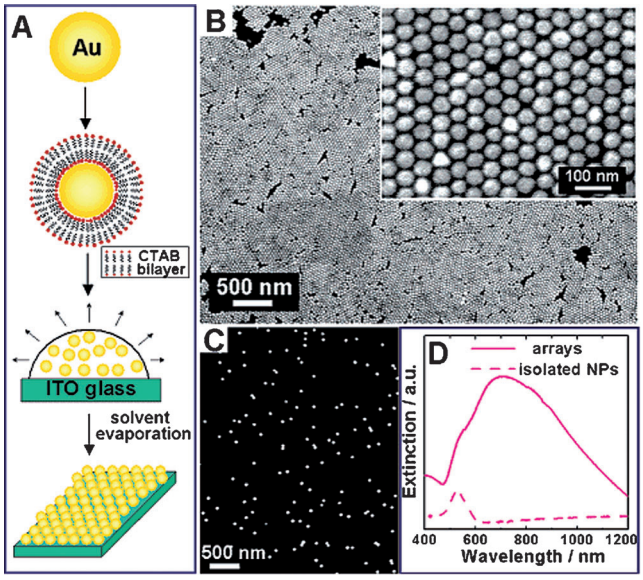

Figure 28. Gold nanosphere arrays with gaps of less than 10 nm. From Ref. [78].

4.2.4. *Exponentially Grown Layer-by-Layer Films*

The detection of analytes at very low concentrations by SERS using solid plasmonic substrates requires that regions with very high field enhancements (hot spots) are accessible for the analyte. Ideally, the molecules also have a high retention time and yield SERS signals over a relatively long period of time. Nanoparticles inside a polymeric matrix provide both access to hot spots and analyte retention.

Thin films prepared by exponential layer-by-layer deposition (e-LBL) are a promising example of such materials since they can be infiltrated by inorganic/metal NPs and owing to the composition of their layers it is possible to analyze molecular systems in solution. Figure 29 shows electron microscopic images of e-LBL films infiltrated with Ag NPs.[79] Figure 29 A and B are top-view SEM images of the e-LBL film after 24 h of immersion shown at different magnifications. Figure 29 C and D are cross-sectional TEM

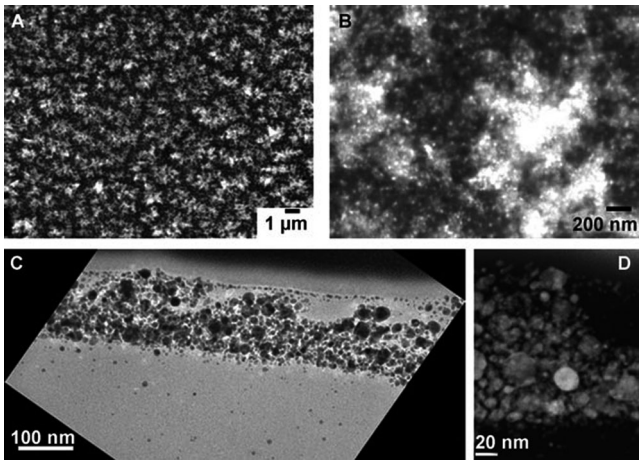

Figure 29. Thin films prepared by exponential layer-by-layer deposition. From Ref. [79].

and STEM images of the film, respectively, after focused ion beam (FIB) preparation.

These thin films have been employed for the detection of dioxins as "unsual" or "difficult" analytes since they do not exhibit a surface-seeking group. This approach for SERS detection is therefore based on the molecular trapping properties of the e-LBL film, rather than the commonly employed approach of adsorbing the analyte onto the metal surface.

The e-LBL approach does not provide control over the locations of the hot spots. The next example presents a rationally designed metal nanostructure with hot spots at well-defined positions.

4.2.5. Silver Nanowire Bundles

Silver nanowires offer a simple yet powerful strategy for obtaining hot spots in the junction between tips of neighboring Ag nanowires. The nanowires can be grown in a highly ordered porous aluminum oxide (PAO) template by electrodeposition, followed by the controlled dissolution of the alumina matrix. Figure 30 shows SEM images of Ag-PAO templates obtained by partial dissolution of the alumina matrix.[80]

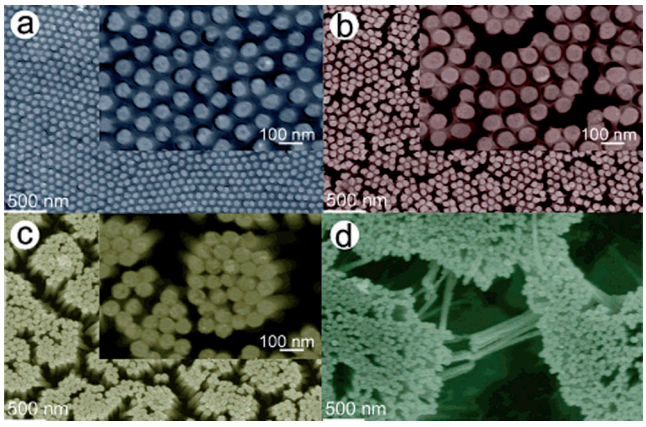

Figure 30. SEM images of silver nanowires. From Ref. [80].

5. Chemical Applications

SERS combines the molecular specificity of vibrational Raman spectroscopy with high sensitivity due to plasmon-assisted scattering. In SERS, Raman scattering from molecules on or near nanostructures that support localized surface-plasmon resonances (LSPRs) is increased by several orders of magnitude (Sections 2–4). This section covers a broad and diverse range of chemical applications of SERS and is therefore the centerpiece of the entire Review. It starts with the spectroelectrochemical investigation of molecules adsorbed on roughened metal films/electrodes, which is a "traditional" application of SERS.[1,2]

5.1. Spectroelectrochemistry and Catalysis

The identification of intermediates and the establishment of reaction mechanisms is a central topic in chemistry, including organic, inorganic, physical, and theoretical chemistry as well as biochemistry and molecular biophysics. This subsection focuses on the application of SERS to catalysis[81] and electrochemistry.[76,82,83] The size of the investigated molecules ranges from diatomics[84] and aromatic compounds[85,86] to proteins attached to model membranes.[87–90]

5.1.1. Monitoring Oxygen Electroreduction on Bismuth-Modified Au Surfaces

The electroreduction of molecular oxygen has long been at the focus of electrochemical research since it is an important process in corrosion and fuel cells. Two pathways, which are most relevant to fuel cells, have been identified in acid media: 1) a direct four-electron pathway from oxygen to water without intermediates and 2) a two-electron pathway containing a peroxide intermediate. The pathway depends on electrode composition: oxygen electroreduction proceeds by pathway 1 on Pt and Ag surfaces, while pathway 2 dominates on Au surfaces. There is an intensive search for materials that could replace Pt since it is expensive and not very efficient for the process. This is a result of the high dissociation energy of molecular oxygen (494 $kJ\,mol^{-1}$) leading to slow kinetics and large overpotentials for the four-electron pathway. However, this search is complicated by our limited understanding of the detailed mechanism of O_2 electroreduction on Pt or any other relevant material in the acidic electrochemical environment. Investigations on the mechanism of oxygen electroreduction have relied extensively on voltammetric methods, which cannot definitely determine the mechanism—pathway 1 versus pathway 2—or identify intermediates—in particular superoxide—with molecular specificity. SERS was therefore employed in order to examine intermediates associated with the electroreduction of molecular oxygen on bismuth-modified polycrystalline Au surfaces, which serve as a model system.[84] In contrast, investigations by surface infrared

spectroscopy are limited by interferences from solution above the electrode surface and its low sensitivity in the low-wavenumber region where vibrational bands due to metal–oxide and metal–hydroxide modes typically occur.

Figure 31 left shows the SERS spectra in the range 600–1200 cm^{-1} obtained from polycrystalline Au in solution, Au(poly), containing 0.5 mM Bi^{3+} and 0.1M $HClO_4$ saturated

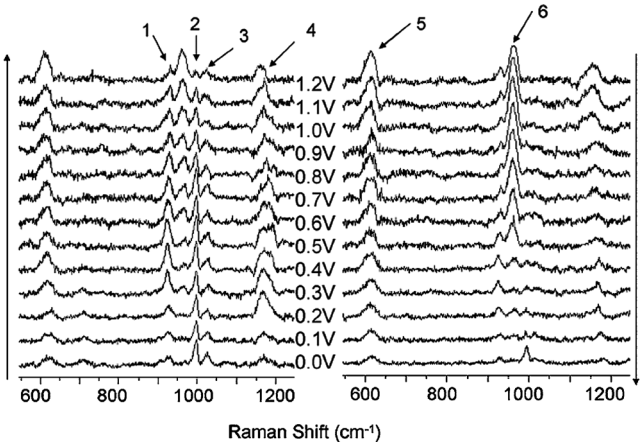

Figure 31. Electrochemical SERS investigation of the electroreduction of molecular oxygen on bismuth-modified polycrystalline Au surfaces. From Ref. [84].

with O_2. The series on the right reflects the anodic sweep from 0.0 to 1.2 V, the series on the right the cathodic sweep. Overall, six vibrational Raman bands can be identified. Peaks 1 to 4 were also observed in SERS control experiments obtained from Au(poly) in solution containing 0.1M $HClO_4$ saturated with O_2, in other words, a control without Bi^{3+}. In particular the presence of peak 4 in Figure 31 suggests that superoxide is one of the intermediates in the O_2 electroreduction on both Bi-modified and bare Au(poly) surfaces (control experiments, not shown). Overall, several signals attributable to O_2, HO_2, Bi-OH, and Bi_2O_2 are detected in the SERS measurements, suggesting that these species are intermediates during the O_2 electroreduction. Superoxide seems to play an important role since it is observed on both bare Au and Bi-modified Au surfaces. Additionally, the observation of superoxide suggests that the four-electron reduction of O_2 on the bismuth-modified surface occurs by the stepwise mechanism.

DFT calculations on O_2 adsorption on bare and bismuth-modified surfaces were performed in order to obtain insight into the electronic structure and energetics. The adsorption energy for molecular oxygen increases from −0.928 eV to −2.322 eV, indicating that the Bi adlayer stabilizes O_2 adsorption on the Au surface. The O−O bond length increases from 126 pm on the Au surface to 136 pm on the Bi/Au surface, which is close to the experimentally found bond length for superoxide O_2^-. In addition, the calculated Mulliken charges on Bi and O atoms before and after O_2 adsorption indicate a transfer of electron density to the O_2 molecule, and concomitant partial oxidation of the Bi adatom. These combined DFT and SERS findings provide valuable mechanistic information; they also strongly suggest that renewed attention to the first step, the conversion of O_2 to HO_2, must be paid.

5.1.2. SERS Monitoring of Benzyl Chloride Reduction at a Silver Electrode

The cleavage of carbon–halogen bonds by electrochemical reduction at inert electrodes is of importance in areas such as electroorganic synthesis, environmental applications, and mechanistic studies on electron transfer. In this context, silver cathodes exhibit a surprisingly large electrocatalytic activity. Again, as in the first example (Section 5.1.1), voltammetry alone cannot characterize transient surface intermediates in situ with the necessary chemical specificity at the molecular level. Also in this case, the electrochemical reduction of benzyl chloride ($PhCH_2Cl$) at a Ag electrode in acetonitrile, a combined SERS and DFT study provided evidence for the corresponding reaction intermediates.[85] The cyclic voltammogramms (CVs) exhibit a single irreversible reduction peak: for the potential sweep of 0.5 $V s^{-1}$, a peak potential of $E_p = -1.82$ V vs. standard calomel electrode (SCE) is observed. The potential-dependent SERS spectra were recorded in the voltammetric range from −0.6 to −2.2 V. At potentials more positive than −1.2 V, the features in the SERS spectra resemble those of free $PhCH_2Cl$ with few significant changes indicating a weak interaction between $PhCH_2Cl$ and the Ag surface. Two drastic spectral changes are observed at −1.2 and −1.6 V. At −1.2 V an intense and unusually strong peak at 800 cm^{-1} appears, which reaches its maximum at −1.4 V. Also, a broad peak at 350 cm^{-1} is observed; it is assigned to Ag–C stretching bands and therefore indicates that at least one reaction intermediate is strongly bound to the surface by a C−Ag bond. At −1.6 V and beyond, a peak at 1000 cm^{-1} occurs, reaching its maximum at −1.8 V.

DFT-simulated spectra can be compared directly with experimental data. The aim is to unambiguously assign the experimentally observed Raman bands to distinct chemical species, in this case surface intermediates. Figure 32 displays the DFT-simulated spectra of the free/unbound benzyl radical (a) and benzyl anion (b), respectively, and their corresponding adducts with a Ag_4 cluster (c,d). A 1:5 superposition (f) of the predicted spectra in (d) and (e) is used for comparison with the experimental SERS spectrum (c) at −1.4 V vs. SCE. All together, the data indicate that both neutral and anionic benzyl–silver adducts were formed, with the anionic species dominating over the main voltammetric range.

This combined SERS/DFT study provides mechanistic insights into the catalytic properties of Ag cathodes for electroreduction: benzyl chloride is weakly adsorbed on the silver surface, first reduced to a bound benzyl radical and then further reduced to the bound benzyl anion. This pathway differs completely from that of the outer-sphere concerted electron reduction at inert electrodes, and alters the thermodynamics and kinetics of the first reduction step. A particular strength of SERS for retrieving in situ mechanistic information is therefore in situations with a strong interaction between reactants and the catalytic metal surface.

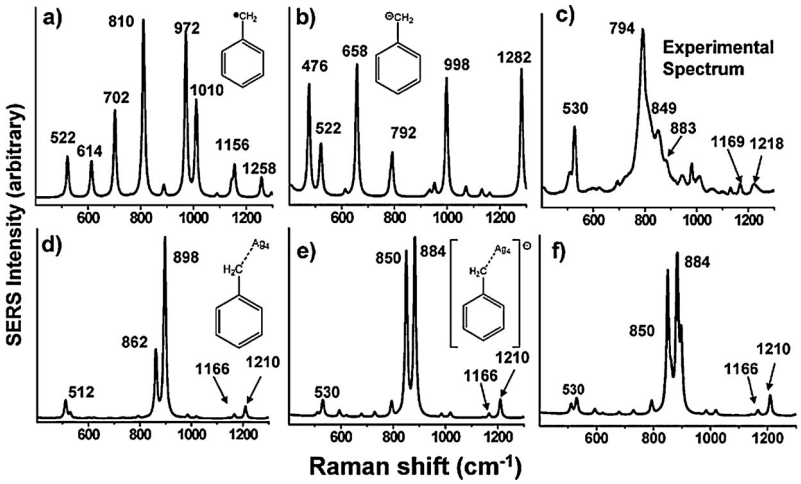

Figure 32. DFT-calculated Raman spectra of different benzyl species together with the experimental SERS spectrum (c). From Ref. [85].

(starting material) decreases and vibrational bands from an azo derivative first increase and then finally disappear. Negative control experiments with a mixture of bare Au and Pt nanospheres did not exhibit the same combined catalytic/SERS activity. Decomposition of the spectrally overlapping contributions from the nitro, azo, and aniline compounds with nonnegative matrix factorization made it possible to quantify the contributions of all three species in each SERS spectrum. In principle, also unknown species could be identified using this combined vibrational/multivariate technique since only the number of chemical components, but no a priori knowledge on their spectral signatures, is required. This approach may become useful for mechanistic investigations in catalytic reactions. A

5.1.3. Monitoring of Platinum-Catalyzed Reactions in Colloidal Suspension

SERS monitoring of catalytic reactions in colloidal suspensions requires NPs that integrate two normally distinct functionalities—plasmonic and catalytic activity—into a single bifunctional entity. The central challenge is therefore to rationally design and synthesize hybrid metal nanostructures that exhibit both high plasmonic/SERS activity and a large surface area of the catalytically active metal. The raspberry-shaped Au/Pt/Au core/shell NPs depicted in Figure 33 fulfill these criteria for platinum-catalyzed reactions;[86] a HR-TEM image of a single raspberry together with a computer-generated model of the core/shell structure with high Pt surface area for catalysis is shown. Plasmonic coupling between the 80 nm Au core (already SERS-active when isolated) and the small Au protuberances (not sufficiently SERS-active when isolated) "lends" plasmonic activity to the entire superstructure, rendering it bifunctional.

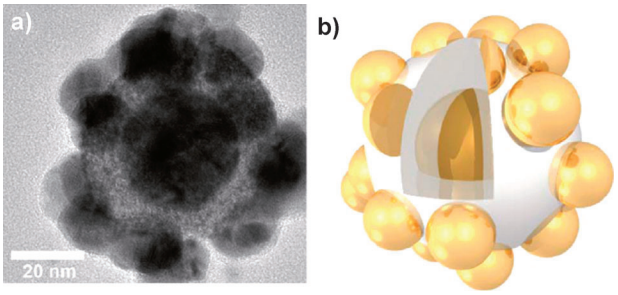

Figure 33. a) HR-TEM image of a Au/Pt/Au nanoraspberry and b) a computer-generated 3D model. From Ref. [86].

In a proof-of-concept study, the hydride reduction of an aromatic nitro compound to the corresponding aniline derivative was monitored by SERS (Figure 34). With an increasing amount of $NaBH_4$ (from bottom to top), the intensity of the characteristic peaks of the nitro compound

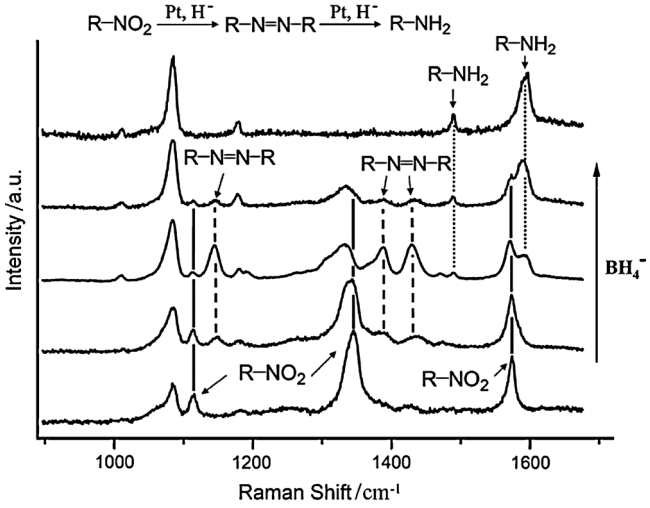

Figure 34. SERS spectra recorded for the Pt-catalyzed hydride reduction of 4-nitrothiophenol to the corresponding aniline derivative using Au/Pt/Au nanoraspberries. From Ref. [86].

current limitation of the Au/Pt/Au nanoraspberries is their restriction to reactions of molecules with a surface-seeking group. Strategies for trapping molecules without such groups near the metal surface (see Section 5.3.2) may overcome this limitation and expand the applicability to a much broader range of catalytic transformations.

5.1.4. Electron Transfer between Proteins and Model Membranes at Electrodes

Inter- and intramolecular electron-transfer (ET) reactions can be controlled or limited by protein dynamics. Proteins immobilized on electrodes coated with biocompatible films can be used to study these fundamental phenomena under controlled conditions, although they unavoidably deviate from the true physiological conditions. Simultaneous and direct real-time monitoring of structure, ET kinetics, and configurational fluctuations of cytochrome C (Cyt) electro-

statically adsorbed to electrodes coated with a SAM was achieved with two-color time-resolved SERRS spectroscopy.[87] The application of a potential jump triggers the reorientation of the protein relative to the electrode surface in addition to the net ET. The time-resolved two-color (413 and 514.5 nm) SERRS experiments probing the heme chromophore were used to extract the time constants for both protein reorientation and ET as a function of SAM chain length. The vibrational spectroscopic basis for this wealth of biophysical information accessible from SERRS experiments is related to the selectivity of resonance Raman (RR) scattering towards normal mode symmetry and the selectivity of SERS towards the orientation of the heme chromophore with respect to the surface. The RR intensity ratio $\nu_{10}(B_{1g})/\nu_4(A_{1g})$ is used as a marker for protein orientation, specifically the degree of perpendicular orientation. Figure 35 A depicts

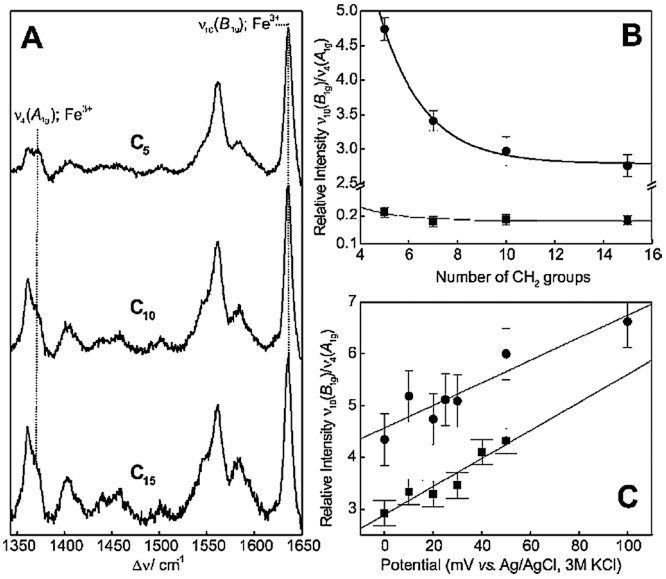

Figure 35. SERRS spectra of cytochrome C electrostatically adsorbed to electrodes coated by SAMs with different chain lengths. The intensity ratio $\nu_{10}(B_{1g})/\nu_4(A_{1g})$ is a marker for protein orientation. From Ref. [87].

the SERRS spectra of Cyt on electrodes coated with C_5, C_{10}, and C_{15} SAMs. With increasing chain length (Figure 35 B), the intensity ratio $\nu_{10}(B_{1g})/\nu_4(A_{1g})$ rapidly decreases for the oxidized form (ferric/Fe^{3+}, circles), but only slowly for the reduced form (ferrous/Fe^{2+}, squares). For a given SAM, the intensity ratio $\nu_{10}(B_{1g})/\nu_4(A_{1g})$ exhibits a positive correlation with the applied potential (Figure 35 C). Overall, the electric field at the Cyt/SAM interface seems to control the orientation of Cyt.

Kinetic information on the orientation/reorientation of the heme unit in Cyt can be obtained from time-resolved (TR) pump(potential jump)/probe (SERRS) experiments. After the application of a potential pump to an equilibrated sample, the orientation of the adsorbed ferric Cyt evolves towards the equilibrium value at the final potential. The experimentally determined rate constants for reorientation strongly depend on the chain length of the SAM. This observation is qualitatively consistent with a simple electrostatic model in which the charge density at the SAM terminus (COO^-) determines the activation barrier for reorientation of the complex above the threshold of thermal energy (kT). In addition to the net ET, the application of a potential jump triggers the reorientation of the protein relative to the surface: the reorientation is fast for thick SAMs and low electric fields, while it slows down dramatically and becomed rate-limiting for thin SAMs and high electric fields. These results imply that local electric fields determine both mean orientation and the mobility of Cyt in electrostatic complexes. Control of the overall ET rates by electric fields through modulation of protein dynamics may therefore be a widespread phenomenon in bioelectrochemistry.

5.2. Single-Molecule Detection

Two pioneering investigations reported on single-molecule SERS (SM-SERS) in 1997.[3,4,91–94] In the case of the dye Rhodamine 6G (R6G) on citrate-reduced Ag NPs immobilized on glass in an ambient environment, strong SERS intensity fluctuations on the second timescale were observed, which were subsequently attributed to the surface diffusion of R6G molecules into and out of the hot spot. Independently, SM-SERS for crystal violet (CV) was observed using citrate-reduced Ag NP aggregates in suspension. In these and subsequent SM-SERS studies, different arguments were employed for claiming single-molecule behavior. Generally, intensity fluctuations in combination with statistical analysis were thought to corroborate the claim of SM-SERS. However, these approaches are accompanied by a series of complications.[95] First, low dye concentrations—suggesting that there is on average one dye molecule per colloidal particle—do not necessarily provide satisfactory proof. Second, SERS spectra exhibit strong intensity fluctuations—including both intensity and spectral changes as well as alternating on/off periods called blinking—which were usually considered to be a characteristic behavior of SM emission. However, these fluctuations are even observed for high dye concentrations as well as under other circumstances. A significant advance in support of the claim of SM-SERS was the introduction of the bianalyte approach (BiASERS),[95] in which two analytes (e.g., two dyes) with spectrally distinct SERS signatures compete with each other for surface adsorption, or, introduced soon after, two different isotopologues of the same dye.[96]

5.2.1. Wavenumber-Domain-Based Approaches to Single-Molecule SERS/SERRS

5.2.1.1. The Bianalyte Approach: Spectral Discrimination in the Wavenumber Domain

Using two different analytes with a surface-seeking group, but with different SERS spectra, is an elegant way of demonstrating the presence of single-molecule behavior in SERS (bianalyte SERS or BiASERS).[95] Figure 36 top shows SERS spectra of rhodamine 6G (R6G) (A), a benzotriazole dye (BTZ) (C), and a combination of both (B), extracted from different positions of a SERS microspectroscopic

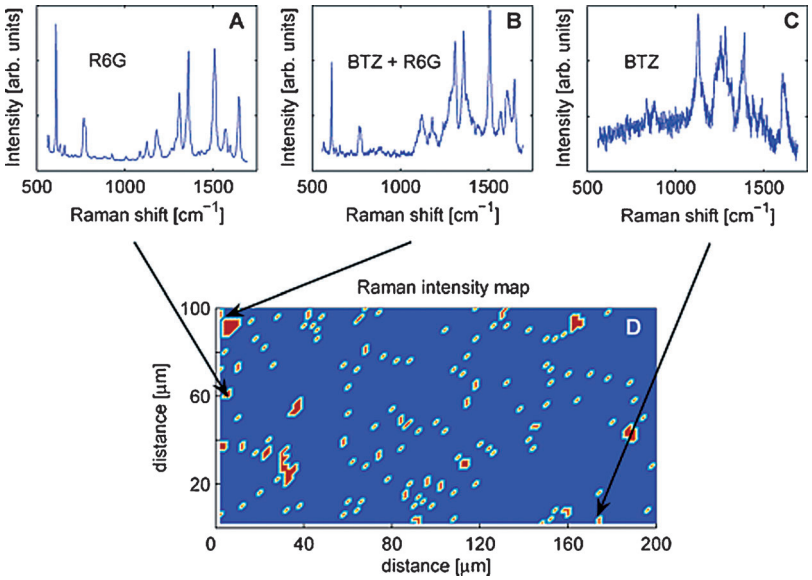

Figure 36. Bianalyte SERS (BiASERS) for the wavenumber-domain-based demonstration of single-molecule SERS. From Ref. [95].

experiment (bottom). When there is just a single molecule, the probability of finding either R6G or BTZ is 1:1. In the case of two molecules, the probability distribution of having either $2\times$R6G or $1\times$R6G/$1\times$BTZ, or $2\times$BTZ is 1:2:1; in other words, there is only a 25% chance of having either two R6G or two BTZ molecules present in the laser focal volume at the same time. For two molecules ($n=2$), we have simply used the binominal formula $(a+b)^2=b^2+2ab+b^2$ with a = R6B and b = BTZ. For n molecules, the probability of finding only a or only b, i.e., a^n or b^n, decreases significantly according to the binominal distribution.

5.2.1.2. *The Isotopologue/Bianalyte Approach Using Isotopic Substitution*

The interpretation of bianalyte SM-SERS results (Section 5.2.1.1; SM = single molecule) requires knowledge on differences in Raman scattering cross-sections, absorption spectra, and surface binding affinities since the two analytes possess distinct vibrational, electronic, and surface-binding properties. The wavenumber-domain approach using two isotopologues is a very elegant extension, which builds upon the advantages of the bianalyte (BiASERS) approach, but at the same time avoids the limitations arising from the use of two chemically distinct analytes. In this respect, it may be considered as a very important special case of the bianalyte approach that is based on the "same" molecule. Specifically, it is based on two isotopologues, molecules that differ only in their isotopic composition. The use of two isotopologues such as R6G-d_4 and R6G-d_0 (Figure 37) for SM-SERS has additional significant advantages since their electronic absorption spectrum, their Raman scattering cross-section, and their surface-binding affinity are the same.

The wavenumber ("frequency") domain discrimination between the two isotopologues is possible due to their distinct vibrational Raman spectrum: wavenumber positions and intensities of peaks due to normal modes involving the C-D groups are changed, as shown for R6G-d_4 and R6G-d_0 in Figure 38. Based on the two peaks at 622 cm^{-1} (R6G-d_0) and 610 cm^{-1} (R6G-d_4), an unambiguous discrimination between the two isotopologues is possible; the claim of single-molecule behavior is qualitatively therefore straightforward. If, on average, only one type of molecule is adsorbed on each NP, then each SM-SERS spectrum contains only the spectral fingerprint of one of the two isotopologues, while it contains both fingerprints for larger surface coverages. Quantitatively, the probabilities for observing the two isotopologues should follow the binominal distribution.

The isotopologue approach has been applied not only to artificial isotopologues, but also to natural isotopologues in order to demonstrate the natural isotope distribution

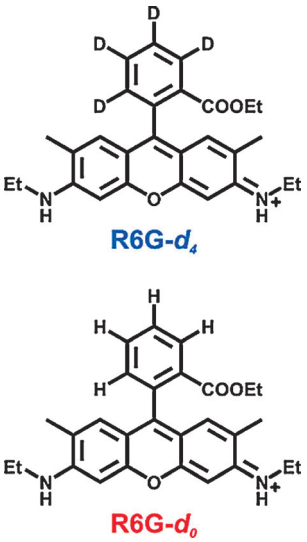

Figure 37. R6G-d_4 and R6G-d_0 for use in the isotopologue-based approach to single-molecule SERS. From Ref. [96].

of elements such as carbon, by using the highly localized stretching vibration of a cyano moiety as a probe.[97]

The wavenumber ("frequency") domain proof-of-existence should become the new "gold standard" in SM-SERS since it eliminates a series of ambiguities present in earlier approaches. The chemical synthesis of the corresponding isotopologues—although time consuming and possibly more challenging and/or expensive for other molecules—should definitely be worth the effort; only results obtained by this approach can be directly interpreted and will significantly promote SM-SERS to become a generally accepted SM technique.

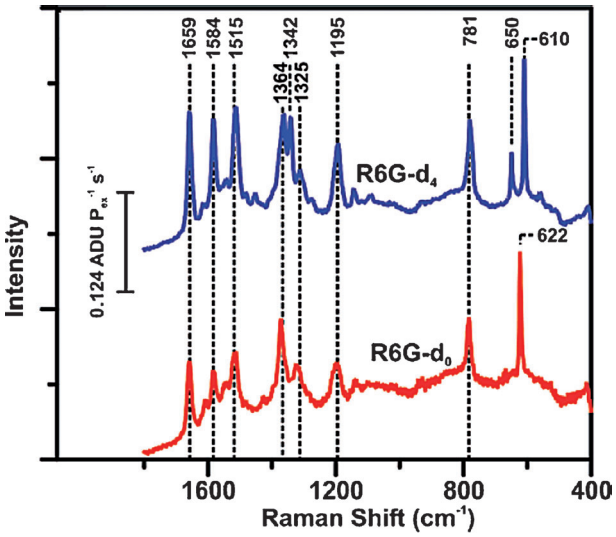

Figure 38. Isotopologue/BiASERS for the wavenumber-domain-based demonstration of single-molecule SERS. From Ref. [96].

5.2.1.3. *Single-Molecule SERS of Nonresonant Molecules*

For resonant molecules such as dyes with differential cross-sections on the order of 10^{-27} $cm^2 sr^{-1}$ for the most intense Raman modes, EFs on the order of 10^8 are fully sufficient to obtain SM-SERRS.[29] Calculations predict electromagnetic EFs at hot spots of 10^{10}–10^{11} for certain configurations such as dimers of metal nanospheres (see Section 3.1). These extreme EFs should be sufficient to bridge the gap between resonant and nonresonant molecules since the latter exhibit differential cross-sections on the order of 10^{-30} $cm^2 sr^{-1}$. The fact that the Raman scattering cross-section of nonresonant molecules is 1000 times lower than that of resonant molecules is compensated by a 1000-fold higher EF. Figure 39 shows the absorption spectra of the nonresonant molecule 1,2-di-(4-pyridyl)ethylene (BPE) and the benzotriazole dye 3-methoxy-4-(5′-azobenzotriazolyl)-phenylamine (BTZ, resonant molecule) for use in BiASERS studies.[29]

Several aspects must be considered when performing SM-SERS experiments on nonresonant molecules.[29] First, the long-tail distribution of EFs in SM-SERS must be kept in mind (cf. Sections 3.1.2 and 3.1.3): only molecules at hot spots with the highest possible enhancement of 10^{11} can be detected. Since nonresonant molecules are significantly less prone to photobleaching, which limits the applicable laser power density and integration time, this figure can be partly reduced by adjusting the laser power density and the integration time. Nevertheless, from a purely electromagnetic enhancement point of view, a much narrower range of enhancements is "usable" at the top of the distribution to push signals above the minimum signal-to-noise ratio. This narrow range of extremely high enhancements corresponds to a much smaller effective number of hot spots that are usable; it is only the EF region right around the maximum which provides enough enhancement to produce a SM-SERS signal. In addition to this statistical aspect related to the EF

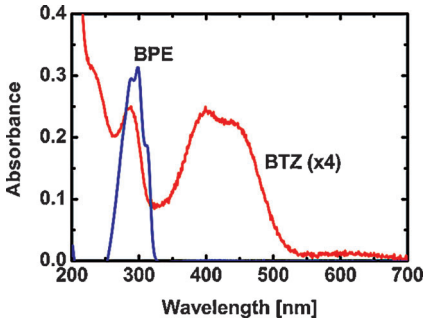

Figure 39. Absorption spectrum of BPE ("nonresonant" molecule) and BTZ ("resonant" molecule). From Ref. [29].

distribution, also contamination issues become critical since competing molecules with similarly weak Raman scattering cross-sections also contribute and complicate the analysis. In order to minimize the presence of such contaminants, the preparation of the SERS substrate was optimized. Instead of using the citrate reduction method, sodium boron hydride was used as a reducing agent. Figure 40 shows the SM-SE(R)RS

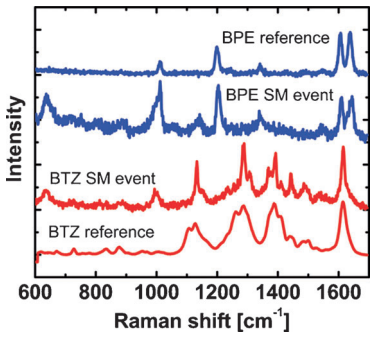

Figure 40. SM-SERS spectra of BPE and BTZ together with their reference ensemble spectra. From Ref. [29].

spectra of BPE and BTZ, respectively, together with their corresponding ensemble spectra as a reference. The authors conclude that—given their conclusive experimental demonstration—in principle any molecule that can be made to adsorb on the substrate can be observed at the single-molecule level with SERS.

Structure–activity correlations on single particles showed that dimers of Ag nanocrystals are the simplest of several possible configurations capable of producing SM-SE(R)RS.[98]

In addition to this plasmonic/EF aspect, it is important to confine the molecules to the hot spot regions. Different approaches to achieve this exist, including Langmuir–Blodgett layers,[92,94] junctions between gold nanostars and a planar gold surface,[99] and rationally designed DNA-modified Au NPs.[100,101]

5.3. Analytical Applications: From Sensing and Trapping to Solid-Phase Synthesis

5.3.1. Sensing

Biomolecular sensing using plasmonic nanostructures is an emerging topic with numerous applications.[102–104]

5.3.1.1. Stimuli-Responsive NPs for pH Sensing through Plasmonic Coupling and SERS

Plasmonic coupling can lead to very high electromagnetic field enhancements (cf. Sections 3.1.1 and 3.2.2). An interesting question is whether plasmonic coupling can be induced by molecular conformational changes. Stimuli-responsive polymers such as polymethacrylic acid (PMAA) offer this opportunity since they exhibit reversible conformational changes in response to environmental factors such as pH (Figure 41 a).[105] At pH > 4 the carboxylic acids are deprotonated, and the PMAA segment is hydrophilic and exhibits a random-coil expanded conformation. At pH < 3 the PMAA segment is nearly neutral and slightly hydrophobic, and it changes to a condensed or collapsed conformation (Figure 41 a). The pH-responsive PMAA segment is conjugated to an amphiphilic polyethylene glycol (PEG) block and a terminal lipoic acid (LA) anchoring group (Figure 41 a). Colloidal gold is incubated first with organic dyes as Raman reporter molecules and second with the LA-PEG-PMAA block copolymers (Figure 41). At pH > 4 these coated SERS NPs exhibit no plasmonic coupling due to strong steric and electrostatic repulsions (Figure 41 c, left). At pH < 3, however, the condensed conformation yields small clusters of coated SERS NPs (Figure 41 c, right). The corresponding SERS spectra (not shown here) demonstrate that at pH 7 no SERS signal is observed, in contrast to pH 3. The process is reversible as shown by a second cycle. Overall, this strategy allows one to control the distances and plasmonic interactions between block copolymer-coated metal NPs.

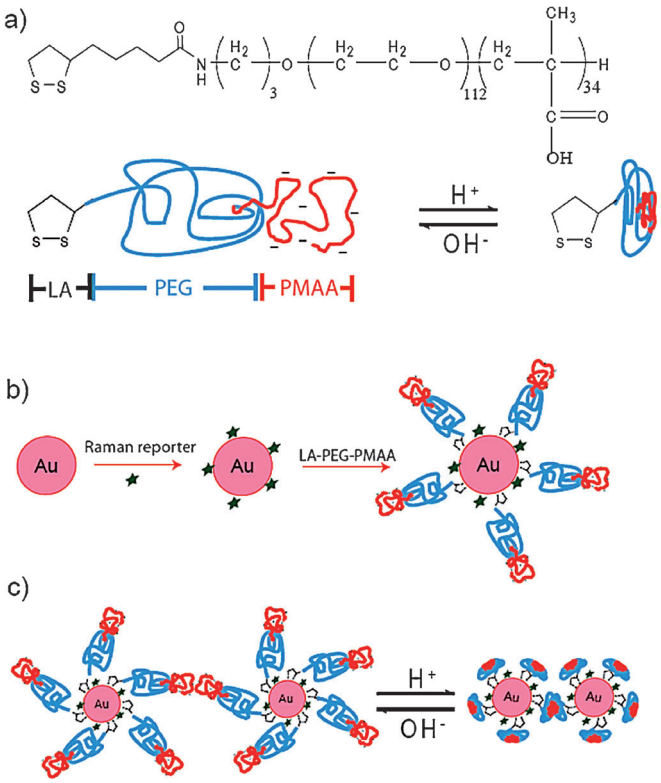

Figure 41. Polymethacrylic acid (PMAA) undergoes pH-dependent conformational changes, which are exploited for pH sensing through plasmonic coupling and SERS. From Ref. [105].

5.3.1.2. An All-Optical Nanoscale pH Meter

An equally elegant way to determine the pH by label-free SERS is to exploit the intrinsic pH sensitivity of molecules towards their state of protonation. 4-Mercaptobenzoic acid (4-MBA) is an ideal Raman reporter molecule since it strongly binds to gold or silver surfaces and the vibrational Raman spectrum of the protonated form (COOH, carboxylic acid) differs significantly from that of the deprotonated/ionized form (COO^-, carboxylate)(Figure 42).[106] Gold nanoshells coated with a self-assembled monolayer (SAM) of 4-MBA can therefore be considered as an all-optical nanoscale pH meter which reports on the local pH at the nanoshell surface (Figure 42). This label-free SERS approach was later applied to determine the local pH in living cells, e.g., in endosomes.[107–109]

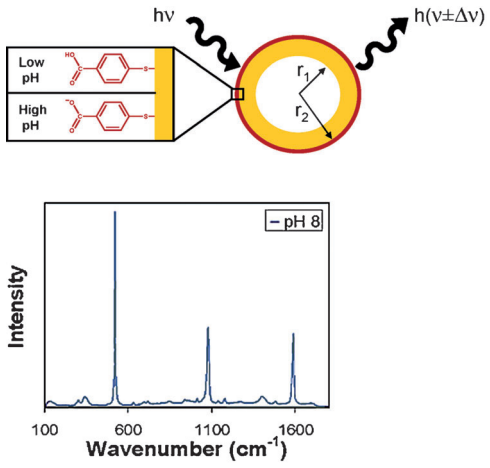

Figure 42. The SERS spectrum of 4-mercaptobenzoic acid (4-MBA) is used for all-optical pH sensing using gold nanoshells coated with a SAM of 4-MBA as a nanoscale pH meter. From Ref. [106].

5.3.1.3. Sensing Polycyclic Aromatic Hydrocarbons: Exploiting Host–Guest Interactions

A further important analytical application of SERS is environmental monitoring.[110] One example of extremely hazardous pollutants are polyaromatic hydrocarbons (PAHs), which are mainly formed during the incomplete combustion of coal, oil, and gas as well as tobacco. Many of them have been reported to be strongly carcinogenic. PAHs such as coronene (blue in Figure 43 middle left) contain condensed

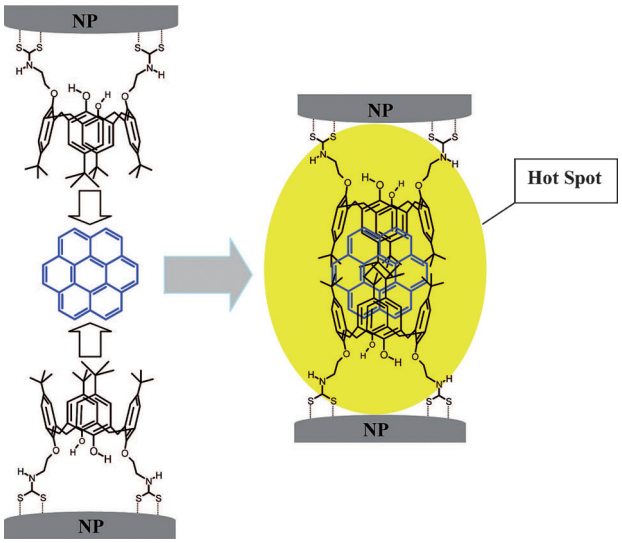

Figure 43. Sensing polycyclic hydrocarbons ("guests"; in blue: coronene) by SERS in a hot spot by using dithiocarbamate-"host"-conjugate-functionalized silver NPs ("host"). From Ref. [111].

benzene rings as a common molecular structure; they exhibit a very low affinity for adsorption on metallic surfaces due to their lack of functional groups, in particular hetero atoms such as sulfur or nitrogen, and are therefore a very challenging albeit important class of analytes. Exploiting host–guest interactions, a concept familiar from supramolecular chemistry, is the key to their highly sensitive and specific detection by SERS.[111–113] The surface of silver NPs is functionalized by a dithiocarbamate–host conjugate. Figure 43 shows the formation of a hot spot in the interparticle junction when two host-functionalized silver NPs jointly complex a coronene molecule as a guest.[111] This elegant concept has been successfully applied to other PAHs including pyrene and triphenylene. Affinity constants and the limits of detection were determined for each PAH from concentration-dependent SERS studies.[111]

5.3.1.4. ***Glucose Sensing***

Patients with diabetes mellitus must monitor their glucose levels frequently since their bodies fails to produce or to respond to insulin, a hormone that regulates glucose metabolism. The resulting large fluctuations in the glucose levels can cause severe complications such as kidney and heart diseases. Most patients use a "finger-prick" apparatus for removing small samples of blood in a painful and inconvenient way. Therefore, many research groups are trying to develop minimally invasive and biologically compatible methods for quantitative glucose detection, including techniques such as mid-infrared absorption and laser polarimetry. Conventional or normal Raman spectroscopy is capable of detecting glucose at physiological concentrations in vitro; for comparison purposes: the Raman scattering cross-section of glucose is only five times smaller than that of benzene and 50 times larger than that of water. However, the laser exposure in terms of laser power and acquisition time is relatively high, in particular higher than biologically permissible. The signal increase in SERS overcomes this limitation by maintaining the high chemical specificity of vibrational Raman spectroscopy. AgFON (Section 4.2.1) as the SERS substrate in combination with partial least squares (PLS) as a chemometric method was successfully employed for quantitative glucose sensing. A key element is the use of a partition layer on the surface of the AgFON substrate for generating a glucose concentration gradient (Figure 44).[114] A dozen

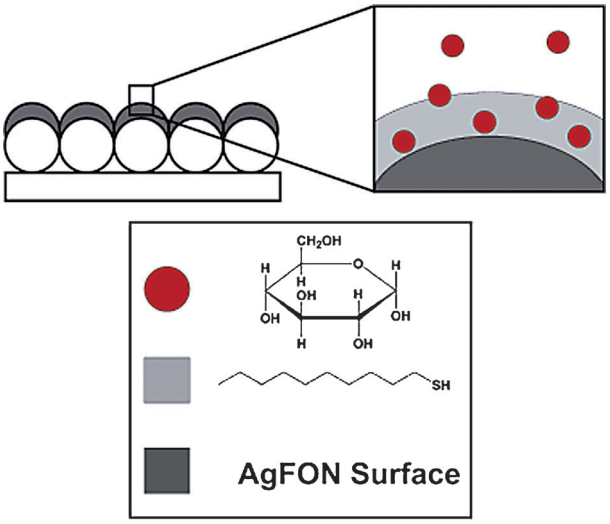

Figure 44. Sensing glucose on a silver film over nanospheres. The 1-decanethiol partition layer ensures the necessary preconcentration. From Ref. [114].

different partition layers were studied, but only straight alkanethiols were found to be effective; in this study, 1-decanethiol (1-DT) was employed. It is important to note that without this partition layer, SERS of glucose could not be observed since the necessary preconcentration—bringing glucose molecules in close vicinity to the plasmonic AgFON surface—is missing in this case. Concentration-dependent studies in the 0–250 mM range were performed in order to determine the accuracy of this approach and to estimate the limit of detection. Partial least squares/leave-one-out (PLS/LOO) analysis was chosen as a chemometric technique for data evaluation since the analyte spectrum (glucose) is embedded within a complex background spectrum. Plots of PLS-predicted concentrations versus the actual concentrations yielded a root-mean-squared error of prediction (RMSEP) of 1.8 mM = 33.1 mg dL^{-1} for the physiologically relevant concentration range (Figure 45), which is close to that desired for medical applications. The calibration vectors used to generate the prediction plot in Figure 45 contain characteristic vibrational Raman bands of glucose, indicating that they represent portions of the glucose spectrum that do not overlap with bands of the partition layer or of analytes present in the background. Nevertheless, 1-DT is not considered to be the optimum SAM and there is certainly room for improvement. The authors note that a systematic search for improved partition layers with higher partition coefficients

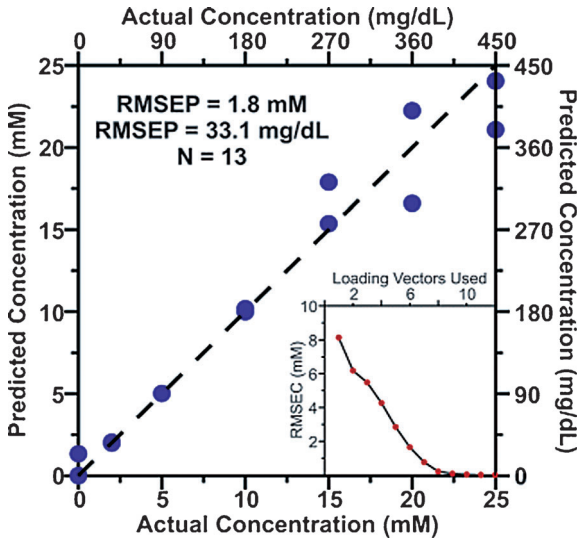

Figure 45. Concentration-dependent SERS measurements of glucose using the approach depicted in Figure 44. From Ref. [114].

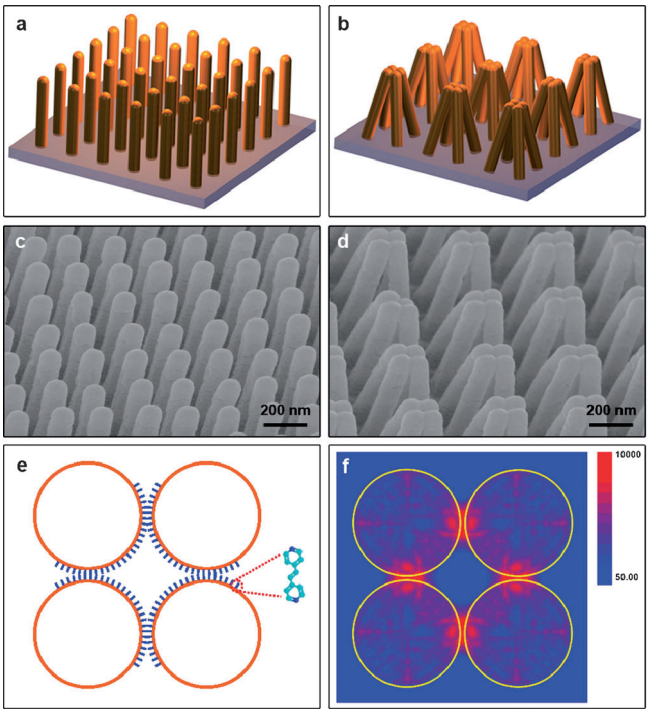

Figure 46. Gold fingers in the open (A) and closed (B) form, together with SEM images and results from computer simulations highlighting the hot spots. From Ref. [116].

and less spectral overlap with glucose Raman bands is in progress. A further improvement would be to switch from visible laser excitation employed in this study to the "biological window" in the near-infrared between 700–1200 nm.

5.3.2. *Trapping*

In addition to partitioning (cf. Section 5.3.1.4), trapping and caging molecules[115] are also very promising approaches for confining the corresponding analyte in small volumes close to the metal surface.

5.3.2.1. *Gold Nanofingers*

An extension of the silver nanowire approach (cf. Section 4.2.5) is based on gold nanofingers for molecule trapping and detection. This approach addresses two key issues: a) Control over the critical sub-nanometer dimensions, which is difficult to achieve with conventional nanofabrication schemes; b) The analyte may not be located in the hot spots, even if the hot spots could be precisely prefabricated. Gold-coated flexible polymer fingers can perform both functions: they can close to trap the molecules and, at the same time, they form reliable hot spots.[116] This system is therefore a generic platform for both molecule trapping and SERS sensing.

Figure 46 shows the gold fingers in the open (a) and closed (b) state; the corresponding SEM images are shown in (c) and (d), respectively. High-density square arrays of free-standing polymer nanofingers were fabricated by nanoimprint lithography followed by gold coating. The finger closure is driven by capillary forces which occur after deposition of the liquid onto the finger and its subsequent drying. Figure 46e shows schematically how the molecules are trapped inside the nanofingers. The spatial distribution of the electric field intensity in this configuration, calculated within the discrete dipole approximation (DDA), demonstrates the appearance of hot spots at the junction between two adjacent gold fingers.

Control experiments were performed in order to demonstrate the actual trapping of molecules between the gold fingertips. The SERS signal upon immersion of the gold nanofingers in a solution of the analyte and drying, i.e., the concerted action of the anticipated molecule trapping and finger closure, was two times higher than that obtained in a sequential procedure, in which only the solvent was evaporated for finger closure followed by the addition of the probe molecule.

5.3.2.2. *Silica-Void-Gold Nanoparticles as Temporally Stable SERS Substrates*

The high surface energy and resulting instability of metal colloids often leads to aggregation and irreproducible SERS signals. The stability of metal colloids is therefore of crucial importance for obtaining reproducible SERS signals. On the one hand, protecting metal nanoparticles by stabilization agents should prevent particle aggregation and on the other hand, the plasmonic/optical properties should be maintained.

Silica-void-gold NPs obtained by encapsulation of Au NP cores in porous silica membranes fulfill both criteria (Figure 47 right).[117] The porosity of the membrane allows molecules to diffuse through the silica network and to get into contact with the gold core. First, Au NPs are entrapped by a silica shell (step 1 in Figure 47). Selective etching of the internal silica matrix in these Au@SiO_2 particles (step 2), which is less dense and cross-linked than the highly cross-linked external silica matrix, leads to internally etched (IE)

$Au@SiO_2$ particles. Extending the etching time results in hollow IE $Au@SiO_2$ spheres with freely moving Au cores (step 3), and finally hollow IE $Au@SiO_2$ spheres with an etched external membrane (step 4). Figure 48 depicts representative TEM images of NPs obtained during the synthesis of the hollow IE $Au@SiO_2$ spheres.

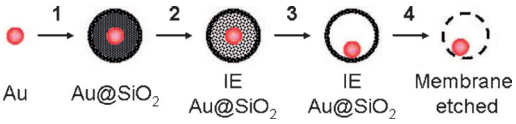

Figure 47. Synthesis of silica-void-gold $Au@SiO_2$ nanoparticles. Analyte molecules can diffuse through the pinholes of the etched silica structure and reside there for SERS detection based on the Au NPs. From Ref. [117].

The etching process has been monitored by extinction spectroscopy and a model for explaining the formation of the silica membrane was provided.

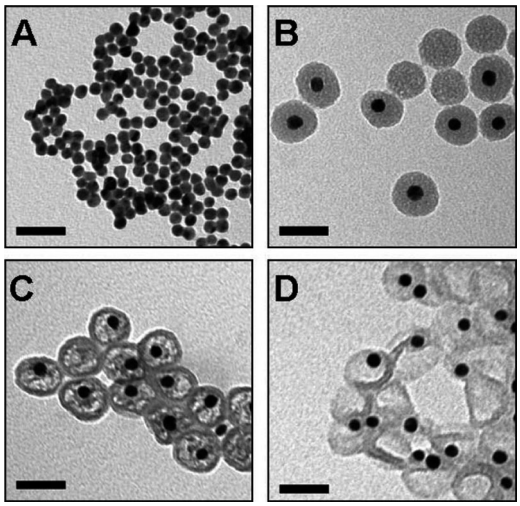

Figure 48. TEM images of nanoparticles obtained during the synthesis of silica-void-gold $Au@SiO_2$ NPs. From Ref. [117].

5.3.2.3. Thermoresponsive Nanocomposites as Molecular Traps for SERS

The vast majority of analytical applications of SERS rely on the adsorption of the analyte on the metal surface. Nitrogen- and sulfur-containing compounds, which usually have a high affinity to silver and gold surfaces, are therefore more or less routinely detected by SERS.

Controlling the surface charge of the colloid is an alternative approach for bringing the analyte onto or close to the metal surface, for instance by electrostatic attraction. Examples for this approach focus on carboxylic acids and amines, while it is hardly helpful for the detection of alcohols, ethers, and other oxygen-containing groups as well as nonfunctionalized molecules.

How can nonfunctionalized molecules, in other words, molecules without surface-seeking groups, be trapped? And how can they be brought close to the plasmonic substrate for SERS detection (cf. SERS distance dependence in Section 3.4)? Thermally responsive microgels containing a gold core are a promising way of achieving this. The polymer shell can swell or collapse as a function of temperature; this change in volume is expected to serve as a means to trap the nonfunctionalized molecules and get them sufficiently close to the metal core.

The synthesis of the SERS-active nanocomposites in Figure 49[118] starts with cetyl trimethyl ammonium bromide (CTAB)-coated, 67 nm gold nanospheres coated with a thin polystyrene (PS) shell. Then the thermoresponsive microgel around this AuNP@PS core is formed by polymerization of *N*-isopropylacrylamide (NIPAM) and a cross-linker. The size of the 67 nm Au core within these AuNP@pNIPAM nanocomposites can be increased by seeded growth using $HAuCl_4$ and ascorbic acid as reducing agent. The resulting 116 nm Au cores exhibit a significantly larger scattering intensity than the 67 nm Au cores.

Figure 49 schematically shows the application of these AuNP@pNIPAM nanocomposites for the detection of noninteracting probes, i.e., molecules with no predisposition to adsorb onto the gold surface. At 4 °C (Figure 49 middle), no SERS signals are observed due to the large spatial separation of the probe molecule and the Au core. Upon heating to 60 °C (Figure 49 right), the thermoresponsive shell contracts and SERS can now be detected.

The microgel has several key advantages: 1) The porous, protective pNIPAM shell enhances the long-term stability of the colloidal nanocomposite. 2) The shell prevents plasmonic coupling between the particles, providing a highly reproducible SERS signature, which is a necessary condition for quantitative SERS. 3) The overall SERS intensity from the pNIPAM shell itself is low, which is important for ultra-

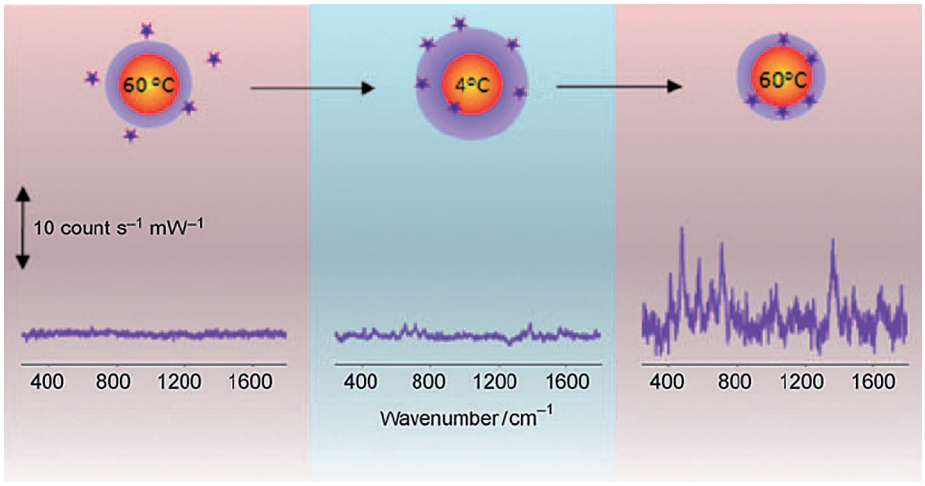

Figure 49. SERS detection of molecules without surface-seeking groups using thermoresponsive polymers on Au NPs. From Ref. [118].

sensitive applications relying on a nanocomposite detection system with low background.

5.3.3. SERS for Direct Detection of Solid-Phase-Bound Compounds

5.3.3.1. SERS Detection through External Plasmonic Nanostructures

Solid-phase synthesis (SPS) of peptides has revolutionized bio-organic synthesis. The solid support in SPS is in most cases a modified polystyrene resin with a low loading of typically about 100 pmol per bead. This makes the direct analysis of solid-phase-bound compounds directly on bead challenging. Any spectroscopic attempt to directly detect a molecule bound to a single micron-sized SPS bead has to cope with the low loading and the presence of a significant excess of the solid support itself. Figure 50 shows schematically how

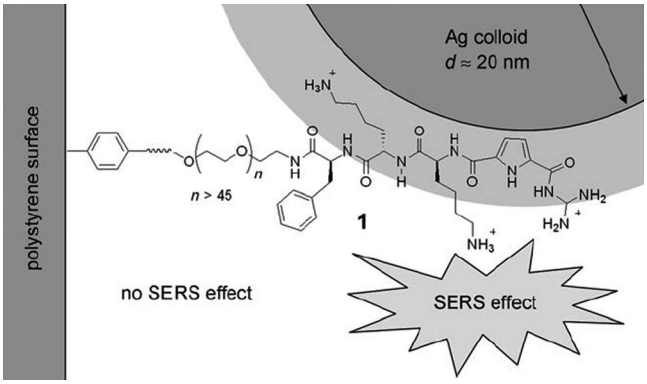

Figure 50. SERS detection of solid-phase-bound molecules using colloidal silver. From Ref. [119].

colloidal SERS was used for the direct and label-free detection of an artificial peptide receptor (**1**), which was bound on the polystyrene surface of a micron-sized bead.[119] Colloidal silver particles with a diameter of roughly 20 nm are added to the surface. Upon resonant laser excitation, only the solid-phase-bound compound **1**, which is in close vicinity to the Ag surface, experiences the high near-field enhancement and is observed in the corresponding SERS spectrum. In contrast, the solid-phase support itself, the polystyrene surface, is too far away from the Ag colloid to experience this enhancement and is expected not to be detectable. The main drawback of this approach is that the bare silver NPs can directly interact with the analyte of interest and may perturb its electronic, vibrational, and/or conformational properties.

5.3.3.2. Integrated Solid-Phase Synthesis and Label-Free SERS Analysis with Plasmonically Active Micron-Sized Beads

A more recent approach circumnavigates this problem and integrates the two functionalities—SPS and direct label-free on-bead SERS analysis—into a single bifunctional unit (Figure 51).[120] The surface of single micron-sized beads is completely covered by 80 nm gold nanospheres with an ultrathin silica shell (Figure 51 a,b) as in the SHINERS

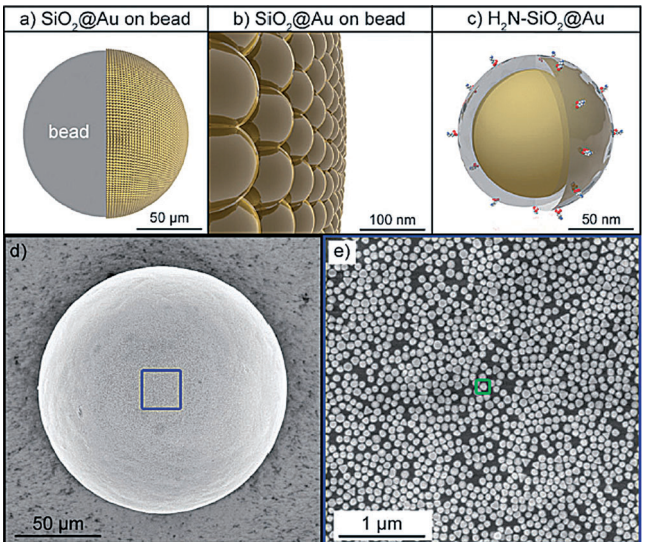

Figure 51. Micron-sized beads covered by 80 nm Au NPs with a very thin silica shell for integrated solid-phase synthesis and direct on-bead SERS detection. From Ref. [120].

approach (Section 4.1.1). The surface of the glass shell is then functionalized with amino groups for subsequent SPS (Figure 51 c). SEM images show the dense packing of the gold/silica core/shell NPs on the surface of the micron-sized beads (Figure 51 d,e). The ultrathin silica shell (2–3 nm) can be recognized in the TEM images (not shown). Direct and label-free SERS microspectroscopy demonstrated the presence of amino acids and a dipeptide as well as the ability to differentiate between them based on their intrinsic vibrational signature. To become generally applicable, the concept certainly has to work also for longer oligopeptides.

5.4. Bioanalytical Applications: Nucleic Acids and Proteins

SERS has a large potential in bioanalytical applications in vitro and in vivo.[121–125] This section focuses on the detection of nucleic acids and proteins as highly important classes of biomacromolecules.

5.4.1. Nucleic Acid Detection

5.4.1.1. DNA/RNA Detection Using NPs with Raman Spectroscopic Fingerprints

An important step in nanobiotechnology was the use of oligonucleotide-functionalized NPs for the highly sensitive and selective detection of DNA,[126,127] using silver deposition for signal enhancement and a flatbed scanner for detection. A disadvantage of this approach is its inherent limitation to one color (gray scale). Multiplexed detection of different DNA/RNA sequences was demonstrated by using metal colloids functionalized with Raman dye-labeled oligonucleotides capped with alkylthiols. In this case surface-enhanced resonance Raman scattering (SERRS), which occurs when the laser wavelength matches an electronic absorption of the molecule on the surface of the plasmonically active nano-

structure, was employed for detection. The additional signal enhancement due to this molecular electronic resonance makes SERRS a highly sensitive vibrational spectroscopic technique.

Small Au NPs with a diameter of ca. 13 nm (Figure 52 top) were functionalized with Cy3-labeled, alkylthiol-capped oligonucleotide strands.[128] For hybridization, the target DNA and the small Au SERS probes were sequentially added to the chip functionalized with the corresponding capture sequence. Next, silver enhancement was performed by the reduction of silver ions with hydroquinone for the sensitive SERRS detection of the hybridization event.

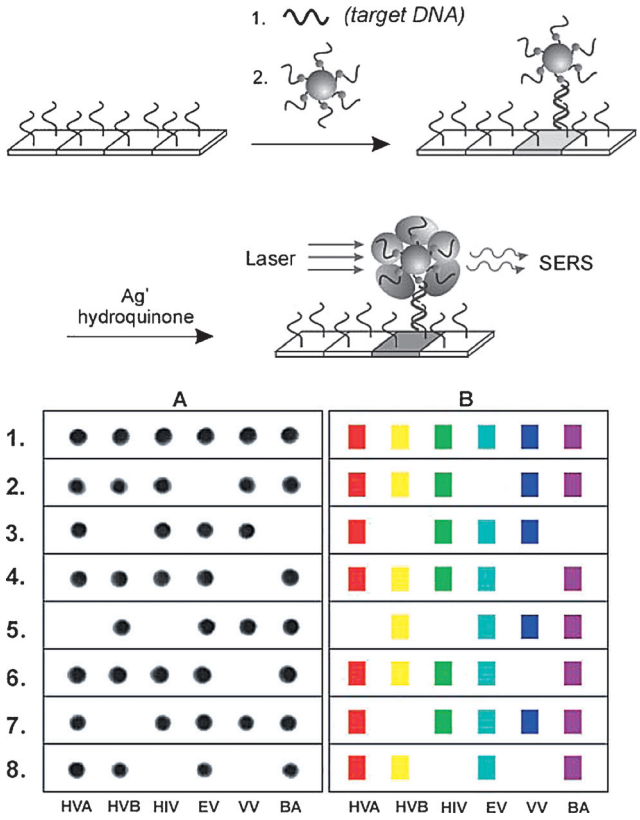

Figure 52. Target DNA detection with dye-labeled, oligonucleotide-functionalized Au NPs with subsequent silver staining for SERRS detection. From Ref. [128].

Flatbed scanner images of the chip before (A) and after silver development (B) were recorded (Figure 52), demonstrating that the corresponding spots on the chip can be detected only after silver staining. A typical Raman/SERRS spectrum exhibits the characteristic vibrational peaks of the dye Cy3. SERRS intensity line profiles (not shown) were obtained by horizontally moving the laser spot (ca. 25 μm diameter) across the chip and plotting the intensity of the intense Raman marker peak at 1192 cm^{-1}. SERRS is observed at all locations with silver spots (maxima in the intensity profile), while no signals are observed in between the spots (minima in the intensity profile).

In a multiplexed version of this approach, six commercially available dyes—Cy3, TAMRA, Texas Red, Dy3.5, Rhodamine 6G, and Cy5—were conjugated to different oligonucleotide sequences specific for six different targets including several viruses (Figure 52 bottom). The Raman spectra of the six dye-labeled NPs obtained after silver staining are each encoded with a single color (Figure 52 bottom right). Fluorescence from the dyes is quenched due to radiationless energy transfer from the molecular fluorophore to the metal surface; in other words: at metal-to-dye distances below a few nanometers, SERRS dominates over fluorescence.

The selectivity of the approach was determined by using a silver-enhanced microarray containing eight different tests. Both flatbed scanner (gray scale) and SERRS-encoded images (Figure 52 bottom) were recorded and analyzed. In the first test (row 1), in which all eight different target strands were added, all spots show the same intense gray color associated with Ag deposition. Their "identity" can easily be determined with the corresponding color-encoded Raman spectra because the correlation of the oligonucleotide sequence and the corresponding SERRS spectrum of the dye attached to it is known. Different combinations of target strands, in particular leave-one- and leave-two-out experiments, were performed in the seven other tests (rows 2–8). The concentration of the target strands was kept constant in all experiments (100 pM each). In this set of experiments, no false-positive or false-negative results are observed. Unoptimized detection limits of 20 fM were obtained.

This contribution has been very influential for bioanalytical SE(R)RS, stimulating further research activities on multiplexed detection of nucleic acids and other biomacromolecules, in particular proteins (Section 5.4.2).

5.4.1.2. *Quantitative and Multiplexed DNA Detection by SERRS*

After this proof-of-principle study (Section 5.4.1.1), it was necessary to investigate several analytical key aspects before using SERRS for routine detection of DNA.[129–131] This includes the concentration range accessible for quantitative predictions, the detection limit for commonly available dyes used as Raman reporters, the number of available dyes, and the optimum buffer conditions.[131] Multiplexing can be achieved by exciting SERRS from several dyes with a single laser wavelength. An alternative is to use two different laser excitation wavelengths, each of them matching the electronic absorption of a particular subset of dyes.[132] The limit of detection for the dyel-labeled oligonucleotides was in the 3–30 pM range for the multiplexed SERRS assay.

5.4.1.3. *DNA-Based Self-Assembly of Dye-Coded Nanoparticles into Larger Clusters*

DNA-based self-assembly upon molecular recognition of a target strand is a powerful and elegant approach to achieve plasmonic coupling between metal NPs. This concept, originally demonstrated for oligonucleotide-labeled Au NPs,[126,127] has been extended to a sandwich assay with silver NPs coated with Raman dyes and oligonucleotides (Figure 53).[133] Benzotriazoles were used as Raman dyes due to their high affinity to the surface of the silver colloid and

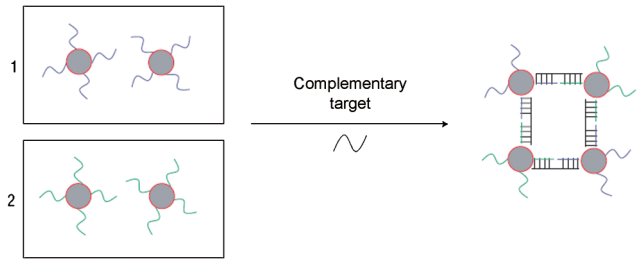

Figure 53. Controlled DNA-based self-assembly of dye-coded oligonucleotide-functionalized silver colloids. From Ref. [133].

their large Raman scattering cross-sections, giving rise to intense SERRS signals. The colloid coated with a monolayer of benzotriazoles was then incubated with two different, noncomplementary 5′-thiol-functionalized oligonucleotide sequences (**1** and **2** in Figure 53). Hybridization occurs when a target sequence complementary to both sequences (**1** and **2**) was added to the Raman-dye-functionalized DNA/Ag-NP conjugates. The controlled DNA-based assembly can be monitored with the naked eye by means of the color change from yellow (single silver particles) to green–blue (assembly). In order to test the sequence discrimination effect of the DNA–silver conjugates, the assembled colloid was heated and cooled. The melting curves, monitored by the extinction at the wavelength of the plasmon peak, display the same sharp transition reported for other oligonucleotide–NP conjugates.[133] This is important since it demonstrates that DNA present in the DNA–colloid conjugates is capable of undergoing sequence-specific hybridization.

Figure 54 shows the SERRS spectra of DNA- and Raman-dye-functionalized silver colloids exposed to a fully complementary target sequences (**1**, strong SERRS signal) and to

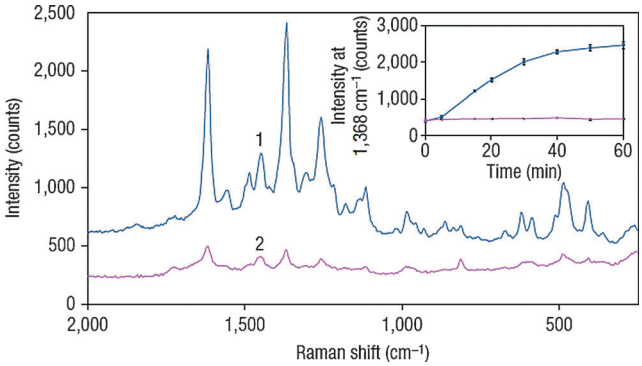

Figure 54. DNA-based self-assembly of dye-coded oligonucleotide-functionalized silver colloids exposed to fully complementary (1) and half-complementary (2) DNA strands. From Ref. [133].

a half-complementary sequence (**2**, weak SERRS signal).[133] The inset in Figure 54 shows the corresponding hybridization profiles obtained by plotting the intensity of the 1368 cm^{-1} peak of the benzotriazole dye as a function of time. These results clearly show the transition from non-aggregated Raman-dye-coated Ag NPs ("off" state) to defined assemblies through DNA hybridization ("on" state). The use of multiple Raman dyes for SERRS monitoring of this process rather than just monitoring changes in the extinction spectrum offers the advantage of exploiting the multiplexing potential of vibrational spectroscopy since different Raman dyes with different SERRS spectra can encode for different target oligonucleotide sequences.

5.4.1.4. *Direct and Label-free Sub-Micromolar Detection of Mononucleotides*

In addition to the SERRS labeling strategies described above, classical label-free approaches can also be used for DNA detection. A possible way to reduce the chemical complexity of this task is to first analyze mononucleotides rather than the more complex oligo- or polynucleotides. Also for the routine detection of mononucleotides, a combination of sensitivity and reproducibility is required. High sensitivity in colloidal/sol-based approaches can be achieved by using aggregated colloids since they exhibit hot spots in the junctions between particles through plasmonic coupling. It was found that using electrolytes such as $MgSO_4$, which do not strongly bind to the surface of a silver sol, leads to very high SERS enhancements. Since Mg^{2+} ions bear a higher charge than the singly charged cations of alkaline metals such as Na^+ and K^+, the aggregation is stronger and therefore the SERS enhancements are very high. In these "Mg^{2+}-aggregated" colloids, anionic analytes such as mononucleotides may bind to the metal surface and thereby occupy surface binding sites by exchanging with the weakly bound citrate ions introduced in the Lee–Meisel synthesis.

Figure 55 shows that this simple concept of using $MgSO_4$ as an electrolyte for colloid aggregation has huge consequences on the SERS signal strength.[134] Spectrum (a) was obtained for 100 ppm dAMP, but in the absence of an

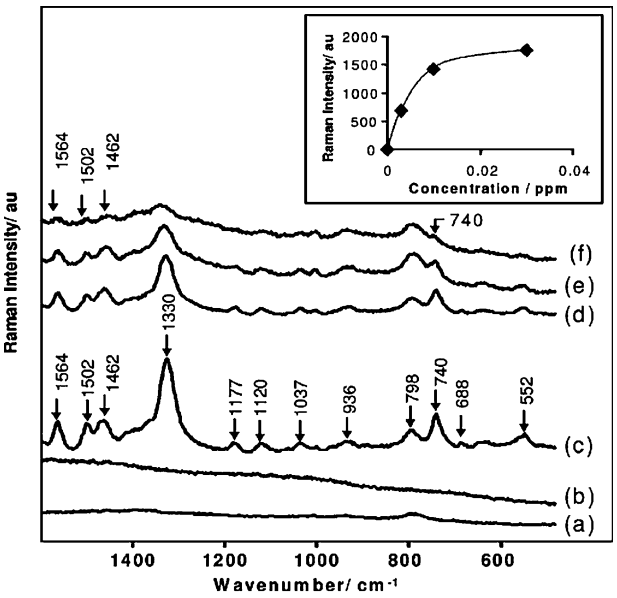

Figure 55. Label-free SERS detection of mononucleotides using different salts for inducing colloid aggregation (a–c). Concentration-dependent measurements yield a micromolar sensitivity (d–f; inset). From Ref. [134].

external aggregating agent and does not exhibit the characteristic Raman bands of dAMP. Spectrum (b) was acquired with excess chloride in solution as an aggregating agent, but only the characteristic band of the Ag–Cl bond at ca. 245 cm^{-1} (not shown) could be observed. With $MgSO_4$-induced aggregation (spectrum (c)), however, even at 100 ppb (10000 times higher dilution than in spectrum (b)), the distinct Raman bands of dAMP can be detected. The SERS spectra (d) to (f) show the concentration dependence, which is plotted in the inset. The limit of detection was found to be about 3 ppb or 10^{-8} M. Also high-quality SERS spectra of other nucleotides were recorded and compared. Their spectra are sufficiently different from each other, which is the basis for a label-free identification of mononucleotides with the advantages of rapid analysis, compatibility with high-throughput methods, and appropriately high, submicromolar sensitivity.

This label-free approach was recently applied to the detection of single base mismatches in short DNA strands (23- and 25-mer) based on the corresponding difference spectra, which contain features corresponding to the exchanged nucleotides.[135]

5.4.1.5. Direct and Label-free Detection of DNA Hybridization

The detection of selected nucleic acid sequences in hybridization assays is widely used in molecular biology and forensics. Commonly, fluorescent labeling of the target DNA is employed. Label-free approaches include, for example, also metal NPs and their change in color due to plasmonic coupling upon hybridization. In contrast, SERS provides the opportunity to achieve label-free DNA detection based on the vibrational fingerprint of the constituting molecular components. A major impediment of using in SERS for label-free DNA detection is the challenge of distinguishing a specific SERS signal due to hybridization of the target and probe sequence since both strands contain the same four DNA bases. Figure 56a shows that the SERS spectrum of thermally pretreated DNA on Au nanoshells (Au NS, silica core with Au shell) is dominated by a peak at 736 cm^{-1}, which is assigned to the ring breathing mode of adenine. The central idea is to remove adenine from the capture strand by replacing it with its isomer 2-aminopurine, which has a different spectral signature but preserves the same hybridization efficiency.[136] Figure 56b depicts the SERS spectrum of 2-aminopurine-substituted DNA anchored to the Au NS surface through a thiol moiety on its 5′-end. Instead of a peak at 736 cm^{-1} due to adenine (Figure 56a), now a peak at 807 cm^{-1} due to 2-aminopurine (Figure 56b) is observed. The inset of Figure 56 depicts the hybridization Scheme between such a 2-aminopurine-substituted DNA capture strand and a native/unlabeled, adenine-containing DNA target strand. Only the latter contains adenine and exhibits the characteristic and dominant peak at 736 cm^{-1}. In other words: the 736 cm^{-1} peak is a marker for hybridization between the native/unlabeled DNA target strand (left in the inset; with A = adenine) and the modified DNA capture strand (right in the inset; with 2-AP = 2-aminopurine). The intensity of the 2-AP peak at 807 cm^{-1} is constant and depends only on the packing density of the probe DNA on the surface of the Au NS. The peak

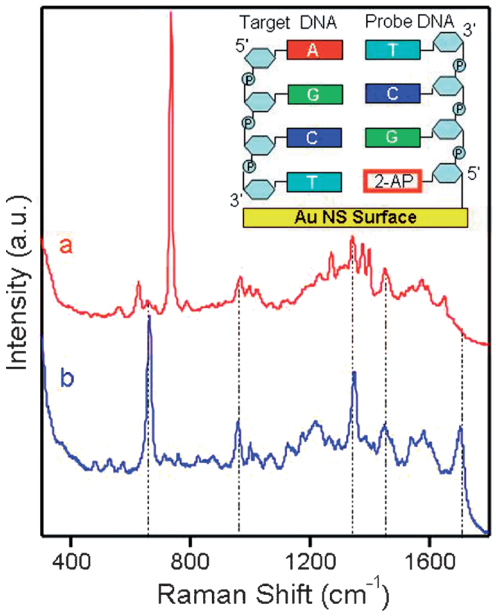

Figure 56. SERS spectra of native DNA (a) and 2-aminopurine-modified DNA (b). The target DNA can be identified by the characteristic adenine peak at 736 cm^{-1} (a; inset). From Ref. [136].

intensity ratio 736 cm^{-1} (A)/807 cm^{-1} (2-AP) is therefore a quantitative marker for the degree of hybridization. Overall, this contribution has demonstrated the label-free detection of DNA hybridization by SERS using a 2-AP-modified capture strand.

5.4.1.6. Discriminating Mutations in DNA Sequences

DNA hybridization assays can also be used for discriminating genomic mutations in DNA, which is important for DNA-based diagnostics and forensics. Usually either solution- or surface-based methods are employed. Quantitative polymerase chain reaction (qPCR), for instance, is a widely used solution-based approach. One advantage of surface-based approaches is that the conditions can be controlled locally at the surface; this is difficult for solution-based techniques. Furthermore, they enable spatial multiplexing in an array format, thereby paving the way for simple and portable biosensor devices (lab-on-a-chip). Surface plasmon resonance (SPR) sensing, for instance, is a widely used technique for detecting binding events through changes in the local refractive index. Apparently only few approaches so far have used a melting analysis by means of differential denaturation on solid substrates. Currently, fluorescence is the preferred technique for detecting mutations using such a hybridization/denaturation strategy.

Figure 57 top depicts three SEM images of sphere segment void (SSV; cf. Section 4.2.1) substrates at different resolutions, together with a computer-generated representation.[137] Modified capture strands comprise the disulfide at the 3′ end for strong binding to the Au@SSV surface as well as hexaethyleneglycol spacers attached at the 5′ end in order to prevent prohibitively close packing of the capture/probe sequences on the surface, ensure efficient hybridization, and

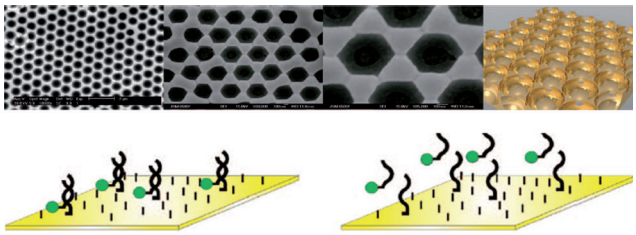

Figure 57. SERRS-based DNA-melting analysis of labeled target sequences hybridized to capture oligonucleotides on the surface of a metal film over gold nanospheres. From Ref. [137].

prevent cross-hybridization. After immobilization of the capture/probe oligonucleotides, the surface is treated with mercaptohexanol to prevent nonspecific binding. Then, the labeled target sequence hybridizes to the surface-bound capture strand with the labels placed close to the surface for ensuring efficient generation of SERRS (Figure 57 bottom left). Differential denaturation is induced either by a temperature or a potential ramp applied to the surface (Figure 57 bottom right). Finally, the surface is recycled by washing in order to remove any remaining target DNA strands, making it usable for another labeled target sequences. Figure 58 depicts

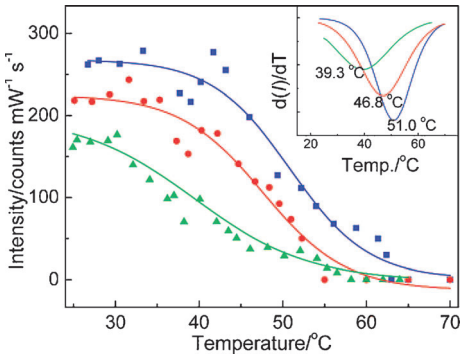

Figure 58. SERRS-based DNA-melting curves. From Ref. [137].

the results from a SERRS thermal melting analysis of three different target DNAs: wild type (filled squares, no mutation), single-point mutant (filled circles), and triple mutant (filled triangles, triple deletion). The wild type exhibits the largest melting temperature (51.0 °C), which is expected since its sequence perfectly matches that of the capture/probe sequence. The melting temperature observed for the single-point mutant is 46.8 °C, 4.2 °C lower than that of the wild type. The melting temperature for the triple mutant is the lowest (39.3 °C), demonstrating the imperfect match due to the triple deletion. The SERRS spectra were acquired from around 12500 molecules on the surface, which demonstrates that the presented SERS melting approach is a very sensitive method for discriminating single-nucleotide mutations.

5.4.2. *Protein Detection*

Proteins are another very important class of biomacromolecules and several concepts for the SE(R)RS detection of proteins are available.[138,139]

5.4.2.1. *Raman-Dye-Labeled Nanoparticle Probes for Protein Detection*

The concept of using Raman-dye-labeled Au NPs for DNA/RNA detection (Section 5.4.1.1) can also be applied to protein detection. Figure 59 shows two different types of probes developed for screening small-molecule–protein (A: type I) and protein–protein (B: type II) interactions.[140] Type I probes comprise 13 nm Au NPs coated with hydrophilic alkylthiol-capped oligonucleotides (A_{20}). Each oligonucleotide contains a small-molecule-recognition element such as biotin at one end and is modified with a Raman dye at the other end. Overall, very stable and water-soluble particles suited for use in complex assay environments are obtained, which specifically bind to the corresponding target molecule through their recognition element and exhibit the characteristic Raman/SERRS signature of the dye. Again, as in the case of DNA/RNA detection, the small linewidth of vibrational Raman bands provides the physical basis for multiplexed

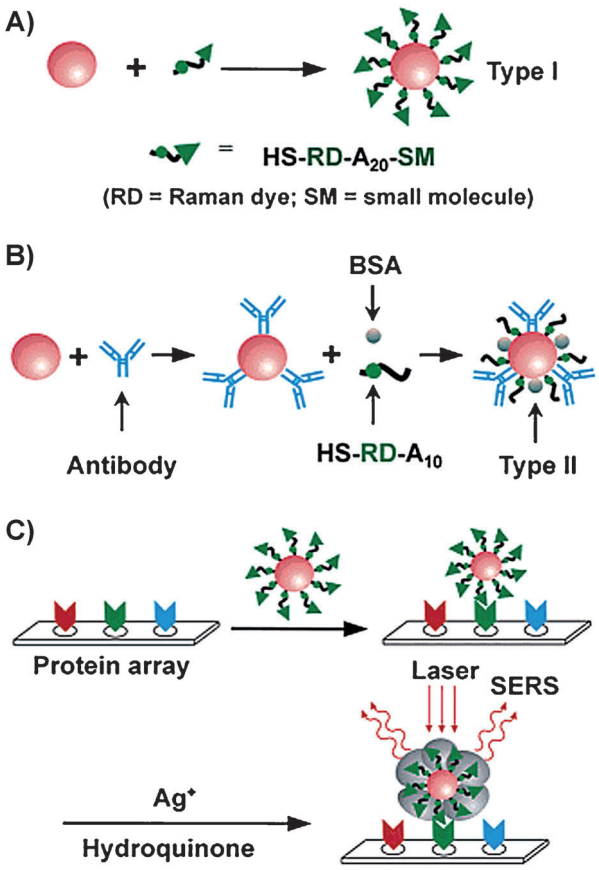

Figure 59. Two nanoparticle probes (A: type I, B: type II) for protein detection. SERS detection of type I probes after immobilization on a chip and silver staining. From Ref. [140].

detection schemes using Raman dyes/reporter molecules. Type II probes comprise 13 nm Au NPs equipped with an antibody for target (antigen) recognition, Raman-dye-modified alkylthiol-capped oligonucleotides for identification by the characteristic SERRS signature, and bovine serum albumin (BSA) to further passivate the metal surface.

Figure 59C shows how these probes are used in a protein array format. The protein chip was produced by spotting the protein solution onto a funtionalized glass slide. Then, the chip was exposed to a colloidal suspension of the Raman-dye-labeled nanoparticles probes. After washing and silver staining, gray spots on the chip can be detected by the naked eye. In subsequent Raman spectroscopic detection using a fiber-optic probe the corresponding SERRS spectrum of the dye was obtained. The effectiveness and selectivity of type I and type II probes was tested in a series of screening experiments using different target molecules.

5.4.2.2. *Immunoassays for the Detection of Proteins in Solution*

Sandwich immunoassays are routinely used in clinical diagnostics. Figure 60 shows the use of Raman-labeled gold colloids in a sandwich format.[141] First, a gold-coated glass surface is functionalized with the capture antibody (Figure 60A). Second, the coated chip is exposed to the sample in order to capture the corresponding antigen from the solution (Figure 60B). Finally, the sandwich complex is formed by the addition of the Raman-labeled colloid with the detection antibody.

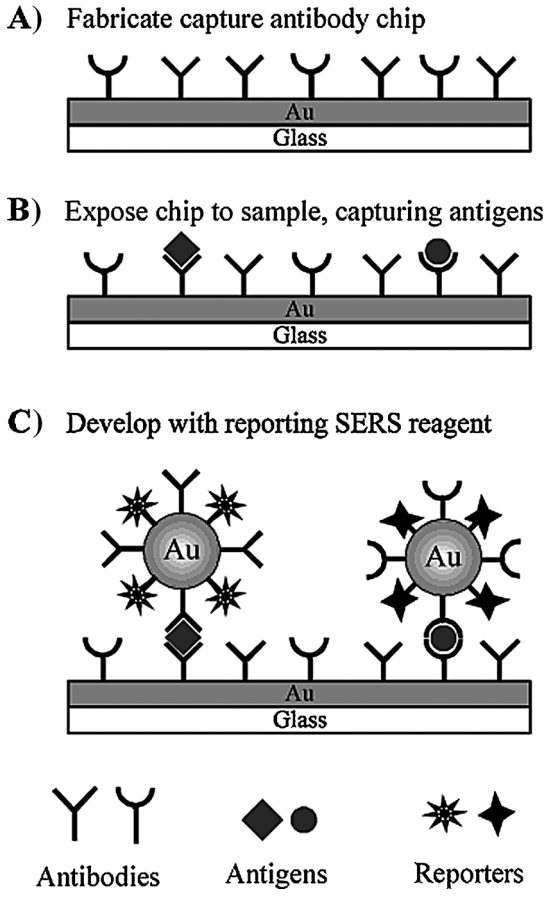

Figure 60. SERS sandwich immunoassay for protein detection. From Ref. [141].

This concept was applied to the SERS detection of prostate-specific antigen (PSA), a 33 kDa glycoprotein that has been used as a prostate cancer marker in serum tests.[141] The experimental setup for measuring PSA levels in human serum using SERS comprises a bifurcated fiber optical bundle for coupling the laser source to the Raman probe head, which focuses the light onto the sample area, and from the probe head to the spectrograph/CCD system for detection.

For the synthesis of the Raman-reporter-labeled immunogold colloid, 5,5′-dithiobis(succinimidyl-2-nitrobenzoate) (DSNB) serves as a Raman reporter molecule, which is already activated for subsequent bioconjugation. DSNB is synthesized from the corresponding biscarboxylic acid using standard N-hydroxysuccinimide (NHS) ester chemistry. Addition of the DSNB disulfide to the gold colloid leads to the formation of a self-assembled monolayer on the metal surface. The NHS ester terminus can subsequently react with the antibody by forming the corresponding amide.

Concentration-dependent sandwich immunoassays for PSA detection were performed (not shown). The SERS spectrum originates from the nitroarylthiol Raman label chemisorbed onto the surface of 32 nm Au NPs. The dominant Raman peak at 1340 cm^{-1} is assigned to the symmetric nitro stretching vibration. From PSA concentrations of 1000 $ng\,mL^{-1}$ down to 0.001 $ng\,mL^{-1}$, this Raman reporter peak can be observed (60 s acquisition time). A blank sample was employed as a negative control. The dose–response curve for free PSA in human serum was constructed by using mean values, averaging over different locations on the surface of each sample, with variations of typically 10%. Based on these data, a limit of detection of roughly 1 $pg\,mL^{-1}$ in human serum (60 s readout time) was determined. This sensitive SERS immunoassay is therefore suitable for detecting PSA at clinically relevant concentrations since normal levels of total PSA (free and complexed form) are between 4 and 10 $ng\,mL^{-1}$. The authors later reported an approach to make the rate-limiting step of antigen capture more effective by using a rotating rod.[142] This reduced the assay time from 24 h to 25 min and resulted in a 10-fold improved limit of detection.

5.4.2.3. *Immunohistochemistry: SERS Microscopy for Protein Localization in Tissues*

The selective localization of proteins in tissues by means of immunohistochemistry is central to histopathology. The proof-of-principle for immuno-SERS microscopy[143–145] demonstrated the selective localization of PSA in a prostate tissue specimen using a SERS-labeled primary antibody directed against PSA. During the last years, different Raman reporter molecules and metal colloids with different shapes and sizes have been employed for tissue imaging. One recent example is the use of gold nanostars, which are stabilized by hydrophilic ethyleneglycol-modified aryl thiols as Raman reporters (cf. Section 5.4.5).[146,147]

Figure 61 top shows TEM images of 60 nm gold nanostars (A) and of a single gold nanostar (B) and its tips at higher magnification (C).[147] Results from tissue imaging using gold

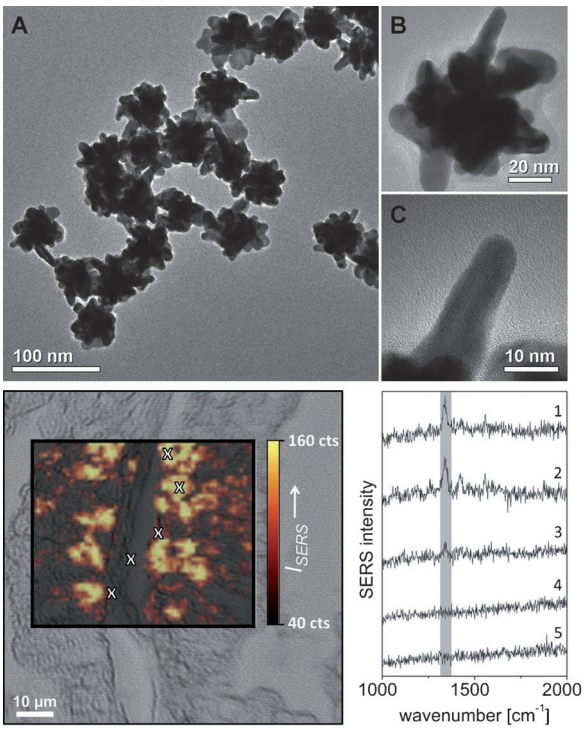

Figure 61. Immunohistochemistry with hydrophilically stabilized gold nanostars as SERS labels, conjugated to antibodies directed against p63. From Ref. [147].

nanostars conjugated to an antibody direct against the tumor suppressor p63, a p53 homologue, are shown in Figure 61 bottom left. A white light image of the prostate tissue section is overlaid with the corresponding SERS false-color image based on the intensity of the Raman marker band of the SERS label at 1340 cm^{-1} (Figure 61 bottom right). Spectra from five selected locations (Figure 61 bottom right) demonstrate that the signature of the SERS label is observed only in the basal epithelium (1–3) but not in the stroma (4) or lumen (5). Overall, these results indicate the selective abundance of p63 in the basal cells of the benign prostate. Also the proof-of-concept for the corresponding nonlinear variant of immuno-SERS, surface-enhanced coherent anti-Stokes Raman scattering (immuno-SECARS), has been demonstrated.[148]

5.4.3. Detection of Sequence-Specific DNA–Protein Interactions

Monitoring molecular interactions is an important aspect in bioanalytical chemistry. Figure 62 A shows a scaffold designed to selectively probe DNA–protein interactions. A double-stranded oligonucleotide C (oligo-C) contains the protein binding site of interest and provides appropriate spacing for protein access into the final assembly.[149] On each end of oligo-C, a 12-base-pair single-stranded overhang has a sequence complementary to oligonucleotides A and B (oligo-A and oligo-B), respectively, which are surface-bound on small gold nanoparticles. The target protein is recognized by means of the recognition site of oligo-C, while the oligo-A- and oligo-B-labeled Au NPs bind to the single-stranded overhangs at both ends of oligo-C and condense into an assembly. The target protein is labeled with a Raman dye for sensitive SERRS detection after silver plating (cf. Section 5.4.1.1). Nonspecific DNA–protein binding can be identified in control experiments using noncognate recognition sequences. Assemblies with cognate and noncognate sequences were spotted onto a glass plate and silver plated. Figure 62 B shows that the clusters are visible in white-light images at 50-fold magnification. Raman mapping experiments were performed in order to test the SERRS activity of the assemblies, using the integrated Raman intensity at 1641 cm^{-1} band of the Raman dye for the generation of SERS false-color images (Figure 62 C). The SERRS spectra in Figure 62 D demonstrate that only for cognate sequences strong SERRS signals are observed (solid lines), in contrast to the noncognate sequences (dotted lines), indicating little if any nonspecific protein binding.

5.4.4. Rational Design and Synthesis of SERS Labels: Chemical Considerations

A large variety of different SERS labels—metal colloids functionalized with Raman reporter molecules for conjugation to target-specific recognition elements such as antibodies and oligonucleotides—have been developed. Small Au NPs labeled with Raman dyes and subsequent silver staining after target recognition are just one example discussed above (Sections 5.4.1.1 and 5.4.2.1). A drawback is that the required plasmonic/SERS activity is obtained only after the silver staining on the chips. In many applications, including assays (Section 5.4.2.2) and cellular/tissue imaging (Section 5.4.2.3), it is favorable to avoid subsequent staining steps and to use SERS particles which are per se "autonomous" in the sense that they yield the corresponding SERS signal without further chemical steps.

Advantages of using a self-assembled monolayer (SAM) of Raman reporter molecules on the surface of a SERS label (Figure 63 left[138,141] and right[146]) are high sensitivity due to the maximum surface coverage with Raman reporters, highly reproducible spectral signatures due to the uniform orientation of the Raman reporters within the SAM, and the elimination or at least minimization of co-adsorption of other molecules which could lead to unwanted spectral interferences. The original design in Figure 63 left suffers from two complications: the dense packing of the Raman reporters within the SAM induces steric hindrance (bioconjugation of the corresponding target recognition element) and the stability of the colloid strongly depends on the particular type of Raman reporter (zeta-potential). These important aspects have been addressed in an improved design of a SERS label depicted in Figure 63 right.[146] Hydrophilic stabilization of the SAM-coated SERS NPs is achieved by covalent conjugation of monoethylene glycols (MEG) and triethylene glycols (TEG) with terminal carboxyl groups to the Raman reporter molecules. The COOH functions attached to the longer TEG spacers are sterically accessible. Furthermore,

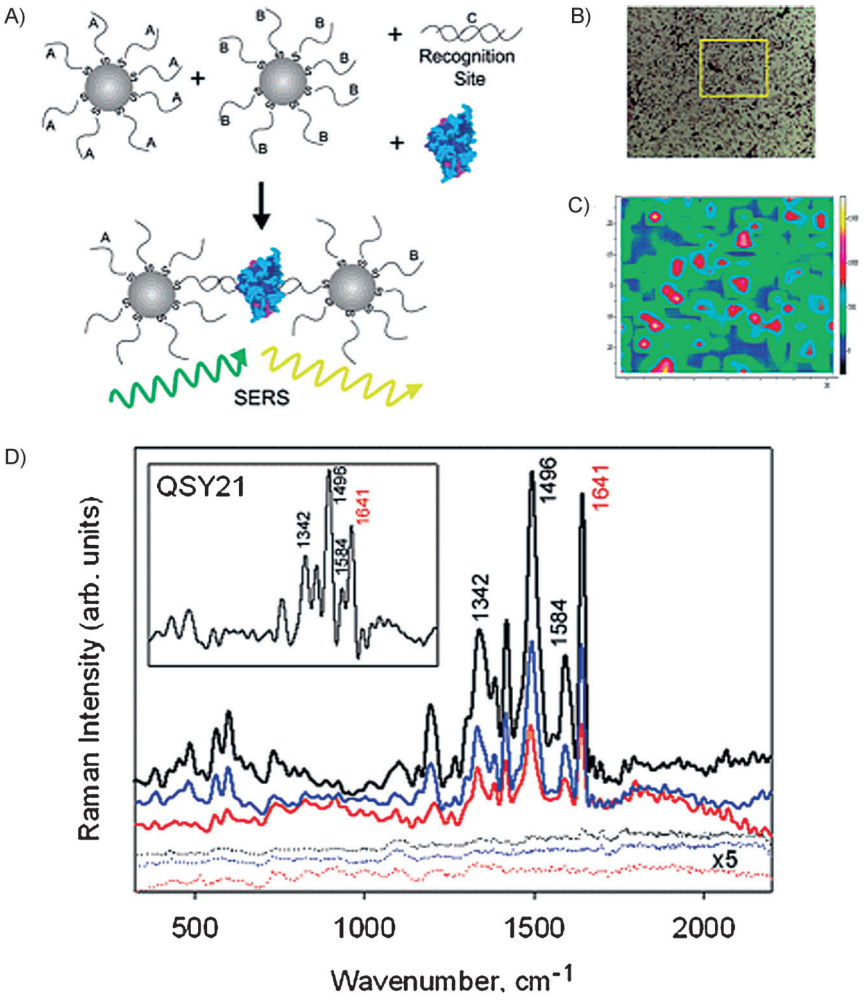

Figure 62. Probing sequence-specific DNA–protein interactions by SERS obtained after assembly of Au NPs labeled with oligonucleotides A and B. The latter bind to the single-stranded overhangs in the oligo-C-labeled double strand containing the recognition site for the Raman-dye-labeled target protein. From Ref. [149].

bioconjugation can be controlled through the stoichiometric ratio of short (MEG) to longer (TEG) hydrophilic units, with ratios typically between 100:1 and 1000:1.

Also various polymers[150,151] can be used for stabilizing and encapsulating SERS particles. Figure 64 top shows the co-adsorption of Raman reporters and thiolated polyethylene glycols (PEG) on the surface of gold cores.[150] Dyes such as malachite green can be used as Raman reporters and provide intense SERRS signals. PEGylation ensures the required colloidal stability and minimizes nonspecific binding. These SERS labels have been employed for the first in vivo SERS application for tumor targeting in a mouse model.[150]

Encapsulating SERS labels is an attractive option in particular when it ensures that the Raman reporter molecules remain adsorbed on the metal surface. For instance, polymer-encapsulated SERS labels were obtained by the self-assembly of Raman reporters (2-naphthalenethiol) and amphiphilic block copolymers in a one-pot synthesis.[151] A different, very attractive route is the encapsulation of SERS particles by glass, yielding chemically and mechanically very stable particles. First approaches started with sub-monolayer coverage through the co-adsorption of Raman reporter molecules (ca. 5%) and amino- or mercaptosilanes (ca. 95%) on the metal surface; the obtained vitreophilic particles were used in subsequent glass encapsulation by means of a sol–gel process (Stöber synthesis).[152,153] The glass encapsulation of SERS particles coated with a full-monolayer SAM, that is, 100% surface coverage with Raman reporters (Figure 65),[154,155] has been a major improvement since the resulting SERS particles are about 20 times brighter than those with only a sub-monolayer coverage of the same Raman reporter.[154]

Finally, it must be stressed that for quantitative measurements, the homogeneity of the colloidal sample is important. Density gradient centrifugation, for instance, makes it possible to separate glass-coated monomers from the significantly more SERS-active glass-coated dimers and trimers.[156,157] Figure 66 shows TEM images of glass-coated quasi-spherical 60 nm Au NPs as monomers (1), dimers (2), and trimers (3) after separation. The clusters (dimers, trimers) exhibit single-particle sensitivity and are therefore ideal SERS labels.[157]

6. Conclusions and Outlook

SERS has become a mature vibrational spectroscopic technique over the last decades and the number of applications in the chemical, material, and in particular life sciences is rapidly increasing. The electromagnetic enhancement has been identified theoretically and experimentally as the dominant mechanism. Computer simulations based on classical physics can determine the spatial and spectral dependency of the increased electric fields in plasmonically active nanostructures. At very small distances (<1 nm) quantum mechanical effects such as tunneling can occur, which may directly influence the quality of the plasmon modes. It therefore remains to be seen in which cases the classical/macroscopic description is sufficient and when the more sophisticated quantum mechanical/microscopic treatment is required. This certainly requires more experiments which investigate this aspect, ideally at the singe-particle level for correlating the structural/geometrical properties of the plasmonic nanostructures with their optical properties.

Compared with the electromagnetic enhancement, the "chemical" enhancement is more difficult to capture both theoretically and experimentally, and substantial work remains to determine its contribution and estimate its magnitude. Again, such characterizations should be per-

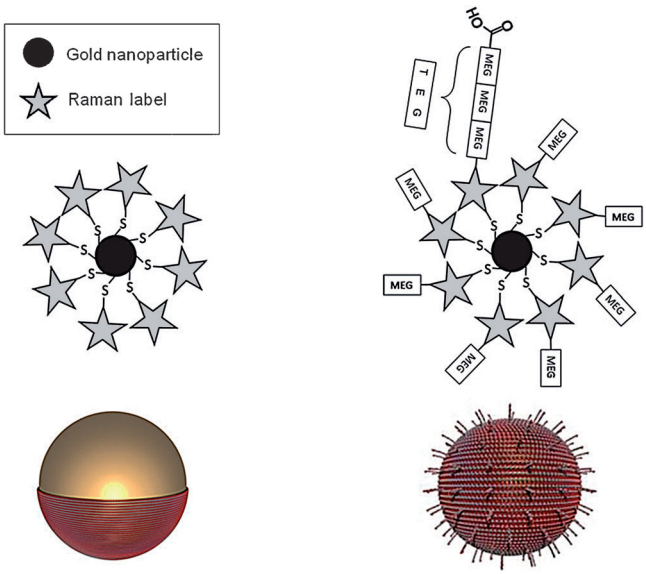

Figure 63. Rational design of SERS labels. Left: Self-assembled monolayer without hydrophilic stabilization and with steric hindrance for bioconjugation. Right: Hydrophilically stabilized Au NPs for controlled bioconjugation through terminal carboxyl groups attached to the longer TEG spacer units. From Ref. [146].

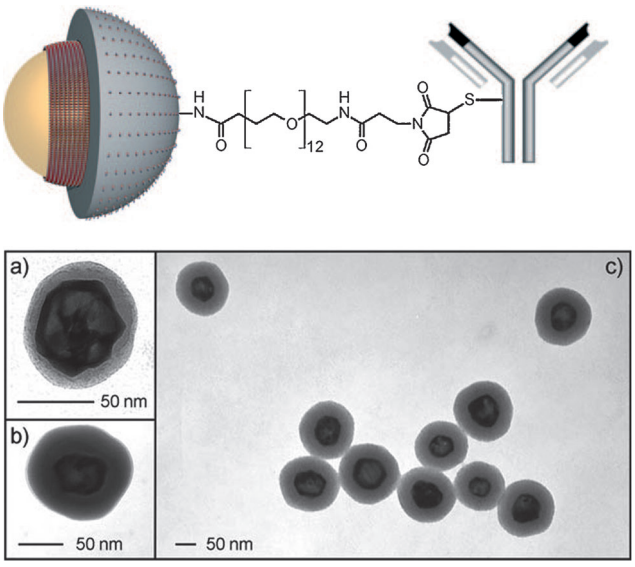

Figure 65. Glass-encapsulated SERS labels consisting of hollow Au/Ag nanoshells coated with a self-assembled monolayer of arylthiols (100% surface coverage). Functionalization of the glass surface with amino groups and hetero-bifunctional spacers allows bioconjugation to antibodies or other ligands. From Ref. [154].

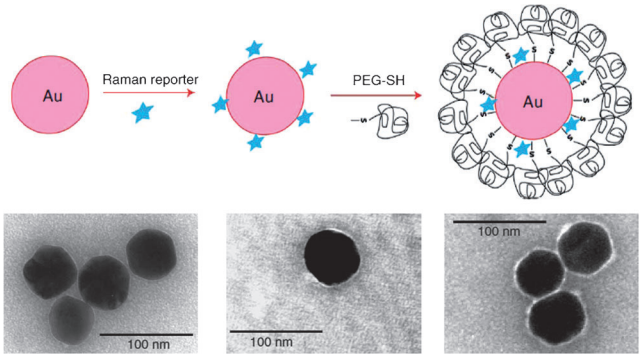

Figure 64. Rational design of SERS labels. Top: Hydrophilically stabilized SERS labels obtained by co-adsorption of Raman reporter molecules and thiolated PEG molecules. Bottom: TEM images of the SERS labels. From Ref. [150].

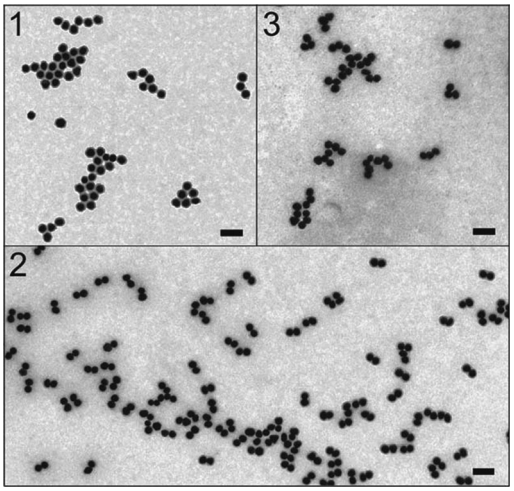

Figure 66. TEM images of purified glass-encapsulated SERS labels: 1) monomers, 2) dimers, and 3) trimers. From Ref. [157].

formed on individual, well-defined plasmonic nanostructures under controlled conditions. The theoretical description of the "chemical" effect is probably more challenging than that of the electromagnetic enhancement since it requires, among other factors, the accurate prediction of the vibrational and electronic eigenstates of the molecule adsorbed in a known geometrical configuration. Also the description of the metal surface itself must be accurate. Quantum chemists often employ atomic clusters as rather localized systems for the description of the metal surface, while quantum physicists use plane wave approaches commonly used in surface and solid-state physics. Communication between the relatively disjunct communities of SERS experimentalists and theoreticians working in "quantum-chemical" and "quantum-physical" electronic structure theory is necessary for advancing our knowledge on the fundamentals of SERS as a multidisplinary phenomenon at the interface of chemistry, molecular physics, plasmonics/metal nanostructures, and surface/solid-state physics. Despite initial and promising experimental efforts, much work on the spectroelectrochemistry of molecules on well-defined plasmonic nanostructures remains to be done on a variety of molecular systems ranging from dyes to non-resonant molecules. Tuning both the laser excitation wavelength and the potential seems to be a prerequisite for controlling the external conditions. Overall, more close collaborations and interactions between theoreticians and experimentalists are highly desirable.

Nanofabrication methods have also matured considerably during the last decade. Solid planar/2D SERS substrates can be reliably generated by physical top-down approaches with high precision. Yet, the generation of 3D SERS substrates remains a challenge[158] and colloid-based approaches seem to be a promising area for adding the next dimension to nanofabrication for SERS and plasmonics in general. Other materials, beyond traditional SERS substrates discussed in Section 4, will probably become increasingly important. Promising examples are graphene-enhanced Raman scattering (GERS)[159] and metal oxide nanoparticle-enhanced Raman scattering (MONERS).[160] These materials open up new fascinating possibilities. Also the rational design of hybrid nanostructures comprising two or more materials into bi- or even multifunctional entities is highly promising (cf. Section 5.1.3) and many more applications can be envisioned.

Colloid chemistry for the conventional bottom-up synthesis of metal NPs has also rapidly improved in terms of size- and shape-selective approaches. Unfortunately, colloidal purity in terms of a well-defined colloidal composition is still largely overlooked in many colloid-based SERS applications and it is in my opinion necessary to improve the general awareness of this issue. In contrast to correlative structure–activity experiments on single particles, which give results on individual well-characterized objects, conventional ensemble experiments on colloidal samples should be much more carefully interpreted since the ensemble distribution is usually poorly characterized, if at all. In many publications, metal colloids are only characterized by UV/Vis/NIR extinction spectroscopy rather than by electron microscopy as an essential additional technique. Dynamic light scattering, which is a mature and widely used technique for pure and well-defined colloids, yields more or less useless results in the case of mixtures. The unknown composition of a colloidal mixture containing monomers, dimers, trimers, and larger aggregates, however, makes it almost impossible to compare results at the ensemble level. Assume, for example, a "crude" mixture with a very strong SERS signal arising from 10% highly active dimers in a colloidal suspension of 20 nm Au particles (which—the experimentalist thinks so—is "pure"), may yield a stronger SERS signal than a highly well-defined sample with only 0.1% dimers in a colloidal suspension of 80 nm Au particles at a particular laser excitation wavelength. Attributing these differences to the properties of the constituting spheres and coming up with the conclusion that the 20 nm Au spheres have better SERS/scattering properties than the 80 nm spheres is certainly problematic. Only when it is known to the experimentalist by a suitable characterization technique that there actually are 100 times more dimers in the 20 nm Au colloid, which usually dominate the overall SERS intensity upon resonant excitation of their longitudinal plasmon mode, reliable conclusions can be drawn. It is this type of awareness about sample composition combined with minimal theoretical knowledge, which must be more widely communicated among experimentalists. Synthesis chemists may certainly be surprised about such comments since they are used to thoroughly characterize their samples. I strongly encourage recalling and maintaining these standards also in SERS. Beyond the characterization of a colloidal sample, this means that either "perfect" synthesis methods with monodispersity yields exceeding 90% need to be developed or, more realistically and parallel to this, separation methods are implemented as a second step after colloid synthesis. Overall, it is not unrealistic to expect that many of the conclusions drawn in literature since the very beginning of colloid-based SERS may have to be re-evaluated under these aspects.

During the last years, single-molecule SERS has developed solid concepts for unambiguously demonstrating the presence of individual molecules through the bi-analyte/isotopologue approach, thereby overcoming the initial vague argumentations based on "blinking". What remains is to expand the versatility of this powerful technique to a much broader range of molecules and applications. The key in single-molecule SERS and ultrasensitive SERS detection of molecules in general is to ensure that the molecule of interest remains in spatially highly localized regions exhibiting extreme field enhancements (hot spots) as long as possible. For many analytical applications it is probably sufficient and more desirable not to put too much emphasis on the very few extreme enhancement sites, but to exploit many more enhancement sites exhibiting smaller but still sufficiently high enhancements.

SERS is currently largely applied to molecules with surface-seeking groups since only molecules on or near the metal surface experience the large near-field enhancements upon resonant plasmon excitation. Chemists have come up with creative ideas on how to also detect "unusual analytes" without surface-seeking groups. In some cases, concepts from supramolecular (host–guest) chemistry are employed and it is realistic to expect that only by expanding the diversity of analytes, SERS will be even more widely accepted as a powerful analytical tool.

In molecular biophysics and biophysical chemistry, the combination of SERS with Raman optical activity (ROA) to give SEROA holds promise for the differentiation of chiral molecules.[161] Also the integration into SERS-based fiber sensors seems promising.[162,163] Combining SERS with other analytical techniques such as separation methods[164] and microfluidics[165–168] still has a large potential. Similar to the problems discussed above regarding colloid purity, it is equally challenging to interpret the SERS spectra of very complex mixtures. Multivariate/chemometric approaches may certainly be very supportive in this respect; however, in many cases a separation step proves to be extremely helpful since the corresponding SERS spectrum can be compared with those in a data bank. There are many other exiting analytical applications of SERS not discussed here, for example, in arts and archeology,[169,170] in forensics,[171] and in the detection of pharmaceuticals.[172,173] These areas of applied sciences are a good demonstration of how SERS as a "spectroelectrochemical" effect discovered in the 1970s has been transformed into a technique, which is now also used for solving problems in the applied sciences.

Bioanalytical applications of SERS set even more stringent constraints on metal colloids with respect to stability under physiologically revelant conditions, bioconjugation to a diverse set of ligands, and biocompatibility. While analytical chemists often prefer to work under well-defined conditions

with purified systems, biologists and medical doctors usually do not consider this to be biologically or clinically relevant. More SERS work is therefore needed to demonstrate its applicability in real-world biological and clinical analysis. Cancer diagnostics is one important area where SERS could contribute both in vitro on tissue sections and in vivo in small animals. The promising combination of SERS with spatially offset Raman spectroscopy (SORS) to SESORS[174] makes it possible to record Raman signals from tissue even mm to cm deep. Also the combination of diagnostics and therapeutics in the emerging field of theranostics with SERS particles can be envisioned. Recently, also super-resolution microscopy using SERS has been reported.[175] Relevant aspects for biomedical applications are nanotoxicology[176] and the biodistribution of SERS particles before we can even think about applications in humans.

SERS should not be looked at from an isolated perspective, but to be considered as part of other surface-enhanced/modified spectroscopic techniques such as surface-enhanced infrared absorption (SEIRA) and surface/metal-enhanced or -modified fluorescence (SEF).[177] From a broader perspective it can be regarded as a subfield of plasmonics and nanophotonics.

Comparing the performance of SERS and benchmarking it with other existing techniques is also necessary. The strength of SERS is its high content of molecular information combined with sensitivity, quantification, and multiplexing. Benchmarking of SERS versus fluorescence is important since fluorescence microscopy and spectroscopy are extremely sensitive and widely used techniques in many areas of the life and natural sciences. Future in vitro and in vivo SERS work in the next years will show to what extent additional information can be gained.

Introducing standards for comparing results obtained in different laboratories worldwide was the topic of a session during the last International Conference on Raman Spectroscopy (ICORS) in 2012 in Bangalore, India. Also SERS as a subdiscipline of Raman spectroscopy could certainly benefit from such as a "standardization" approach.

Finally, we also should think about providing more readily available training opportunities on Raman and SERS fundamentals, both on-site during workshops or summer schools as well as off-site using internet-based resources. This is particularly important for SERS experimentalists who have not received the relevant in-depth training in chemistry and physics during their regular education. However, a basic understanding of the underlying concepts and principles is absolutely essential for a comprehensive and critical interpretation of SERS spectra.

I thank Dr. Magdalena Gellner, Dr. Dennis Steinigeweg, and Dr. Wei Xie for support with the graphics.

Received: July 18, 2012
Revised: November 3, 2012
Published online: ■■ ■■, ■■■■

[1] M. Fleischmann, P. J. Hendra, A. J. McQuillan, *Chem. Phys. Lett.* **1974**, *26*, 163.
[2] D. L. Jeanmaire, R. P. Van Duyne, *J. Electroanal. Chem. Interfac. Electrochem.* **1977**, *84*, 1.
[3] S. Nie, S. R. Emory, *Science* **1997**, *275*, 1102.
[4] K. Kneipp, Y. Wang, H. Kneipp, L. T. Perelman, I. Itzkan, R. R. Dasari, M. S. Feld, *Phys. Rev. Lett.* **1997**, *78*, 1667.
[5] M. Moskovits, *Rev. Mod. Phys.* **1985**, *57*, 783.
[6] A. Otto, *J. Raman Spectrosc.* **1991**, *22*, 743.
[7] A. Campion, P. Kambhampati, *Chem. Soc. Rev.* **1998**, *27*, 241.
[8] K. Kneipp, H. Kneipp, I. Itzkan, R. R. Dasari, M. S. Feld, *J. Phys. Condens. Matter* **2002**, *14*, R597.
[9] M. Moskovits, *J. Raman Spectrosc.* **2005**, *36*, 485.
[10] P. L. Stiles, J. A. Dieringer, N. C. Shah, R. P. Van Duyne, *Annu. Rev. Anal. Chem.* **2008**, *1*, 601.
[11] R. Aroca, *Surface-Enhanced Vibrational Spectroscopy*, Wiley, New York, **2006**.
[12] *Surface-Enhanced Raman Scattering: Physics and Applications*, *Vol. 103* of *Topics in Applied Physics* (Eds.: K. Kneipp, M. Moskovits, H. Kneipp), Springer, Berlin, **2006**.
[13] E. Le Ru, P. Etchegoin, *Principles of Surface-Enhanced Raman Spectroscopy and Related Plasmonic Effects*, Elsevier, Amsterdam, **2009**.
[14] Z. Q. Tian, *J. Raman Spectrosc.* **2005**, *36*, 466.
[15] D. Graham, R. Goodacre, *Chem. Soc. Rev.* **2008**, *37*, 883.
[16] P. G. Etchegoin, *Phys. Chem. Chem. Phys.* **2009**, *11*, 7348.
[17] J. Popp, T. Mayerhöfer, *Anal. Bioanal. Chem.* **2009**, *394*, 1717.
[18] Surface Enhanced Raman Spectroscopy web themed issue, *Chem. Commun.* **2011**, Guest editors: D. Graham, Z. Tian, R. Van Duyne; http://www.rsc.org/sers.
[19] Surface Enhanced Raman Spectroscopy: Faraday Discussions No. 132 (held at Imperial College London 19–21 September **2005**), Royal Society of Chemistry, Cambridge, **2006**.
[20] P. G. Etchegoin, E. C. Le Ru, *Surface Enhanced Raman Spectroscopy* (Ed.: S. Schlücker), Wiley-VCH, Weinheim, **2011**, pp. 1–37.
[21] W. E. Smith, *Chem. Soc. Rev.* **2008**, *37*, 955.
[22] S. E. J. Bell, N. M. S. Sirimuthu, *Chem. Soc. Rev.* **2008**, *37*, 1012.
[23] S. E. J. Bell, A. Stewart, *Surface Enhanced Raman Spectroscopy* (Ed.: S. Schlücker), Wiley-VCH, Weinheim, **2011**, pp. 71–86.
[24] K. A. Willets, R. P. Van Duyne, *Annu. Rev. Phys. Chem.* **2007**, *58*, 267.
[25] V. Myroshnychenko, J. Rodríguez-Fernández, I. Pastoriza-Santos, A. M. Funston, C. Novo, P. Mulvaney, L. M. Liz-Marzán, F. J. García de Abajo, *Chem. Soc. Rev.* **2008**, *37*, 1792.
[26] H. Xu, J. Aizpurua, M. Käll, P. Apell, *Phys. Rev. E* **2000**, *62*, 4318.
[27] J. Zuloaga, E. Prodan, P. Nordlander, *Nano Lett.* **2009**, *9*, 887.
[28] E. C. Le Ru, P. G. Etchegoin, M. Meyer, *J. Chem. Phys.* **2006**, *125*, 204701.
[29] E. J. Blackie, E. C. Le Ru, P. G. Etchegoin, *J. Am. Chem. Soc.* **2009**, *131*, 14466.
[30] H. Liang, Z. Li, W. Wang, Y. Wu, H. Xu, *Adv. Mater.* **2009**, *21*, 4614.
[31] M. J. Mulvihill, X. Y. Ling, J. Henzie, P. Yang, *J. Am. Chem. Soc.* **2010**, *132*, 268.
[32] T. K. Sau, A. L. Rogach, F. Jäckel, T. A. Klar, J. Feldmann, *Adv. Mater.* **2010**, *22*, 1805.
[33] Y. Wang, E. Wang, *Surface Enhanced Raman Spectroscopy* (Ed.: S. Schlücker), Wiley-VCH, Weinheim, **2011**, pp. 39–69.
[34] E. Bailo, V. Deckert, *Chem. Soc. Rev.* **2008**, *37*, 921.
[35] T. Ichimura, S. Kawata, *Surface Enhanced Raman Spectroscopy* (Ed.: S. Schlücker), Wiley-VCH, Weinheim, **2011**, pp. 305–321.
[36] B. Pettinger, P. Schambach, C. J. Villagómez, N. Scott, *Annu. Rev. Phys. Chem.* **2012**, *63*, 379.

[37] Y. Fang, N. H. Seong, D. D. Dlott, *Science* **2008**, *321*, 388.
[38] J. H. Tian, B. Liu, X. Li, Z. L. Yang, B. Ren, S. T. Wu, N. Tao, Z. Q. Tian, *J. Am. Chem. Soc.* **2006**, *128*, 14748.
[39] K. L. Wustholz, A. I. Henry, J. M. McMahon, R. G. Freeman, N. Valley, M. E. Piotti, M. J. Natan, G. C. Schatz, R. P. Van Duyne, *J. Am. Chem. Soc.* **2010**, *132*, 10903.
[40] A. I. Henry, J. M. Bingham, E. Ringe, L. D. Marks, G. C. Schatz, R. P. Van Duyne, *J. Phys. Chem. C* **2011**, *115*, 9291.
[41] D. Steinigeweg, M. Schütz, S. Schlücker, *Nanoscale* **2013**, *5*, 110.
[42] Y. Min, M. Akbulut, K. Kristiansen, Y. Golan, J. Israelachvili, *Nat. Mater.* **2008**, *7*, 527.
[43] K. J. M. Bishop, C. E. Wilmer, S. Soh, B. A. Grzybowski, *Small* **2009**, *5*, 1600.
[44] Y. Wang, G. Chen, M. Yang, G. Silber, S. Xing, L. H. Tan, F. Wang, Y. Feng, X. Liu, S. Li, H. Chen, *Nat. Commun.* **2010**, *1*, 87.
[45] Z. Nie, A. Petukhova, E. Kumacheva, *Nat. Nanotechnol.* **2010**, *5*, 15.
[46] M. Gellner, D. Steinigeweg, S. Ichilmann, M. Salehi, M. Schütz, K. Kömpe, M. Haase, S. Schlücker, *Small* **2011**, *7*, 3445.
[47] P. H. C. Camargo, M. Rycenga, L. Au, Y. X. Xia, *Angew. Chem.* **2009**, *121*, 2214; *Angew. Chem. Int. Ed.* **2009**, *48*, 2180.
[48] C. Chen, J. A. Hutchison, F. Clemente, R. Kox, H. Uji-I, J. Hofkens, L. Lagae, G. Maes, G. Borghs, P. Van Dorpe, *Angew. Chem.* **2009**, *121*, 10116; *Angew. Chem. Int. Ed.* **2009**, *48*, 9932.
[49] A. Hartschuh, E. J. Sánchez, X. S. Xie, L. Novotny, *Phys. Rev. Lett.* **2003**, *90*, 095503.
[50] B. Pettinger, *Mol. Phys.* **2010**, *108*, 2039.
[51] J. A. Dieringer, A. D. McFarland, N. C. Shah, D. A. Stuart, A. V. Whitney, C. R. Yonzon, M. A. Young, X. Zhang, R. P. Van Duyne, *Faraday Discuss.* **2006**, *132*, 9.
[52] S. Lal, N. K. Grady, G. P. Goodrich, N. J. Halas, *Nano Lett.* **2006**, *6*, 2338.
[53] L. Zhao, L. Jensen, G. C. Schatz, *J. Am. Chem. Soc.* **2006**, *128*, 2911.
[54] L. Jensen, C. M. Aikens, G. C. Schatz, *Chem. Soc. Rev.* **2008**, *37*, 1061.
[55] T. Shegai, A. Vaskevich, I. Rubinstein, G. Haran, *J. Am. Chem. Soc.* **2009**, *131*, 14390.
[56] G. A. Baker, D. S. Moore, *Anal. Bioanal. Chem.* **2005**, *382*, 1751.
[57] M. J. Banholzer, J. E. Millstone, L. Qin, C. A. Mirkin, *Chem. Soc. Rev.* **2008**, *37*, 885.
[58] S. Lal, N. K. Grady, J. Kundu, C. S. Levin, J. B. Lassiter, N. J. Halas, *Chem. Soc. Rev.* **2008**, *37*, 898.
[59] R. J. C. Brown, M. J. T. Milton, *J. Raman Spectrosc.* **2008**, *39*, 1313.
[60] K. Hering, D. Cialla, K. Ackermann, T. Doerfer, R. Moeller, H. Schneidewind, R. Mattheis, W. Fritzsche, P. Rösch, J. Popp, *Anal. Bioanal. Chem.* **2008**, *390*, 113.
[61] X. M. Lin, Y. Cui, Y. H. Xu, B. Ren, Z.-Q. Tian, *Anal. Bioanal. Chem.* **2009**, *394*, 1729.
[62] S. Guo, S. Dong, *J. Mater. Chem.* **2011**, *21*, 16704.
[63] M. Fan, G. F. Andrade, A. G. Brolo, *Anal. Chim. Acta* **2011**, *693*, 7.
[64] D. Cialla, A. März, R. Böhme, F. Theil, K. Weber, M. Schmitt, J. Popp, *Anal. Bioanal. Chem.* **2012**, *403*, 27.
[65] X. Gong, Y. Bao, C. Qiu, C. Jiang, *Chem. Commun.* **2012**, *48*, 7003.
[66] G. V. P. Kumar, *J. Nanophotonics* **2012**, *6*, 064503.
[67] J. F. Li, Y. F. Huang, Y. Ding, Z. L. Yang, S. B. Li, X. S. Zhou, F. R. Fan, W. Zhang, Z. Y. Zhou, D. Y. Wu, B. Ren, Z. L. Wang, Z. Q. Tian, *Nature* **2010**, *464*, 392.
[68] J. R. Anema, J. F. Li, Z. L. Yang, B. Ren, Z. Q. Tian, *Annu. Rev. Anal. Chem.* **2011**, *4*, 129.
[69] Y. Xia, Y. Xiong, B. Lim, S. E. Skrabalak, *Angew. Chem.* **2008**, *121*, 62; *Angew. Chem. Int. Ed.* **2008**, *48*, 60.
[70] X. Lu, M. Rycenga, S. E. Skrabalak, B. Wiley, Y. Xia, *Annu. Rev. Anal. Chem.* **2009**, *60*, 167.
[71] W. Li, P. H. C. Camargo, L. Au, Q. Zhang, M. Rycenga, Y. Xia, *Angew. Chem.* **2010**, *122*, 168; *Angew. Chem. Int. Ed.* **2010**, *49*, 164.
[72] D. Steinigeweg, S. Schlücker, *Chem. Commun.* **2012**, *48*, 8682.
[73] T. R. Jensen, M. D. Malinsky, C. L. Haynes, R. P. Van Duyne, *J. Phys. Chem. B* **2000**, *104*, 10549.
[74] C. L. Haynes, R. P. Van Duyne, *J. Phys. Chem. B* **2001**, *105*, 5599.
[75] S. Mahajan, J. J. Baumberg, A. E. Russell, P. N. Bartlett, *Phys. Chem. Chem. Phys.* **2007**, *9*, 6016.
[76] D. Y. Wu, J. F. Li, B. Ren, Z. Q. Tian, *Chem. Soc. Rev.* **2008**, *37*, 1025.
[77] X. Zhang, J. Zhao, A. V. Whitney, J. W. Elam, R. P. Van Duyne, *J. Am. Chem. Soc.* **2006**, *128*, 10304.
[78] H. Wang, C. S. Levin, N. J. Halas, *J. Am. Chem. Soc.* **2005**, *127*, 14992.
[79] S. Abalde-Cela, S. Ho, B. Rodríguez-González, M. A. Correa-Duarte, R. A. Álvarez-Puebla, L. M. Liz-Marzán, N. A. Kotov, *Angew. Chem.* **2009**, *121*, 5430; *Angew. Chem. Int. Ed.* **2009**, *48*, 5326.
[80] S. J. Lee, A. R. Morrill, M. Moskovits, *J. Am. Chem. Soc.* **2006**, *128*, 2200.
[81] H. Kim, K. M. Kosuda, R. P. Van Duyne, P. C. Stair, *Chem. Soc. Rev.* **2010**, *39*, 4820.
[82] Z.-Q. Tian, B. Ren, *Annu. Rev. Phys. Chem.* **2004**, *55*, 197.
[83] B. Ren, Y. Cui, D.-Y. Wu, Z.-Q. Tian, *Surface Enhanced Raman Spectroscopy* (Ed.: S. Schlücker), Wiley-VCH, Weinheim, **2011**, pp. 191 – 218.
[84] X. Li, A. A. Gewirth, *J. Am. Chem. Soc.* **2005**, *127*, 5252.
[85] A. Wang, Y. F. Huang, U. K. Sur, D. Y. Wu, B. Ren, S. Rondinini, C. Amatore, Z. Q. Tian, *J. Am. Chem. Soc.* **2010**, *132*, 9534.
[86] W. Xie, C. Herrmann, K. Kömpe, M. Haase, S. Schlücker, *J. Am. Chem. Soc.* **2011**, *133*, 19302.
[87] A. Kranich, H. K. Ly, P. Hildebrandt, D. H. Murgida, *J. Am. Chem. Soc.* **2008**, *130*, 9844.
[88] D. H. Murgida, P. Hildebrandt, *Chem. Soc. Rev.* **2008**, *37*, 937.
[89] H. K. Ly, M. Sezer, N. Wisitruangsakul, J. J. Feng, A. Kranich, D. Millo, I. M. Weidinger, I. Zebger, D. H. Murgida, P. Hildebrandt, *FEBS J.* **2011**, *278*, 1382.
[90] P. Hildebrandt, J.-J. Feng, A. Kranich, K. H. Ly, D. F. Martín, M. Martí, D. H. Murgida, D. A. Paggi, N. Wisitruangsakul, M. Sezer, I. M. Weidinger, I. Zebger, *Surface Enhanced Raman Spectroscopy* (Ed.: S. Schlücker), Wiley-VCH, Weinheim, **2011**, pp. 219 – 240.
[91] X. M. Qian, S. M. Nie, *Chem. Soc. Rev.* **2008**, *37*, 912.
[92] N. P. W. Pieczonka, R. F. Aroca, *Chem. Soc. Rev.* **2008**, *37*, 946.
[93] K. L. Wustholz, C. L. Brosseau, F. Casadio, R. P. Van Duyne, *Phys. Chem. Chem. Phys.* **2009**, *11*, 7350.
[94] N. P. W. Pieczonka, G. Moula, A. R. Skarbek, R. F. Aroca, *Surface Enhanced Raman Spectroscopy* (Ed.: S. Schlücker), Wiley-VCH, Weinheim, **2011**, pp. 87 – 101.
[95] E. C. Le Ru, M. Meyer, P. G. Etchegoin, *J. Phys. Chem. B* **2006**, *110*, 1944.
[96] J. A. Dieringer, R. B. Lettan II, K. A. Scheidt, R. P. Van Duyne, *J. Am. Chem. Soc.* **2007**, *129*, 16249.
[97] P. G. Etchegoin, E. C. Le Ru, M. Meyer, *J. Am. Chem. Soc.* **2009**, *131*, 2713.
[98] J. P. Camden, J. A. Dieringer, Y. Wang, D. J. Masiello, L. D. Marks, G. C. Schatz, R. P. Van Duyne, *J. Am. Chem. Soc.* **2008**, *130*, 12616.
[99] L. Rodriguez-Lorenzo, R. A. Álvarez-Puebla, I. Pastoriza-Santos, S. Mazzucco, O. Stéphan, M. Kociak, L. M. Liz-Marzán, F. J. Garcia de Abajo, *J. Am. Chem. Soc.* **2009**, *131*, 4616.

[100] D. K. Lim, K. S. Jeon, H. M. Kim, J. M. Nam, Y. D. Suh, *Nat. Mater.* **2010**, *9*, 60.
[101] D. K. Lim, L. S. Jeon, J. H. Hwang, H. Kim, S. Kwon, Y. D. Suh, J. M. Nam, *Nat. Nanotechnol.* **2011**, *6*, 452.
[102] J. N. Anker, W. P. Hall, O. Lyandres, N. C. Shah, J. Zhao, R. P. Van Duyne, *Nat. Mater.* **2008**, *7*, 442.
[103] K. C. Bantz, A. F. Meyer, N. J. Wittenberg, H. Im, Ö. Kurtuluş, S. H. Lee, N. C. Lindquist, S.-H. Oh, C. L. Haynes, *Phys. Chem. Chem. Phys.* **2011**, *13*, 11551.
[104] Y. B. Zheng, B. Kiraly, P. S. Weiss, T. J. Huang, *Nanomedicine* **2012**, *7*, 751.
[105] X. Qian, J. Li, S. Nie, *J. Am. Chem. Soc.* **2009**, *131*, 7540.
[106] S. W. Bishnoi, C. J. Rozell, C. S. Levin, M. K. Gheith, B. R. Johnson, D. H. Johnson, N. J. Halas, *Nano Lett.* **2006**, *6*, 1687.
[107] J. Kneipp, H. Kneipp, B. Wittig, K. Kneipp, *Nano Lett.* **2007**, *7*, 2819.
[108] J. Kneipp, H. Kneipp, B. Wittig, K. Kneipp, *Nanomed. Nanotechnol. Biol. Med.* **2010**, *6*, 214.
[109] J. Kneipp in *Surface Enhanced Raman Spectroscopy* (Ed.: S. Schlücker), Wiley-VCH, Weinheim, **2011**, pp. 285 – 304.
[110] R. A. Álvarez-Puebla, L. M. Liz-Marzán, *Energy Environ. Sci.* **2010**, *3*, 1011.
[111] L. Guerrini, J. V. Garcia-Ramos, C. Domingo, S. Sanchez-Cortes, *Anal. Chem.* **2009**, *81*, 953.
[112] L. Guerrini, Z. Jurasekova, C. Domingo, M. Pérez-Méndez, P. Leyton, M. Campos-Vallette, J. V. Garcia-Ramos, S. Sanchez-Cortes, *Plasmonics* **2007**, *2*, 147.
[113] L. Guerrini, P. Leyton, M. Campos-Vallette, C. Domingo, J. V. Garcia-Ramos, S. Sanchez-Cortes, *Surface Enhanced Raman Spectroscopy* (Ed.: S. Schlücker), Wiley-VCH, Weinheim, **2011**, pp. 103 – 128.
[114] K. E. Shafer-Peltier, C. L. Haynes, M. R. Glucksberg, R. P. Van Duyne, *J. Am. Chem. Soc.* **2003**, *125*, 588.
[115] R. A. Alvarez-Puebla, L. M. Liz-Marzán, *Chem. Soc. Rev.* **2012**, *41*, 43.
[116] M. Hu, F. S. Ou, W. Wu, I. Naumov, X. Li, A. M. Bratkovsky, R. S. Williams, Z. Li, *J. Am. Chem. Soc.* **2010**, *132*, 12820.
[117] M. Roca, A. J. Haes, *J. Am. Chem. Soc.* **2008**, *130*, 14273.
[118] R. A. Álvarez-Puebla, R. Contreras-Cáceres, I. Pastoriza-Santos, J. Pérez-Juste, L. M. Liz-Marzán, *Angew. Chem.* **2009**, *121*, 144; *Angew. Chem. Int. Ed.* **2009**, *48*, 138.
[119] C. Schmuck, P. Wich, B. Küstner, W. Kiefer, S. Schlücker, *Angew. Chem.* **2007**, *119*, 4870; *Angew. Chem. Int. Ed.* **2007**, *46*, 4786.
[120] M. Gellner, S. Niebling, H. Y. Kuchelmeister, C. Schmuck, S. Schlücker, *Chem. Commun.* **2011**, *47*, 12762.
[121] I. Chourpa, F. H. Lei, P. Dubois, M. Manfait, G. D. Sockalingum, *Chem. Soc. Rev.* **2008**, *37*, 993.
[122] K. W. Kho, C. Y. Fu, U. S. Dinish, M. Olivo, *J. Biophotonics* **2011**, *4*, 667.
[123] W. Xie, P. Qiu, C. Mao, *J. Mater. Chem.* **2011**, *21*, 5190.
[124] J. A. Dougan, K. Faulds, *Analyst* **2012**, *137*, 545.
[125] J. Kneipp, H. Kneipp, K. Kneipp, *Chem. Soc. Rev.* **2008**, *37*, 1052.
[126] C. A. Mirkin, R. L. Letsinger, R. C. Mucic, J. J. Storhoff, *Nature* **1996**, *382*, 607.
[127] J. J. Storhoff, R. Elghanian, R. C. Mucic, C. A. Mirkin, R. L. Letsinger, *J. Am. Chem. Soc.* **1998**, *120*, 1959.
[128] Y. Wei, C. Cao, R. Jin, C. A. Mirkin, *Science* **2002**, *297*, 1536.
[129] D. Graham, K. Faulds, *Chem. Soc. Rev.* **2008**, *37*, 1042.
[130] R. Stevenson, K. Faulds, D. Graham, *Surface Enhanced Raman Spectroscopy* (Ed.: S. Schlücker), Wiley-VCH, Weinheim, **2011**, pp. 241 – 262.
[131] K. Faulds, W. E. Smith, D. Graham, *Anal. Chem.* **2004**, *76*, 412.
[132] K. Faulds, F. McKenzie, W. E. Smith, D. Graham, *Angew. Chem.* **2007**, *119*, 1861; *Angew. Chem. Int. Ed.* **2007**, *46*, 1829.
[133] D. Graham, D. G. Thompson, W. E. Smith, K. Faulds, *Nat. Nanotechnol.* **2008**, *3*, 548.
[134] S. E. J. Bell, N. M. S. Sirimuthu, *J. Am. Chem. Soc.* **2006**, *128*, 15580.
[135] E. Papadopoulou, S. E. J. Bell, *Angew. Chem.* **2011**, *123*, 9224; Angew. Chem. Int. Ed. **2011**, 50, 9058.
[136] A. Barhoumi, N. J. Halas, *J. Am. Chem. Soc.* **2010**, *132*, 12792.
[137] S. Mahajan, J. Richardson, T. Brown, P. N. Bartlett, *J. Am. Chem. Soc.* **2008**, *130*, 15589.
[138] M. D. Porter, R. J. Lipert, L. M. Siperko, G. Wang, R. Narayanan, *Chem. Soc. Rev.* **2008**, *37*, 1001.
[139] X. X. Han, B. Zhao, Y. Ozaki, *Anal. Bioanal. Chem.* **2009**, *394*, 1719.
[140] Y. C. Cao, R. Jin, J. M. Nam, C. S. Thaxton, C. A. Mirkin, *J. Am. Chem. Soc.* **2003**, *125*, 14676.
[141] D. S. Grubisha, R. J. Lipert, H. Y. Park, J. Driskell, M. D. Porter, *Anal. Chem.* **2003**, *75*, 5936.
[142] J. D. Driskell, J. M. Uhlenkamp, R. J. Lipert, M. D. Porter, *Anal. Chem.* **2007**, *79*, 4141.
[143] S. Schlücker, B. Küstner, A. Punge, R. Bonfig, A. Marx, P. Ströbel, *J. Raman Spectrosc.* **2006**, *37*, 719.
[144] S. Schlücker, *ChemPhysChem* **2009**, *10*, 1344.
[145] S. Schlücker in *Surface Enhanced Raman Spectroscopy* (Ed.: S. Schlücker), Wiley-VCH, Weinheim, **2011**, pp. 263 – 283.
[146] C. Jehn, B. Küstner, P. Adam, A. Marx, P. Ströbel, C. Schmuck, S. Schlücker, *Phys. Chem. Chem. Phys.* **2009**, *11*, 7499.
[147] M. Schütz, D. Steinigeweg, M. Salehi, K. Kömpe, S. Schlücker, *Chem. Commun.* **2011**, *47*, 4216.
[148] S. Schlücker, M. Salehi, G. Bergner, M. Schütz, P. Ströbel, A. Marx, I. Petersen, B. Dietzek, J. Popp, *Anal. Chem.* **2011**, *83*, 7081.
[149] A. J. Bonham, G. Braun, I. Pavel, M. Moskovits, N. O. Reich, *J. Am. Chem. Soc.* **2007**, *129*, 14572.
[150] X. Qian, X. H. Peng, D. O. Ansari, Q. Yin-Goen, G. Z. Chen, D. M. Shin, L. Yang, A. N. Young, M. D. Wang, S. Nie, *Nat. Biotechnol.* **2008**, *26*, 83.
[151] M. Yang, T. Chen, W. S. Lau, Y. Wang, Q. Tang, Y. Yang, H. Y. Chen, *Small* **2009**, *5*, 198.
[152] W. E. Doering, S. Nie, *Anal. Chem.* **2003**, *75*, 6171.
[153] S. P. Mulvaney, M. D. Musick, C. D. Keating, M. J. Natan, *Langmuir* **2003**, *19*, 4784.
[154] B. Küstner, M. Gellner, M. Schütz, F. Schöppler, A. Marx, P. Ströbel, P. Adam, C. Schmuck, S. Schlücker, *Angew. Chem.* **2009**, *121*, 1984; *Angew. Chem. Int. Ed.* **2009**, *48*, 1950.
[155] M. Schütz, B. Küstner, M. Bauer, C. Schmuck, S. Schlücker, *Small* **2010**, *6*, 733.
[156] G. Chen, Y. Wang, L. H. Tan, M. X. Yang, L. S. Tan, Y. Chen, H. Chen, *J. Am. Chem. Soc.* **2009**, *131*, 4218.
[157] D. Steinigeweg, M. Schütz, M. Salehi, S. Schlücker, *Small* **2011**, *7*, 2443.
[158] K. A. Stoerzinger, J. Y. Lin, T. W. Odom, *Chem. Sci.* **2011**, *2*, 1435.
[159] X. Ling, L. Xie, Y. Fang, H. Xu, H. Zhang, J. Kong, M. S. Dresselhaus, J. Zhang, Z. Liu, *Nano Lett.* **2010**, *10*, 553.
[160] L. Li, T. Hutter, A. S. Finnemore, F. M. Huang, J. J. Baumberg, S. R. Elliott, U. Steiner, S. Mahajan, *Nano Lett.* **2012**, *12*, 4242.
[161] S. Abdali, E. W. Blanch, *Chem. Soc. Rev.* **2008**, *37*, 980.
[162] P. R. Stoddart, D. J. White, *Anal. Bioanal. Chem.* **2009**, *394*, 1761.
[163] C. Shi, Y. Zhang, C. Gu, B. Chen, L. Seballos, T. Olson, J. Z. Zhang, *J. Nanosci. Nanotechnol.* **2009**, *9*, 2234.
[164] A. J. Hobro, B. Lendl, *Surface Enhanced Raman Spectroscopy* (Ed.: S. Schlücker), Wiley-VCH, Weinheim, **2011**, pp. 155 – 171.
[165] L. Chen, J. Choo, *Electrophoresis* **2008**, *29*, 1815.
[166] Y. S. Huh, A. J. Chung, D. Erickson, *Microfluid. Nanofluid.* **2009**, *6*, 285.
[167] Y. Yin, T. Qiu, W. Zhang, P. C. Chu, *J. Mater. Res.* **2011**, *26*, 170.

[168] T. Henkel, A. März, J. Popp, *Surface Enhanced Raman Spectroscopy* (Ed.: S. Schlücker), Wiley-VCH, Weinheim, **2011**, pp. 173 – 190.
[169] K. Chen, M. Leona, T. Vo-Dinh, *Sens. Rev.* **2007**, *27*, 109.
[170] F. Casadio, M. Leona, J. R. Lombardi, R. P. Van Duyne, *Acc. Chem. Res.* **2010**, *43*, 782.
[171] A. G. Ryder, *Curr. Opin. Chem. Biol.* **2005**, *9*, 489.
[172] C. Pînzaru, I. Pavel, N. Leopold, W. Kiefer, *J. Raman Spectrosc.* **2004**, *35*, 338.
[173] S. C. Pînzaru, I. Pavel, *Surface Enhanced Raman Spectroscopy* (Ed.: S. Schlücker), Wiley-VCH, Weinheim, **2011**, pp. 129 – 154.
[174] N. Stone, M. Kerssens, G. R. Lloyd, K. Faulds, D. Graham, P. Matousek, *Chem. Sci.* **2011**, *2*, 776.
[175] S. M. Stranahan, K. A. Willets, *Nano Lett.* **2010**, *10*, 3777.
[176] B. J. Marquis, S. A. Love, K. L. Braun, C. L. Haynes, *Analyst* **2009**, *134*, 425.
[177] I. A. Larmour, D. Graham, *Analyst* **2011**, *136*, 3831.

